UNIVERSITÀ DEGLI STUDI DI GENOVA

SCUOLA DI SCIENZE MEDICHE E FARMACEUTICHE

DIPARTIMENTO DI SCIENZE CHIRURGICHE E DIAGNOSTICHE INTEGRATE (DISC)

Corso di Laurea Magistrale in Odontoiatria e Protesi Dentaria

TESI DI LAUREA

" Development of Zn^{2+}-Doped Brushite-Based Calcium Phosphate Cements Combined with PCL for Potential Bone Regeneration Applications through 3D Printing "

Relatore: Prof. De Angelis Nicola Antonio Cesare
Correlatore: Prof. Lagazzo Alberto

Candidato: Bianchetti Francesco
Matricola: 5410011

Anno Accademico 2025/2026

TABLE OF CONTENTS

1. INTRODUCTION

1.1. Anatomy and biology of the periodontium

The periodontium comprises the set of tissues that ensure the support and anchorage of the tooth within the jaws, namely the gingiva, root cementum, periodontal ligament, and alveolar bone. These elements should not be considered as independent structures, but rather as components of a single functional and biological unit that develops and matures in a coordinated manner during tooth formation and eruption. [1]

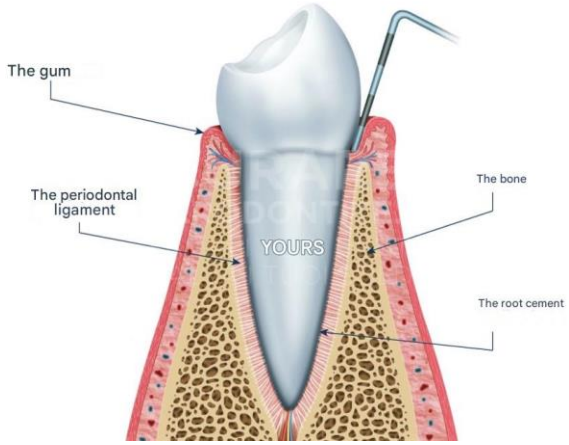

Figure 1: *Anatomical representation of the periodontium*

The development of periodontal tissues is closely related to odontogenesis and occurs mainly in conjunction with the formation of dental roots. Most periodontal structures originate from the dental follicle, a structure of ectomesenchymal origin that surrounds the tooth germ. The cells that give rise to the dental follicle are themselves derived from the neural crest, a pluripotent cell population that plays a fundamental role in craniofacial development. [2]

During the early stages of embryonic development, neural crest cells migrate from the neural tube toward the developing branchial arches, where they acquire a mesenchymal phenotype that allows them to differentiate into numerous cell types. Alterations in the migration or differentiation processes of these cells can lead to severe developmental anomalies, such as the absence of dental elements or incomplete formation of the jaw bones.

The dental follicle, together with the dental papilla, represents the main mesenchymal compartment of the tooth germ. In particular, while the dental papilla will give rise to the pulp and odontoblasts, the dental follicle is responsible for the formation of the periodontal supporting tissues, namely cementum, periodontal ligament, and alveolar

bone. From an anatomical perspective, the dental follicle consists of a more internal portion, closely associated with the tooth germ, and a more peripheral component in continuity with the developing bony trabeculae that surround the tooth.

Taken together, these data indicate that the development of the periodontium is the result of a highly organized process involving cell populations of common origin and complex biological interactions. In this context, alveolar bone plays a key role not only as a structural support for the tooth, but also as a dynamic tissue capable of continuously adapting to functional loads and to changes in the periodontal environment. [3]

1.2. Histological characteristics of bone

Bone tissue is a specialized connective tissue characterized by the presence of a mineralized extracellular matrix, whose particular chemical composition and histological organization confer high hardness and resistance to both tension and compression to the bones. At the same time, thanks to a refined structural architecture, bone tissue is relatively light, allowing an effective supporting function and enabling the action of skeletal muscles without excessive energy expenditure.

In addition to mechanical functions, bone plays a fundamental role in mineral metabolism, representing the main reservoir of calcium in the body and contributing to the maintenance of the concentration of this ion in body fluids, which is essential for numerous biological and functional processes.

From a compositional point of view, bone tissue consists of 10–20% water, while the dry mass is composed of approximately 65–70% inorganic component and the remaining 30–35% organic component.

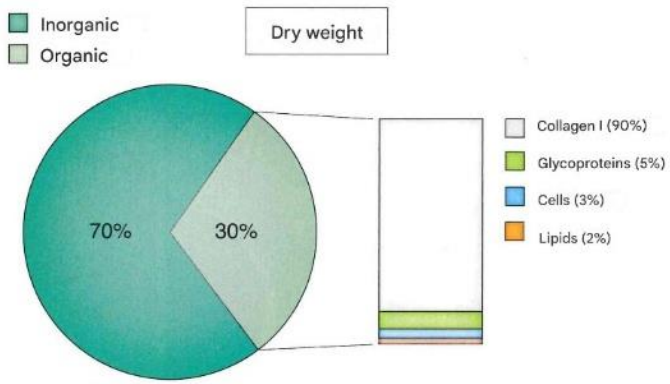

Figure 2: *Pie chart of the chemical composition of bone tissue after dehydration.*

Organic component characterized by:

- *Cells of bone tissue:*
    - Osteoprogenitor cells (preosteoblasts): mainly located in the cambial layer of the periosteum and endosteum, they derive from the osteogenic differentiation of pluripotent mesenchymal cells of connective tissues. When appropriately stimulated, these cells proliferate and differentiate into osteoblasts.
    - Osteoblasts: metabolically active cells responsible for the synthesis of the organic extracellular matrix (osteoid), which undergoes calcification processes through the deposition of minerals such as calcium and phosphate; subsequently, the addition of hydroxide and bicarbonate ions leads to the formation of hydroxyapatite crystals, which represent bone in its mature form. [4]

      Once osteoblasts have completed their function, they remain embedded within the mineralized matrix and transform into osteocytes.
    - Osteocytes: they represent the most numerous cellular population in mature bone; they are located within bone lacunae and maintain mutual contacts through a network of canaliculi; they play a fundamental role in the maintenance of the bone matrix and in the perception of mechanical stimuli.
    - Osteoclasts: multinucleated cells of hematopoietic origin belonging to the monocyte–macrophage lineage, specialized in bone tissue resorption. They act through acidification of the microenvironment and the secretion of lysosomal enzymes, allowing the continuous renewal and remodeling of bone tissue.

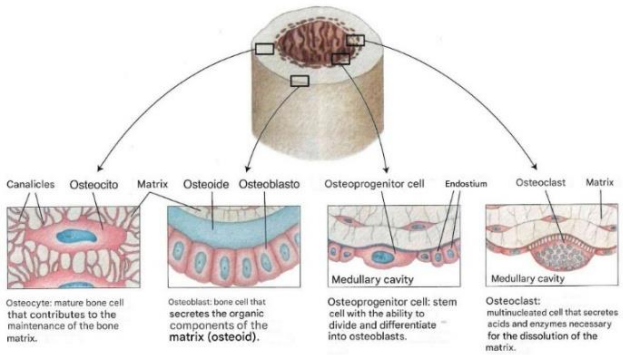

Figure 3: *Representation of bone cells and their predominant location within the wall of a long bone.*

- *Organic component of the extracellular matrix*: rich in type I collagen fibers, non-collagenous proteins (Gla proteins), proteoglycans, glycoproteins (osteonectin), and lipids. This component provides bone with elasticity and resistance to mechanical stress.

Inorganic component:

Composed mainly of the inorganic portion of the extracellular matrix, which consists of calcium and phosphate salts organized in the form of hydroxyapatite crystals, responsible for the hardness and compressive strength of bone tissue. [5,6]

From a histomorphological point of view, bone tissue can be distinguished into:

- *Non-lamellar bone:* characterized by a disorganized arrangement of collagen fibers, it is typical of the early stages of development and of repair processes, whereas in adults it is present in limited sites, such as bone sutures or areas of new formation.
- *Lamellar bone:* represents the predominant form in the adult organism and is characterized by a high structural organization of collagen fibers, which ensures greater resistance to mechanical stress.

  Lamellar bone, based on its macroscopic structure, is further divided into:
  - Compact bone, which constitutes the outermost layer of bones and is organized into cylindrical structural units called osteons, at the center of which runs the Haversian canal containing blood vessels and nerve fibers.
  - Spongy bone, formed by a three-dimensional network of trabeculae that delimit spaces containing bone marrow; this architecture allows an effective distribution of mechanical loads and promotes metabolic exchanges. [7]

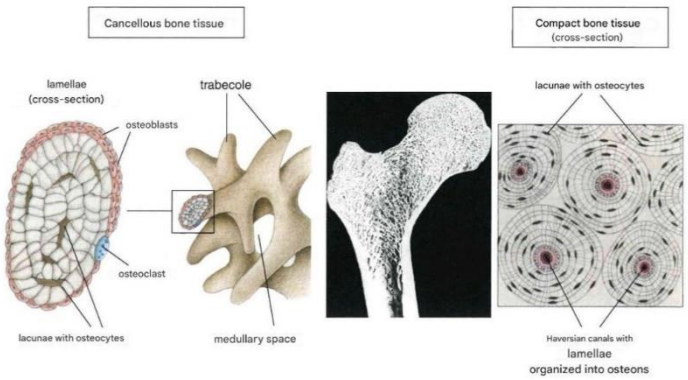

Figure 4: *Histological organization of spongy and compact bone tissue.*

All bones are externally covered by the periosteum, a connective membrane consisting of an outer fibrous layer and an inner cambial layer rich in osteoprogenitor cells, essential for growth and repair processes. The internal surfaces of bone cavities and vascular canals are instead lined by the endosteum, formed by a thin layer of cells with osteogenic function.

Therefore, bone tissue is characterized by high metabolic activity, due to the continuous alternation of processes of deposition and resorption, collectively known as bone remodeling. This process allows bone to adapt its structure to mechanical stresses and to the metabolic needs of the organism, while maintaining calcium homeostasis.

With advancing age, the balance between deposition and resorption tends to shift in favor of the latter, resulting in a progressive reduction in bone mass and an increase in skeletal fragility. [7]

It is important to emphasize that, although they share these general histological principles, the different bones of the skeleton show significant structural and functional variations in relation to their origin, function, and the biomechanical stresses to which they are subjected. These differences are particularly evident in the craniofacial region, where the maxillary bone and the mandibular bone exhibit distinctive histological and biological characteristics of great relevance in dentistry and implantology.

1.3. Anatomy of the jaw bones

The skeleton of the head consists of the skull, in which two parts can be distinguished that are continuous with each other: the neurocranium, largely formed by flat bones that delimit the cranial cavity in which the brain is housed, and the viscerocranium/splanchnocranium, composed of bones located in the anteroinferior part of the skull that contribute to delimiting visceral cavities such as the orbital cavities, nasal cavities, and the oral cavity.

From a dental perspective, the bones of the viscerocranium of greatest interest are the maxillary bone and the mandibular bone.

<u>The maxillary bone:</u>

A paired and symmetrical bone that forms a large part of the skeleton of the face; it participates in the formation of the orbital cavities, the nasal cavities, and the oral cavity and houses the upper teeth. Inside it is the largest of the paranasal sinuses, namely the maxillary sinus (Antrum of Highmore), which represents a pneumatic cavity that communicates with the nasal cavity through an orifice located on the medial wall in an anterosuperior position, which drains into the middle meatus.

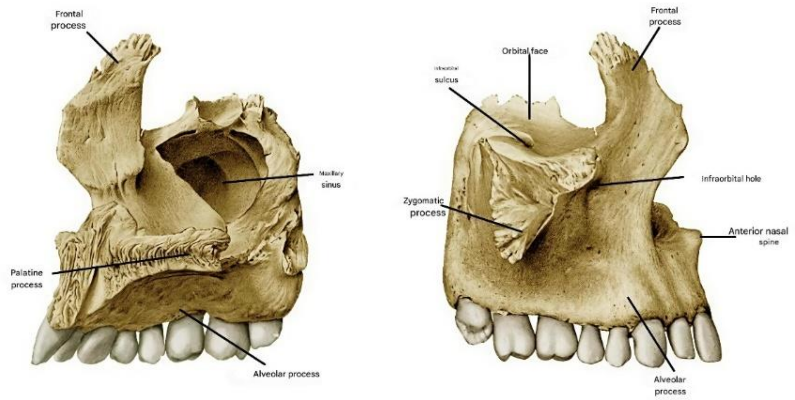

Figure 5: *Body and processes of the maxillary bone (images taken from the internet)*

For this bone we can distinguish:

- Body: a voluminous and hollow triangular pyramid-shaped portion characterized by four surfaces:
  - Anterior: a superficial triangular surface that continues laterally into the zygomatic process, superiorly into the frontal process, and inferiorly into the alveolar process. In the center it presents a depression (canine fossa) above which the infraorbital foramen is visible (which represents the opening of the infraorbital canal originating from the orbital surface). Medially this surface ends with the nasal notch which, together with the contralateral maxillary bone, delimits the piriform aperture (allowing access to the nasal cavity).
  - Superior/orbital: a slightly concave surface that contributes to forming the floor of the orbit. Posteriorly the infraorbital groove is located, which continues anteriorly into the infraorbital canal, in whose anterior part originate the incisive canals through which nerves and blood vessels pass to reach the alveoli of the upper incisors and canines.
  - Medial/nasal: a surface that constitutes most of the lateral wall of the nasal cavities and presents, in its central part, the maxillary opening that provides access to the maxillary sinus. In front of the maxillary opening there is the lacrimal groove, which is transformed into the nasolacrimal canal through articulation with the lacrimal bone and with the inferior nasal concha. Behind the opening, the nasal surface is rough for articulation with the palatine bone and, at the limit with the posterior surface, presents the greater palatine groove which, through articulation with the vertical part of the palatine bone, becomes the greater palatine canal for the vessels and nerve of the same name.

- Posterior/infratemporal: a surface that continues laterally into the zygomatic process and inferiorly into the alveolar process. In the central part of the surface there is a convexity, the maxillary tuberosity, which is smooth in its superior part and rough inferiorly for articulation with the palatine bone. At this level alveolar foramina are also visible that open into the alveolar canals traversed by the posterior superior alveolar vessels and nerves for the premolar and molar teeth.

- Four processes:
  - Frontal: it detaches anterosuperiorly from the external and nasal surfaces and extends upward between the lacrimal bone and the nasal bone to articulate with the frontal bone. The anterior margin of the process joins the nasal bone while the posterior margin articulates with the lacrimal bone.
  - Zygomatic: a voluminous bony prominence in the shape of a triangular pyramid with a base corresponding to the anterior surface of the maxilla and a truncated apex that articulates with the zygomatic bone at the zygomaticomaxillary suture. The superior surface participates in forming the floor of the orbital cavity.
  - Palatine: it has the shape of a quadrangular horizontal lamina that originates from the inferior part of the medial surface of the maxillary bone. With its superior surface it delimits the floor of the nasal cavities; with the inferior surface it forms the anterior two-thirds of the hard palate, delimiting superiorly the oral cavity; the medial margin articulates with the contralateral palatine process forming the median palatine suture; the posterior margin articulates with the horizontal part of the palatine bone forming the transverse palatine suture. On the inferior surface of the palate, immediately behind the incisors, there is the opening of the incisive canal which, running upward, divides and reaches each nasal cavity.
  - Alveolar: it originates from the inferior part of the maxillary bone and houses the teeth of the upper alveolar hemiarch. It appears as an arched prominence in the shape of a horseshoe which, articulating with the alveolar process of the opposite side, constitutes the upper alveolar arch. In adults the process is characterized by the presence of eight cavities (the dental alveoli) separated by interalveolar septa. The anterior dental alveoli are simple conical cavities

corresponding to the roots of the incisors and canine teeth; the posterior alveoli present multiple cavities separated by interradicular septa for the roots of premolar and molar teeth. On the external surface of the process, above the dental alveoli, prominences are visible (the alveolar jugums); above the jugums of the incisors there is a depression (the incisive fossa).

From an evolutionary point of view, the maxillary bone develops from five centers of membranous ossification, from which two distinct bones initially form, the true maxillary bone and the intermaxillary bone; subsequently the two parts unite into a single piece. The palatine processes (of both maxillary bones), initially directed downward and separated by the lingual primordium, around the sixtieth day elevate becoming horizontal and fuse on the midline. Alterations of these morphogenetic mechanisms result in cleft palate. Around the fourth month of fetal life the alveolar process appears with the dental primordia. The formation of the maxillary sinus begins in the second month of embryonic life; at birth it is still rather narrow and only after the tenth year does it reach its complete development.

The mandibular bone:

An unpaired median bone of the splanchnocranium that constitutes the inferior portion of the facial skeleton. It articulates with the temporal bone through the temporomandibular joint (TMJ), the only diarthrosis of the skull, whose complex biomechanics give the bone a wide freedom of movement. Along its superior margin, the alveolar process houses the teeth of the lower arch.

The mandible consists of:

- Body: a horseshoe-shaped lamina with anterior convexity. It presents an external surface, an internal surface, and two margins: the inferior one (base) and the superior one, which houses the alveolar process. The latter, similarly to the maxilla, contains the teeth and tends to undergo physiological resorption in elderly or edentulous individuals.
- Ascending rami: two vertical quadrangular laminae that join the body forming the angle of the mandible. The amplitude of the latter varies with age, tending to be more obtuse in childhood and in the edentulous elderly.

Each ramus presents:

- Two surfaces: the lateral surface hosts the insertion of the masseter muscle, while the medial surface presents the spine of Spix (lingula).
- Two superior processes, separated by the mandibular notch:
  - Coronoid process: anterior, insertion site for the temporalis muscle.
  - Condyloid process: posterior, whose apex (condyle) constitutes the articular segment of the TMJ.

Anterior projection:

The external surface presents centrally the mandibular symphysis, which ends inferiorly in the mental protuberance. Lateral to it, at the level of the premolars, opens the mental foramen (passage for mental vessels and nerve), the outlet of the mandibular canal. Continuing posteriorly originates the oblique line, which runs toward the coronoid process delimiting, together with the molars, the buccinator groove for the muscle of the same name.

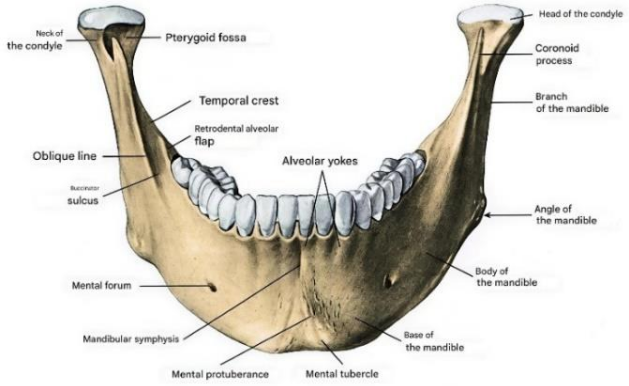

Figure 6: *Anterior projection of the mandible*

Posterior projection:

The internal surface, concave, presents centrally the mental spines (superior for the genioglossus muscle, inferior for the geniohyoid muscle). The mylohyoid line crosses the bone obliquely, giving insertion to the mylohyoid muscle (floor of the mouth) and delimiting two glandular areas: the sublingual fossa (superior) and the submandibular fossa (inferior).

The inferior margin hosts the digastric fossa, while the superior margin (alveolar part) presents the dental alveoli separated by interalveolar septa and, for multirooted teeth, by interradicular septa.

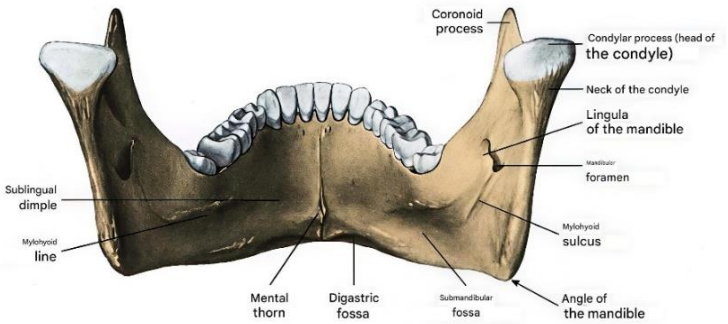

Figure 7: *Posterior projection of the mandible*

Lateral projection:

External surface: on the body the alveolar jugums are evident, prominences determined by the presence of dental roots. The ramus presents inferiorly the masseteric tuberosity, insertion site for the muscle of the same name.

Internal surface: inferiorly shows the pterygoid tuberosity (medial pterygoid muscle). In the center opens the mandibular foramen, protected by the lingula (spine of Spix), a landmark for anesthesia of the inferior alveolar nerve. From the foramen originates the mylohyoid groove for the nerve of the same name. Behind the last molar, delimited by the oblique line and the temporal crest, lies the retromolar trigone/retromolar fossa, which allows communication between the vestibule and the oral cavity.

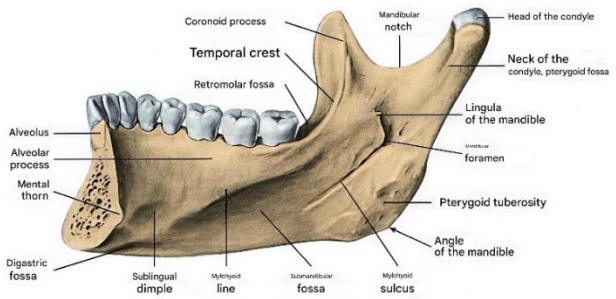

Figure 8: *Lateral projection internal surface.*

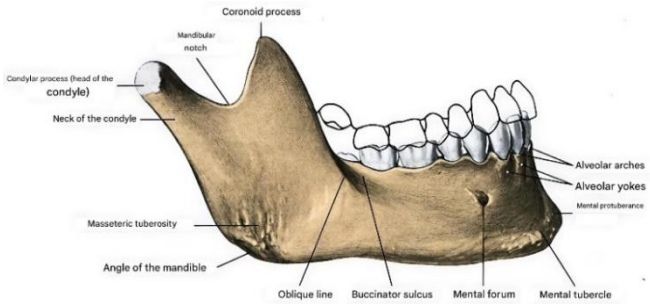

Figure 9: *Lateral projection external surface.*

1.4. Alveolar bone

Bone tissue represents a dynamic and highly specialized structure of the human body, responsible for mechanical support, organ protection, hematopoietic function, and maintenance of mineral homeostasis. Within the craniofacial district, the maxillary bone and the mandible present peculiar morphological, functional, and embryological characteristics compared with the rest of the skeleton, deriving predominantly from the cranial neural crest and developing through intramembranous ossification. Within these structures, alveolar bone represents a highly specialized portion directly related to the presence and function of the dental elements. [1,8]

Alveolar bone constitutes one of the four fundamental components of the periodontium, together with gingiva, root cementum, and periodontal ligament, and plays a crucial role in dental anchorage and in the distribution of occlusal forces generated during mastication and intercuspation. Its loss or alteration significantly compromises oral function and the stability of the dental elements.

From an anatomical point of view, the maxilla and mandible of the adult can be divided into two main components: a basal portion, not involved in housing the dental roots, and the alveolar process, responsible for the formation and support of the dental alveoli. This distinction is fundamental, since the alveolar process is a tooth-dependent bony structure, which develops, changes, and regresses in close relation to the presence of the dental elements. [1,8,9]

Structure of the alveolar process

From a structural point of view, the alveolar process consists of two main components:

- *Alveolar bone proper* (also known as the lamina dura): it is a thin layer of compact bone lining the wall of the dental alveolus. Its thickness generally ranges from 0.1 to 0.5 mm (about 200–500 μm) and it is characterized by the presence of a high quantity of Sharpey's fibers, terminal portions of the periodontal ligament fibers that insert perpendicularly into the bone matrix, allowing the functional anchorage of the tooth to the skeleton. This bony portion presents a predominantly lamellar and bundle bone structure, with a system of Volkmann's canals that allow the passage of blood vessels, lymphatic vessels, and nerve fibers between the periodontal ligament and the marrow spaces. [1,8,10,11]
- *Supporting alveolar bone*: instead consists of the buccal and lingual/palatal cortical plates and of the trabecular (cancellous) bone interposed between the alveolar bone proper and the cortical plates. This compartment contributes significantly to the mechanical resistance of the alveolar process and to the dissipation of functional forces. [8]

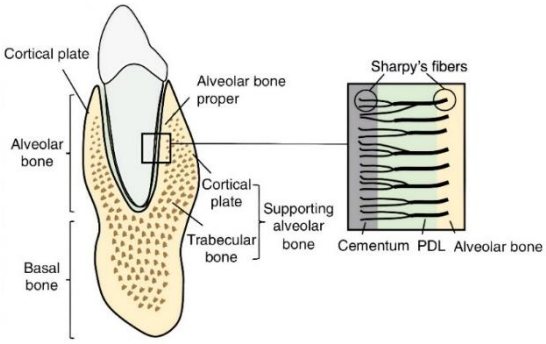

Figure 10: *Schematic representation of the supporting apparatus of the tooth [8]*

Embryological development and tooth dependence

The development of alveolar bone is closely related to odontogenesis. It originates from the dental mesenchyme derived from the cranial neural crest, in particular from the dental follicle that surrounds the developing tooth germ. During the late bell stage, bony septa and bridges begin to form, separating the individual tooth germs and creating distinct bony compartments. [1,8]

With the beginning of root formation and tooth eruption, the cells of the dental follicle differentiate into cementoblasts, periodontal ligament fibroblasts, and osteoblasts responsible for the formation of the alveolar bone proper. This process occurs in a coordinated manner with the formation of cementum and the periodontal ligament, making the morphology of the alveolar bone closely dependent on the shape, size, and orientation of the dental roots. [12,13]

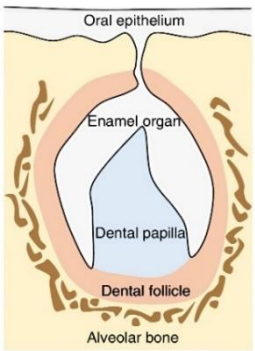

Figure 11: *Schematic representation of alveolar bone development*

Bone remodeling and tooth eruption

Tooth eruption is a complex biological process that requires continuous remodeling of the alveolar process, based on a delicate balance between bone resorption and new bone formation. During this phase, osteoclastic resorption allows enlargement of the gubernacular canal, enabling the erupting tooth to emerge from the bony crypt,

whereas the deposition of new bone at the apical level contributes to the generation of eruptive force. [14,15]

The dental follicle plays a central role in the regulation of these events, coordinating the activity of osteoblasts and osteoclasts through the secretion of specific biological mediators, including colony-stimulating factor-1 (CSF-1), epidermal growth factor (EGF), and several interleukins with pro-osteoclastogenic activity. The presence of tartrate-resistant acid phosphatase (TRAP)-positive osteoclast precursors within the follicular tissue confirms the importance of this compartment in controlling bone resorption during tooth eruption. [16-21]
These mediators act predominantly through the main molecular systems regulating osteoclastogenesis, including the RANK/RANKL/OPG axis, which represents the key mechanism of bone remodeling also in adult alveolar bone. [8]

Bone remodeling, understood as the process through which mature bone is continuously replaced, is essential for the maintenance of mineral homeostasis and for the repair of structural microdamage. In the adult, about 10% of the entire skeleton is renewed annually thanks to the coordinated action of osteoclasts, osteoblasts, and osteocytes. Under physiological conditions, the amount of bone resorbed by osteoclasts is balanced by the amount of new bone formed by osteoblasts, according to a mechanism known as coupling, which ensures maintenance of net bone mass. Osteoclasts, in addition to performing a resorptive function, play an active role in controlling the formative phase of remodeling through the release of factors capable of recruiting and stimulating pre-osteoblasts. [8]

Numerous pieces of evidence suggest that osteoclasts do not constitute a functionally homogeneous cell population, but rather present site-specific characteristics. In particular, cells from maxillary bone marrow show a greater capacity to generate osteoclasts and a higher resorptive activity than those from long bones, especially in relation to the substrate on which resorption occurs. These differences seem to be related to the peculiarities of the extracellular matrix of maxillary and alveolar bone, which presents a distinct composition compared with that of long bones, as well as to possible cell-intrinsic differences in the osteoclasts themselves. Supporting this hypothesis, it has been shown that the resorptive activity of craniofacial osteoclasts depends on both cysteine proteinases and matrix metalloproteinases (MMPs), whereas

in long-bone osteoclasts resorption is mediated predominantly by cysteine proteinases. [8]

A distinctive characteristic of alveolar bone is its high turnover. Experimental studies have shown that the rate of bone formation in maxillary and mandibular alveolar bone is three to six times higher than that observed in long bones, such as the femur. This rapid remodeling seems to be closely related to mechanical stimulation exerted during mastication. According to the mechanostat model, bone is able to adapt its mass and architecture in response to the magnitude, duration, and frequency of the mechanical strains to which it is subjected. In particular, dynamic loading is more effective than static loading in inducing an anabolic response, stimulating bone formation and reducing osteoclastogenesis. [8]

Osteocytes, embedded within the bone matrix, represent the main mechanosensitive cells involved in transducing mechanical stimuli into a biological response. They regulate bone remodeling both through cell-cell contact and through the release of soluble factors, including sclerostin and Dickkopf-1 (DKK-1), potent inhibitors of the Wnt/β-catenin pathway. Mechanical loading reduces the expression of sclerostin and DKK-1, favoring bone formation, whereas mechanical unloading increases their production, resulting in reduced osteoblastic activity and increased bone resorption. In alveolar bone, a hard diet and masticatory stimulation have been associated with reduced expression of sclerostin, suggesting a protective role of functional loading against bone loss. [8]

Under pathological conditions, however, mechanical stress may contribute to the progression of bone resorption. In periodontal disease, excessive occlusal forces increase RANKL expression in the periodontium and accelerate alveolar bone resorption. Moreover, mechanical stimulation in the presence of bacterial infection can amplify the local inflammatory response, promoting the production of pro-inflammatory cytokines and favoring alveolar bone loss. These observations highlight how alveolar bone remodeling is the result of a complex integration between biological and mechanical signals, which gives this skeletal district unique characteristics compared with the rest of the skeleton. [8]

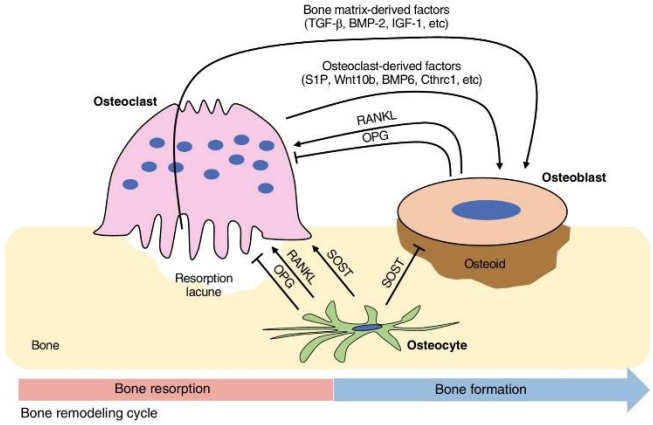

Figure 12: *Diagram of the cellular interactions that regulate bone tissue remodeling. Osteoblasts and osteocytes synthesize RANKL and osteoprotegerin (OPG). The binding of RANKL to the RANK receptor expressed on osteoclasts promotes their differentiation and functional activation. OPG instead acts as a soluble receptor that sequesters RANKL, preventing its interaction with RANK and thus limiting osteoclastogenesis. Osteocytes contribute to the regulation of bone metabolism by producing sclerostin (SOST), which suppresses bone formation and stimulates resorption. In addition, osteoclasts influence osteoblast recruitment and activity through factors released both by the cells themselves and by the lacunae generated during bone resorption.*

Regional anatomical differences and clinical implications

Numerous studies have shown that alveolar bone thickness (ABT) varies significantly according to the anatomical region, the tooth considered, and the arch involved. A recent meta-analysis including 68 studies showed that, in the anterior maxilla, the mean thickness of the buccal plate is generally reduced, with values ranging from 0.42 to 1.75 mm, whereas it tends to increase in the posterior sectors, where it can reach values between 0.78 and 4.31 mm. The palatal plate, on the other hand, shows a generally greater and more variable thickness, with values ranging from about 0.97 to over 8 mm.

Similarly, in the anterior mandible, alveolar bone thickness is generally greater on the lingual side than on the buccal side, with mean values ranging from 0.38 to 5.44 mm for the lingual cortex and from 0.4 to 3.71 mm for the buccal cortex, respectively. Also at the mandibular level, the posterior sectors show greater bone thickness both on the buccal side (0.66–6.31 mm) and on the lingual side (2.31–7.77 mm), confirming a non-uniform distribution of ABT along the dental arches.

These regional anatomical differences are of relevant clinical importance, particularly in implantology, orthodontics, and surgery. Areas characterized by thin bony walls, such as the anterior maxillary sectors, are in fact more susceptible to fenestration, dehiscence, and bone resorption phenomena, especially following invasive procedures or changes in functional loads. Detailed knowledge of the distribution of alveolar bone

thickness therefore represents a fundamental prerequisite for correct therapeutic planning and for the prevention of biological complications. [22]

Biological and clinical function of alveolar bone

The primary function of the alveolar process is to house and anchor the dental roots, while at the same time allowing the absorption and distribution of occlusal forces through the insertion of periodontal ligament fibers into the alveolar bone proper. However, this function is closely linked to the presence of teeth; indeed, following their loss, the alveolar process undergoes progressive atrophy and resorption, losing its function and part of its structure.

For this reason, a thorough understanding of the biology, structure, and remodeling of alveolar bone represents a fundamental prerequisite for the prevention and treatment of periodontal diseases, for implant planning, and for the development of targeted regenerative strategies. [1,8]

1.5. Bone resorption/bone atrophy

Functional role of alveolar bone and consequences of tooth loss:

Alveolar bone represents the most dynamic and “labile” component of the periodontium, since it is subject to continuous remodeling in response to the mechanical and functional stimuli exerted by the natural dentition and occlusal forces, which influence not only the “quantity” but also the “quality” of the available bone. [23] The loss of one or more dental elements, due to extraction or trauma, in fact determines the loss of physiological intraosseous stimulation and triggers a sequence of biological and morphological events that progressively modify the architecture and dimensions of the alveolar ridge, with functional, esthetic, and rehabilitative implications. [23] Under edentulous conditions, in addition to psychological repercussions, stomatognathic, phonetic, masticatory, and esthetic functions are compromised, while the maxillofacial district tends to develop anatomical alterations typical of senescence, with changes affecting soft and hard tissues and biomechanical adaptations of the TMJ and intermaxillary relationships. [24]

Anatomy of alveolar bone and biological bases of remodeling:

From an anatomical point of view, the maxilla and mandible include a basal component (formed during fetal life and the site of the main muscular insertions) and an alveolar component (developed with tooth eruption and an integral part of the

periodontal system), with the consequence that tooth loss primarily affects the alveolar bone, whereas basal bone tends to preserve its morphology to a greater extent unless irritative stimuli or incongruous loads occur. [24] In biological terms, the dimensional stability of bone is “dynamic,” resulting from the continuous balance between apposition and resorption, and Wolff’s law describes how every variation in function is translated into modifications of the internal architecture and external configuration of bone. [24]

Healing of the post-extraction socket and ridge remodeling:

The lack of post-extraction mechanical stimuli induces a reduction in trabeculation, local bone density, and a rapid contraction of the buccolingual dimension, followed later by a vertical reduction, progressively configuring an atrophy of the residual ridge. [24] The healing process of the post-extraction socket, although leading to the deposition of bone tissue in the space previously occupied by the root, does not correspond to a restitutio ad integrum of the original ridge dimensions, because at the same time as intra-alveolar bone formation, remodeling occurs with loss of crestal volume. [25]

Bone regeneration is based on the activity of osteogenic progenitor cells of osteoblasts, present in the medullary stroma close to blood vessels and in the bone linings (endosteum and periosteum), including “determined” cells capable of forming bone without inductive agents and inducible cells that instead require osteogenic signals to differentiate. [25]

In this context, it has historically been demonstrated that the insertion of inductive agents such as decalcified bone matrix or bone morphogenetic proteins into heterotopic tissues can promote osteogenesis, but the newly formed bone proves unstable over time in the absence of continuous stimulation and cellular recolonization. [25]

Biological phases of alveolar healing:

Socket healing follows sequential phases: formation of a stable blood clot as the initial “scaffold,” cellular infiltration and controlled inflammatory response, development of granulation tissue with neoangiogenesis, deposition of osteoid initially in the apical area and progressive mineralization with replacement by more mature bone, up to a restructuring process that may require several months. [25]

Dimensional modifications of the alveolar ridge:

Even when the socket heals without complications, vertical height is normally not completely restored in comparison with adjacent teeth, and remodeling results in a narrower ridge often relocated in a lingual/palatal direction, with predominantly horizontal loss and greater involvement of the buccal aspect. [25]

From a quantitative point of view, a systematic review showed that after extraction clinically relevant mean dimensional changes can be expected, with buccolingual loss generally greater than vertical loss and with the initial phase of healing (first months) accounting for the largest proportion of dimensional ridge changes. [25]

Bone quality and implant implications:

At the same time, histological observations have indicated that in the first 8–12 post-extraction weeks the socket may present a coexistence of mature bone and osteogenic tissue and that filling of the undisturbed socket may be completed in approximately 100 days, although with modifications in trabecular composition and orientation compared with the pre-extraction condition. [23] It has also been described that spontaneously healed sockets may contain portions of woven bone and areas with empty osteocytic lacunae, associated with reduced osteoblastic activity and increased osteoclastic activity, elements that underline how the "quality" of post-extraction bone is not automatically superimposable on the original one. [23]

Since the trabecular component, porosity, and microarchitectural organization influence load response and biomechanical stability, these modifications have a direct impact on planning and outcomes of implant therapy, especially with regard to primary stability and management of loading protocols. [23] In fact, bone quality has historically been considered a crucial determinant of osseointegration, and early studies reported lower survival rates in some regions, such as the posterior maxilla, although today these differences are attenuated by progress in implant design, surface treatment, and understanding of biomechanics. [23]

However, it remains essential to distinguish mechanical primary stability, necessary to initiate biological integration, from the simplistic concept of "better bone = denser bone," because excessive torque may induce microfractures, areas of suffering osteocytes, and greater peri-implant resorption, whereas apparently less dense bone

may offer a favorable biological potential thanks to the greater non-mineralized and vascularized component. [23]

From this perspective, bone microarchitecture does not depend only on the anatomical site, since intra-site variability can be wide and factors such as the degree of atrophy negatively influence parameters such as trabecular volume, suggesting that evaluation should be individualized, for example through CBCT, rather than based exclusively on the region (maxilla vs mandible; anterior vs posterior). [23]

The different distribution of bone density in the arches has been schematized by clinical classifications, including Misch's classification, which describes densities from D1 to D4/D5 and frequently places less dense bone in the posterior maxillary regions and denser bone in the mandibular areas, while recognizing that intermediate types may occur in a not strictly predictable way. [23]

Cellular and molecular mechanisms of bone resorption:

At the biological level, remodeling and resorption are supported by osteoclastic activity, mediated by multinucleated cells derived from the hematopoietic lineage and regulated mainly by the M-CSF/RANKL-RANK axis, with activation of specific transcriptional pathways (c-Fos, NFATc1) and production of enzymes necessary for degradation of the mineralized and organic matrix, while inflammatory cytokines may enhance osteoclastogenesis especially under pathological conditions. [8] In the alveolar district, moreover, gingival fibroblasts and periodontal ligament cells contribute to the local regulation of osteoclastic activity through the RANKL/OPG balance, and in inflammatory conditions such as periodontitis immune cells may also amplify alveolar bone resorption. [8] Osteoclastic resorption occurs through acidification of the resorption compartment and proteolysis of the matrix, requiring specialized structures such as the sealing zone and ruffled border, with modalities that may produce resorption pits or channels, suggesting variable osteoclastic behavior according to the microenvironment and biological context. [8]

Patterns of resorption in the maxillary and mandibular arches:

From a clinical-morphological point of view, post-extraction remodeling tends to be more evident on the buccal aspect, where the cortex is often thinner and therefore less resistant to resorption, whereas the thicker palatal/lingual cortices remain relatively more coronal, with displacement of the crestal center toward the palate/tongue and

reduction first in the transverse and then in the vertical dimension. [26] In cases of extended or total edentulism, these modifications become systemic for the entire maxillofacial complex, altering interarch relationships in the three planes of space and progressively favoring a tendency toward pseudo-Class III skeletal relationship, with increased interarch distance and potentially unfavorable crown/implant ratios. [24]

In particular, the upper maxilla tends to resorb in a centripetal direction with progressive contraction of the arch and frequent association with maxillary sinus pneumatization in the posterior regions, whereas the mandible shows a more centrifugal behavior, with predominantly horizontal resorption in the symphyseal region and more vertical resorption in the posterior sectors. [24] In the long term, longitudinal studies indicate that most bone loss occurs early, but the process may continue slowly over time, with wide individual variability related to systemic factors (hormonal profile and bone metabolism, osteoporosis/osteomalacia, drugs) and local factors (traumatic extractions, incongruous prostheses with chronic irritative stimulus and periosteal ischemia, surgery with mucoperiosteal flaps, long-standing edentulism). [24]

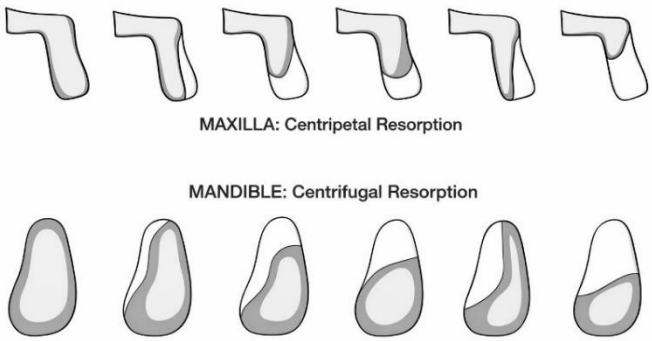

Figure 13: *Resorption pattern of the maxillary and mandibular arches.*

Classifications of atrophy and evaluation of bone density:

In order to make the assessment of atrophies reproducible and comparable and to guide surgical-prosthetic planning, numerous classifications have been proposed, based on morphological parameters (quantity and shape of the ridge) or qualitative parameters (density/internal structure), each with different clinical purposes. [24]

Cawood and Howell's classification describes the morphological evolution of the edentulous ridge in progressive classes, from the presence of dentition to knife-edge ridges, flat ridges, and depressed ridges with involvement of basal bone, highlighting that resorption patterns follow relatively predictable models but with variability related

to age, sex, and skeletal morphology. [24] In parallel, bone quality/density classifications such as Lekholm and Zarb's and Misch's classification distinguish sites with a greater cortical component (more resistant but less vascularized) from sites with a greater trabecular component (less mechanically resistant but potentially more biologically favorable), introducing a language useful for the choice of surgical protocol, implant selection, and definition of loading times.

Objective evaluation of density may be supported by three-dimensional imaging and radiological quantification through Hounsfield units, which allow estimation of radiopacity and correlation with density classes useful for planning, although intraoperative evaluation remains a clinical parameter influenced by experience and cutting resistance. [24]

Clinical implications of alveolar bone resorption:

Ultimately, post-extraction alveolar bone resorption is a physiological but clinically determinant phenomenon, because socket healing does not coincide with preservation of crestal volume, and dimensional and qualitative changes in bone may limit the ideal implant position, compromise the esthetics of peri-implant tissues, and make targeted reconstructive interventions necessary. [23] Precisely for this reason, modern implant-prosthetic planning cannot be limited to describing resorption, but must consider preventive and corrective strategies to preserve or regenerate alveolar bone, integrating the understanding of biological mechanisms and atrophy patterns with the rational choice of surgical techniques and biomaterials.

1.6. Materials for alveolar ridge preservation (ARP) and/or bone regeneration

Following tooth extraction, the loss of functional stimuli determines a physiological remodeling of the alveolar bone with reduction of ridge volume, a condition that may compromise prosthetic-implant planning and require additional reconstructive procedures. In this context, alveolar ridge preservation (ARP) was developed with the aim of minimizing post-extraction bone loss, preserving both the hard and soft tissues of the socket, thus facilitating future implant placement and improving esthetics, especially in the anterior sectors. ARP also aims to reduce the need for more complex reconstructive procedures, increasing the predictability of implant therapy and promoting more rapid healing toward definitive rehabilitation. [27]

More broadly, regenerative procedures in dentistry and oral/maxillofacial surgery include applications such as socket preservation, ridge augmentation, maxillary sinus lift, and periodontal surgery, in which the choice of biomaterial depends on clinical factors such as defect size, shape, and volume, local and general patient conditions, and the goals of rehabilitation. [28] In edentulous jaws or atrophic ridges, insufficient bone volume can make correct implant placement difficult or impossible; in such scenarios, reconstructive techniques are used (including grafting procedures and GBR) aimed at restoring a ridge volume adequate for subsequent mechanical loading.

Biological requirements and principles of graft healing:

A bone regeneration material should ensure biocompatibility and support bone formation through the three key properties: osteoconduction, osteoinduction, and osteogenesis. Osteoconduction is the ability to act as a scaffold for vascular and cellular colonization and progressive replacement with newly formed bone, whereas osteoinduction implies the ability to induce the differentiation of mesenchymal cells into osteoblasts, also through biochemical mediators such as BMPs; osteogenesis, on the other hand, corresponds to the production of new bone by vital cells already present in the graft (a typical feature of autologous bone). [28,29]

From a biological point of view, the engraftment of a non-vascularized graft follows sequential phases (initial hematoma, inflammatory response, centripetal vascular invasion, bone deposition, and remodeling), which are influenced by mechanical stability, graft microarchitecture and the revascularization capacity of recipient bed.

Classification of materials:

The materials used in ARP and bone regeneration can be classified, according to their origin, into autografts, allografts, xenografts, and alloplastic/synthetic materials, with the possibility of association with membranes or biological adjuvants. [28,29]

- Autologous bone (autograft): it is traditionally considered the gold standard because it can simultaneously express osteoconduction, osteoinduction, and osteogenesis, with the absence of immunological compatibility problems. However, its use involves donor site morbidity, increased surgical time and complexity, and possible local complications; moreover, the quantity and quality of available bone may be limited in relation to age and comorbidities. In dentistry, its use therefore tends to be reserved for more complex cases or extensive defects,

also as a function of the limited availability of intraoral bone and the need for a second surgical site. [28,29]

In reconstructive protocols, the choice of harvesting site (intraoral vs extraoral) depends on the extent of the defect and the characteristics required of the graft (cancellous, corticocancellous, or predominantly cortical).

- Allografts: they derive from donors of the same species and are available through bone banks after selection, treatment, and preservation processes. They are considered predominantly osteoconductive and, under some conditions, weakly osteoinductive (if growth factors remain after processing), but they do not express osteogenesis; moreover, there remain considerations regarding processing costs and infectious/immunological risks, although these are reduced by modern control and treatment procedures. [28,29]
- Xenografts (xenograft): often of bovine or porcine origin, they are used as biocompatible scaffolds with marked osteoconduction, thanks to the mineral component (mainly HA) and to a microstructure that can favor vascular and cellular colonization. One aspect frequently considered is their slower resorption, which may maintain space and volume for longer, but may also result in persistence of residual particles. Among the disadvantages are ethical/religious issues and the need for preparation processes aimed at reducing antigenicity; the issue of interspecies disease transmission is also discussed, albeit as a rare risk. [28,29]
- Synthetic/alloplastic biomaterials: they are designed to promote bone regeneration by offering advantages such as high availability, reproducibility, sterilizability, ease of handling, and, in some cases, injectability and moldability, reducing the need for a donor site. In general, the main groups include calcium phosphates, calcium sulfates, bioactive glasses, and polymers, each with different profiles of degradation, structural stability, and biological interaction. Calcium phosphates, in particular, are widely used because of their similarity to the mineral phase of bone and their high biocompatibility, although they have limitations related to absent or reduced osteoinductivity in defects and to mechanical properties that are not always optimal.

Membranes and principles of guided regeneration (GBR) in ARP:

In ARP and, more generally, in guided bone regeneration, the use of barrier membranes is intended to protect the clot and/or the biomaterial, preventing soft tissue invasion into the defect and creating a space favorable to bone regeneration. Collagen membranes, often bioresorbable, are used both in association with bone substitutes and as site protection devices; in several clinical experiences the "graft + membrane" association has shown smaller dimensional ridge changes compared with the use of membrane alone. A historical limitation of membranes, especially non-resorbable ones, has been the risk of exposure and infection and the need for a second surgery for removal; this has stimulated the search for combinations of materials with better clinical management. [27] From a technical point of view, in socket preservation procedures, one critical issue is the competition between bone integration and epithelial invagination, which is why the barrier assumes a key role in protecting the grafted material during the early healing phases.

Platelet concentrates and biological adjuvants:

In recent years, attention has also shifted toward biological adjuvants capable of improving the healing environment. Platelet concentrates, particularly PRF (and its variants), are described as autologous biomaterials rich in growth factors and cellular components within a fibrin matrix, with potential support for tissue healing and regeneration, and with evidence of increased bone formation compared with spontaneous healing in some ARP contexts. In general, these approaches are frequently proposed in combination with graft biomaterials, with the aim of favoring early vascularization and improving soft tissue management, although this remains an area in which standardized protocols and long-term clinical data are required. [27,29]

Innovative biomaterials:

The evolution of biomaterials for ARP and bone regeneration is including technologies that aim to reproduce the bone microenvironment more faithfully. One example of this direction is the development of injectable materials, capable of adapting to the geometry of the defect and stabilizing in situ, offering a scaffold for cell adhesion, proliferation, and differentiation.

At the same time, 3D printing and the design of "patient-specific" scaffolds represent a further step toward personalized treatments, potentially able to improve adaptation to the defect and clinical predictability. [27]

Within the framework of composite materials, solutions are being explored that combine mineral phases and polymeric or collagenic components to improve mechanical strength, porosity, and biological performance, with the aim of optimizing the balance between volume maintenance and replacement with newly formed bone. [29]

Clinical considerations:

In clinical practice, no material fully satisfies all ideal requirements in every situation; the choice must therefore be guided by defect size and morphology, required healing times, systemic and local patient conditions, and the need for mechanical stability. [28,29]

In general, materials with slower resorption may favor volume maintenance, whereas more resorbable materials may be associated with faster replacement, with possible implications for dimensional stability over time; for this reason, combinations of biomaterials, membranes, and biological adjuvants are often proposed according to the clinical objective. Furthermore, management of clot and biomaterial stability, protection from soft tissues, and control of complications (membrane exposure, infection, material migration) represent determining aspects for the outcome of ARP and for subsequent implant stability. [27,29]

The current landscape of biomaterials for alveolar preservation and bone regeneration therefore shows a continuum ranging from traditional grafts (autologous, allogeneic, and xenogeneic) to synthetic substitutes and composite and bioactive systems, with growing attention toward manageable, reproducible, and defect-adaptable solutions.

In this context, particular interest has been directed toward calcium phosphate-based cements, synthetic biomaterials characterized by high biocompatibility and a composition similar to the mineral phase of bone, whose properties can be further optimized through compositional modifications and ionic doping strategies aimed at improving their biological and regenerative performance. [28,29]

1.7. Calcium phosphate-based cements, with a focus on brushite and its doping

In the context of bone regeneration, bone cements represent a class of biomaterials developed to overcome the limitations of traditional grafts and to improve the management of bone defects of different origins. These materials are generally composed of a mixture of powders and a liquid phase which, once mixed, give rise to a moldable paste capable of hardening in situ through a chemical setting reaction, allowing the material to adapt to the bone defect and facilitating its use in the surgical and dental fields. [30]

Interest in bone cements mainly derives from the possibility of obtaining materials with chemical and biological characteristics similar to the mineral component of human bone, thereby favoring integration with the host tissue and the formation of new bone tissue. [30] In order to be successfully used in the clinical setting, these materials must meet several requirements, including biocompatibility, bioactivity, osteoconductivity, and controlled resorption capacity, as well as possessing adequate mechanical and structural properties such as porosity, crystallinity, and surface roughness. [31]

Among the different types of bone cements available, calcium phosphate cements (CPCs) play a particularly relevant role thanks to their chemical composition, which faithfully reproduces the mineral phase of natural bone. This characteristic gives calcium phosphate-based materials excellent biocompatibility, bioactivity, and osteoconductive properties, making them particularly suitable for bone regeneration applications and for the reconstruction of skeletal defects. [32]

Calcium phosphate cements are generally obtained by mixing one or more calcium phosphate powders with an aqueous liquid phase; during the setting reaction, a process of reagent dissolution followed by re-precipitation of the final crystalline phase occurs, with the formation of a solid structure that adapts to the bone defect. [33] Depending on the composition and reaction conditions, the final product may be mainly represented by two different phases: an apatitic phase, similar to hydroxyapatite, or a calcium hydrogen phosphate dihydrate-based phase known as brushite. [34]

Brushite ($CaHPO_4 \cdot 2H_2O$) represents one of the most important calcium phosphates used in the biomedical field for bone tissue repair and regeneration applications. [35,36] It is characterized by greater solubility than the apatitic phases and by a faster

resorption capacity under physiological conditions, properties that favor the progressive replacement of the material with new bone tissue during the healing process. [37]

Numerous in vitro and in vivo studies have shown that brushite possesses osteoconductive properties and can promote the proliferation and differentiation of osteogenic cells, contributing to the formation of new bone tissue. [38] Moreover, its high solubility allows the controlled release of calcium and phosphate ions during the degradation process, contributing to the mineralization of the surrounding tissue. [37]

Despite these favorable characteristics, brushite-based cements also present some limitations, including relatively low mechanical strength and degradation that is sometimes difficult to control, aspects that may limit their application in large bone defects or in defects subjected to high loads. [39] In addition, a further critical issue concerns the absence of intrinsic antibacterial properties, which may favor the onset of post-operative infections at the implantation site. [40]

To overcome these limitations, in recent years several strategies have been developed to modify calcium phosphate-based cements, including the incorporation of drugs, bioactive molecules, or metal ions capable of modulating the biological and physicochemical properties of the material. [40] Among the most promising approaches is ionic doping of the crystalline structure of calcium phosphates through the introduction of bioactive elements such as zinc, silver, copper or strontium. [41-43]

In particular, zinc (Zn^{2+}) plays a fundamental biological role in bone metabolism, since it is involved in the proliferation and differentiation of osteoblasts and in the regulation of bone tissue formation. [44,45] Moreover, numerous studies have shown that the incorporation of Zn^{2+} ions into calcium phosphate-based biomaterials can improve the osteogenic properties of the material and confer antibacterial activity against different microorganisms. [46,47]

Ionic doping also makes it possible to modulate important parameters such as crystallinity, solubility, and material degradation rate, significantly influencing the biological behavior of bone cements and their interaction with host tissue cells. [48]

In light of these considerations, brushite-based cements doped with metal ions currently represent a promising class of biomaterials for bone tissue engineering

applications, capable of combining biocompatibility, resorbability, and improved bioactive properties compared with traditional materials. [49]

1.8. Application of calcium phosphate-based cements in 3D printing

In recent years, the development of additive manufacturing technologies has opened new perspectives in the field of bone tissue engineering, allowing the production of three-dimensional scaffolds designed to mimic the structure and properties of natural bone tissue. In particular, three-dimensional printing (3D printing) represents one of the most promising technologies for the fabrication of customized scaffolds intended for bone regeneration.

3D printing is based on an additive manufacturing process in which the material is deposited layer by layer following a digital model obtained through computer-aided design (CAD) systems. This approach makes it possible to create highly precise three-dimensional structures that can be adapted to the shape and size of the patient's bone defect. [50,51]

In the field of bone tissue engineering, scaffolds produced by 3D printing act as a temporary framework capable of supporting the adhesion, proliferation, and differentiation of osteogenic cells, favoring the formation of new bone tissue and the progressive replacement of the material with regenerated tissue. [52]

In order for a scaffold to effectively perform this function, it is necessary for it to exhibit some fundamental characteristics, including an interconnected porous structure that allows nutrient diffusion, waste product removal, and cell migration within the structure. [53] In particular, for bone tissue engineering, pore sizes between about 100 and 300 μm have been shown to promote both osteogenesis and angiogenesis, contributing to the formation of functional bone tissue. [54]

Different biomaterials can be used as components for scaffold fabrication by 3D printing. Among these, three main categories can be distinguished: polymers, bioceramics, and composite materials. [55]

Polymers represent a particularly versatile class of materials, since they allow the mechanical properties and degradability of the scaffold to be modulated through changes in their chemical structure. [56] Among the synthetic polymers most widely used for 3D printing of bone scaffolds is polycaprolactone (PCL), a biodegradable

material characterized by a low melting point and good mechanical stability, which makes it particularly suitable for fabrication processes by extrusion. [57]

Bioceramics, including calcium phosphates and bioactive glass, are instead inorganic materials with high bioactivity and the ability to bond directly to bone tissue. However, their brittleness and limited mechanical strength often make it necessary to use them in combination with polymeric materials. [58-61]

For this reason, in recent years the use of polymer-ceramic composite materials has been proposed, in which the polymer phase provides mechanical support and flexibility, while the ceramic phase contributes to improving the bioactivity and osteoconductivity of the scaffold. [62] A particularly studied example is the combination of PCL with calcium phosphate-based bioceramics, which makes it possible to obtain scaffolds with improved mechanical and biological properties compared with the individual materials. [62]

The use of 3D printing in the fabrication of bone scaffolds also offers the possibility of producing patient-specific customized structures, improving the adaptation of the material to the anatomical defect and potentially helping to improve the clinical outcomes of reconstructive procedures. [63]

These technologies therefore represent an important advancement in the field of regenerative medicine and cranio-maxillofacial surgery, allowing the development of increasingly sophisticated and functionalized biomaterials for advanced clinical applications. [64]

1.9. Thesis rationale

Despite the significant progress made in the field of biomaterials for bone regeneration, research continues to be directed toward the development of materials capable of combining biocompatibility, bioactivity, adequate mechanical properties, and the ability to promote rapid and effective bone regeneration.

Calcium phosphate-based cements represent one of the most promising solutions in this field, owing to their chemical similarity to the mineral component of bone and their ability to support osseointegration and osteoconduction processes. [65] However, these materials still present some limitations, including relatively modest mechanical properties and limited intrinsic antibacterial activity, which may compromise the clinical success of implants. [40]

In order to improve the biological performance of these materials, a particularly promising strategy consists of the ionic doping of calcium phosphates with bioactive elements capable of modulating the cellular response and biological behavior of the material. Among these elements, zinc (Zn^{2+}) has attracted considerable interest due to its role in bone metabolism and its ability to stimulate osteoblast proliferation and differentiation. [44,45] Moreover, the incorporation of Zn^{2+} ions into the crystalline structure of calcium phosphate-based cements may confer antibacterial properties to the biomaterial, contributing to a reduction in the risk of post-operative infections at the implantation site. [46]

At the same time, the integration of these biomaterials with additive manufacturing technologies, such as 3D printing, offers the possibility of producing customized scaffolds designed to adapt to the specific anatomical features of the patient's bone defect, potentially improving the effectiveness of bone regeneration strategies. [63]

In this context, the use of composite materials that combine a bioactive ceramic phase, such as calcium phosphates, with a biodegradable polymeric component represents a particularly promising strategy. Among the synthetic polymers most widely used for tissue engineering applications is polycaprolactone (PCL), a material characterized by good biocompatibility, controlled degradation, and adequate mechanical properties for the fabrication of three-dimensional scaffolds using 3D printing techniques. [57] Indeed, the combination of a bioactive ceramic phase with a biodegradable polymer makes it possible to obtain composite materials capable of combining the osteoconductive properties of bioceramics with the greater processability and mechanical stability provided by the polymeric component. [62]

A further potential advantage of using resorbable brushite- and PCL-based scaffolds compared with metallic devices traditionally used in regenerative surgery, such as titanium meshes, is the possibility of avoiding a second surgical procedure for device removal. Titanium meshes are frequently used to maintain space and stabilize biomaterials during guided bone regeneration procedures; however, since they are non-resorbable materials, they generally require subsequent removal surgery once the regeneration process has been completed. The use of biodegradable scaffolds designed to progressively degrade and be replaced by newly formed bone tissue could therefore reduce surgical morbidity for the patient, simplifying the therapeutic pathway and improving the clinical management of bone defects.

In light of these considerations, the general aim of the present thesis was the development and preliminary characterization of composite materials based on Zn^{2+}-doped brushite and polycaprolactone, with a view to their possible future application in the fabrication of customized three-dimensional scaffolds for bone regeneration. In particular, brushite cements doped with different nominal concentrations of zinc, equal to 2%, 5%, and 10%, were prepared and subsequently combined with a biodegradable polymeric matrix consisting of PCL.

The main outcomes of this work were: the verification of the possibility of obtaining Zn^{2+}-doped brushite cements at different percentages; the evaluation of the effect of doping on the chemical and structural properties of the cements by XRD and FT-IR analyses; the preliminary evaluation of the mechanical properties of the cements by compression testing; the preparation of PCL/brushite-Zn^{2+} composites with an 80/20 weight ratio; the production of processable composite pellets and filaments; and the fabrication, by 3D printing, of samples intended for flexural mechanical testing and preliminary biological evaluations.

Furthermore, an additional experimental outcome was represented by the evaluation of the processability of the composite throughout the different operational phases, from material preparation to filament production, up to the 3D printing of discs and rectangular specimens. This aspect is particularly relevant because transforming a cement or ceramic powder into a printable composite material requires not only adequate chemical-structural and mechanical properties, but also sufficient workability during the mixing, extrusion, and deposition phases.

The proposed approach therefore aims to evaluate the feasibility of an integrated experimental pathway which, starting from the synthesis of Zn^{2+}-doped brushite, allows the obtainment of a PCL-brushite composite that can be transformed into filament and subsequently 3D printed. From this perspective, the present work fits within the development of resorbable and customizable composite biomaterials, potentially usable in the future for the fabrication of scaffolds intended for the regeneration of complex bone defects.

2. MATERIALS AND METHODS

This chapter describes the materials used and the experimental procedures adopted for the preparation, characterization, and preliminary evaluation of the materials investigated in this study.

The experimental activity was aimed at the development of composite materials based on zinc-doped calcium phosphates, subsequently processed by additive manufacturing techniques for the fabrication of three-dimensional samples intended for preliminary mechanical and biological testing, with a view to the possible future development of customized scaffolds for bone regeneration applications.

In particular, three different material formulations were developed in the present study, characterized by different nominal percentages of doping with Zn^{2+} ions (2%, 5%, and 10%), in order to evaluate the influence of zinc content on the properties of the biomaterial.

In the first phase, β-tricalcium phosphate (β-TCP) doped with Zn^{2+} ions was synthesized by a solid-state reaction starting from a mixture of inorganic precursors. Three different formulations of doped β-TCP were therefore obtained, characterized by nominal Zn^{2+} percentages of 2%, 5%, and 10%.

The materials thus obtained were subsequently used as starting reagents for the preparation of the corresponding zinc-doped brushite cements, obtained through the reaction between doped β-TCP, monocalcium phosphate monohydrate (MCPM), and distilled water. Trisodium citrate was also added to the liquid phase and used as a retarder of the brushite cement setting reaction.

In parallel with the zinc-doped formulations, a pure brushite formulation was also prepared and used as a control sample for the subsequent mechanical tests and characterization analyses.

The brushite cements obtained were initially subjected to preliminary mechanical compression tests. Subsequently, the samples were ground until a fine powder was obtained. Part of the resulting powder was stored for chemical and structural characterization analyses, in particular by FT-IR spectroscopy and X-ray diffraction (XRD), aimed at evaluating the chemical composition and crystalline phases of the material.

The remaining portion of the brushite powder was instead used for the preparation of a ceramic-polymer composite obtained by melt blending with polycaprolactone (PCL). The composite thus obtained was transformed into pellets and subsequently extruded to produce a filament suitable for three-dimensional printing processes.

Finally, the resulting filament was used for the fabrication, by 3D printing, of samples intended for flexural mechanical testing and preliminary biological evaluations. In particular, for each formulation, rectangular specimens (70 × 8 × 3 mm) were fabricated for mechanical testing, and cylindrical discs (18 × 0.8 mm) were fabricated for preliminary biological biocompatibility investigations.

The main steps of the experimental workflow adopted in the present study are summarized in the diagram shown in Figure 14.

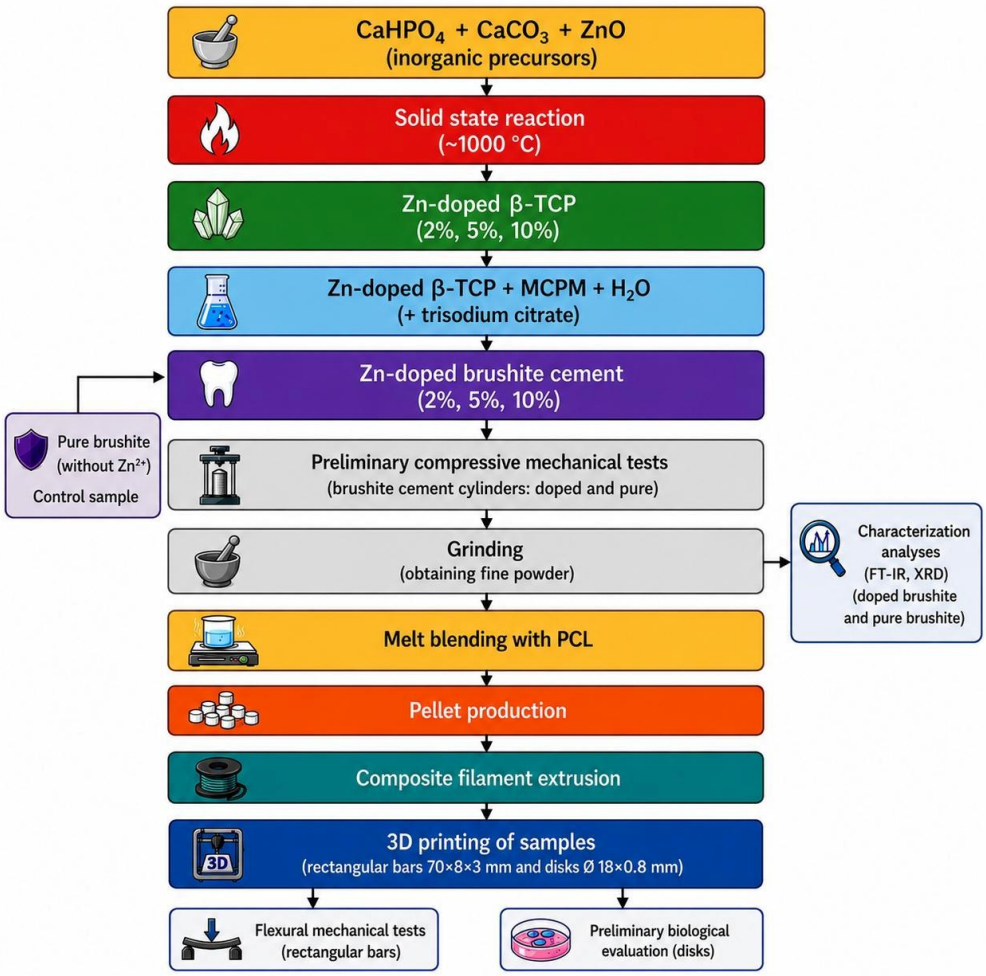

Figure 14: Scheme of the experimental workflow adopted in the present study, illustrating the main steps of synthesis of β-tricalcium phosphate (β-TCP) doped with Zn^{2+} ions, the preparation of doped and undoped brushite cements, preliminary mechanical compression testing, chemical-structural characterization by FT-IR and X-ray diffraction (XRD), production of the brushite-PCL composite, subsequent filament extrusion, and fabrication by 3D printing of samples intended for flexural mechanical testing and preliminary biological evaluations.

2.1. Materials

Several powder reagents were used for the preparation of the samples investigated in the present study. These reagents were employed for the synthesis of zinc-doped β-tricalcium phosphate (β-TCP), for the preparation of brushite cements, and for the subsequent fabrication of the brushite-PCL composite intended for 3D printing.

In particular, the following materials were used:

- Dibasic calcium phosphate;
- Calcium carbonate;
- Zinc oxide;
- Monocalcium phosphate monohydrate (MCPM);
- Trisodium citrate dihydrate;
- Distilled water;
- Polycaprolactone (PCL).

Dibasic calcium phosphate, calcium carbonate, and zinc oxide were used as precursors for the synthesis of zinc-doped β-tricalcium phosphate. The β-TCP obtained was subsequently used, together with monocalcium phosphate monohydrate (MCPM) and distilled water, for the preparation of the doped brushite cement. Trisodium citrate dihydrate was also added to the liquid phase and used as a retarder of the brushite cement setting reaction.

For the preparation of the ceramic-polymer composite, polycaprolactone (PCL), a biodegradable polymer, was instead used as the matrix for the production of the filament intended for additive manufacturing by 3D printing.

The main materials used in the present work, together with their respective suppliers and intended use, are reported in Table 1.

Reagent	Chemical formula	Supplier	Use
Dibasic calcium phosphate	$CaHPO_4$	La Farmochimica (Genoa, Italy)	Precursor for β-TCP synthesis
Calcium carbonate	$CaCO_3$	J.T. Baker (Mallinckrodt Baker B.V., Deventer, The Netherlands)	Precursor for β-TCP synthesis
Zinc oxide	ZnO	Merck	Source of Zn^{2+} ions for β-TCP doping
Monocalcium phosphate monohydrate	$Ca(H_2PO_4)_2 \cdot H_2O$	Scharlau	Reagent for brushite formation
Distilled water	-	-	Liquid phase of the cement
Trisodium citrate dihydrate	$Na_3C_6H_5O_7 \cdot 2H_2O$	Sigma-Aldrich	Retarder of the setting reaction
Polycaprolactone (PCL)	$(C_6H_{10}O_2)_n$	3D4Makers	Polymeric matrix for the composite and filament production

Table 1: Reagents used for the synthesis of zinc-doped β-tricalcium phosphate (β-TCP), for the preparation of brushite cement, and for the fabrication of the brushite-PCL composite intended for 3D printing.

2.2. Synthesis of zinc-doped β-tricalcium phosphate

The first phase of the experimental work concerned the synthesis of zinc-doped β-tricalcium phosphate (β-TCP), subsequently used as a precursor for the preparation of brushite cement.

Zinc-doped β-tricalcium phosphate (β-TCP:Zn) was synthesized by a solid-state reaction, starting from a mixture of:

- Dibasic calcium phosphate ($CaHPO_4$)
- Calcium carbonate ($CaCO_3$)
- Zinc oxide (ZnO).

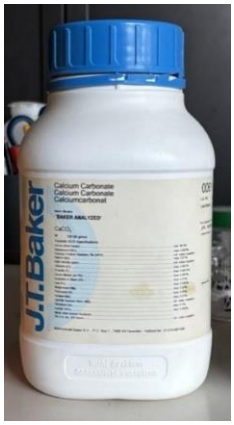

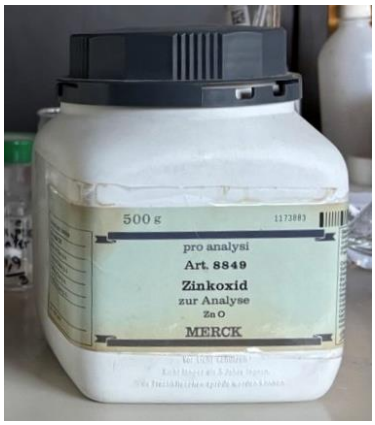

This approach is commonly used for the preparation of doped calcium phosphates, as it allows materials with controlled composition and good homogeneity of the crystalline phase to be obtained.

The quantities of the reagents were determined based on the stoichiometry of the synthesis reaction:

$$2CaHPO_4 + (1 - x)\,CaCO_3 + xZnO = Ca_{(3-x)}\,Zn_x\,(PO_4)_2 + H_2O + (1 - x)CO_2$$

In this reaction, the parameter x represents the molar fraction of Zn^{2+} ions introduced into the starting mixture, which partially substitute Ca^{2+} ions within the crystal lattice of β-tricalcium phosphate. By varying the value of x, it is therefore possible to modulate the degree of doping of the material and obtain formulations with different zinc contents, as shown in Table 2.

ZnO %	ZnO Moles (X)	Powder	
0	0	$Ca_3(PO_4)_2$	→ β-TCP
1	0.03	$Ca_{2.97}Zn_{0.03}(PO_4)_2$	Znβ-TCP
3	0.09	$Ca_{2.91}Zn_{0.09}(PO_4)_2$	
6	0.18	$Ca_{2.82}Zn_{0.18}(PO_4)_2$	
9	0.27	$Ca_{2.73}Zn_{0.27}(PO_4)_2$	
12	0.36	$Ca_{2.64}Zn_{0.36}(PO_4)_2$	
18	0.54	$Ca_{2.46}Zn_{0.54}(PO_4)_2$	
24	0.72	$Ca_{2.28}Zn_{0.72}(PO_4)_2$	

Table 2: The ZnO content in the starting mixture is expressed both in moles and in the corresponding weight percentages (%ZnO). The %ZnO value represents the ratio between the moles of ZnO added to the powder mixture and the moles of Ca^{2+} ions present in the β-TCP lattice. The parameter x indicates the number of moles of zinc introduced into the powder mixture.

In the present work, three different nominal zinc doping percentages were considered, equal to 2%, 5%, and 10%, in order to evaluate the influence of the amount of Zn^{2+} on the properties of the material obtained. Since the theoretical amount of reagents required for the production of one mole of material was excessive compared with the experimental needs, the reagents were weighed by considering one tenth of the theoretical quantities calculated.

The masses actually used for the preparation of the different formulations are reported in Table 3, which summarizes the amounts of $CaHPO_4$, $CaCO_3$, and ZnO used for each doping level. As shown in the table, as the percentage of zinc doping increases, the amount of calcium carbonate required for the synthesis decreases, whereas the amount of zinc oxide used in the starting mixture increases.

Zn doping (%)	x	$CaHPO_4$ (g/mol)		$CaCO_3$ (g/mol)		ZnO (g/mol)	
		Teoric	Used	Teoric	Used	Teoric	Used
2	0,06	272,1	27,2	94,1	9,4	4,88	0,486
5	0,15	272,1	27,2	85,1	8,5	12,21	1,215
10	0,30	272,1	27,2	70,1	7,01	24,41	2,443

Table 3: Amounts of reagents used for the synthesis of β-tricalcium phosphate (β-TCP) doped with Zn^{2+} at the different doping percentages. The reported values correspond to one tenth of the theoretical quantities calculated per mole of product on the basis of the stoichiometric reaction.

Weighing of the reagents for the synthesis of 2% Zn^{2+}-doped β-TCP

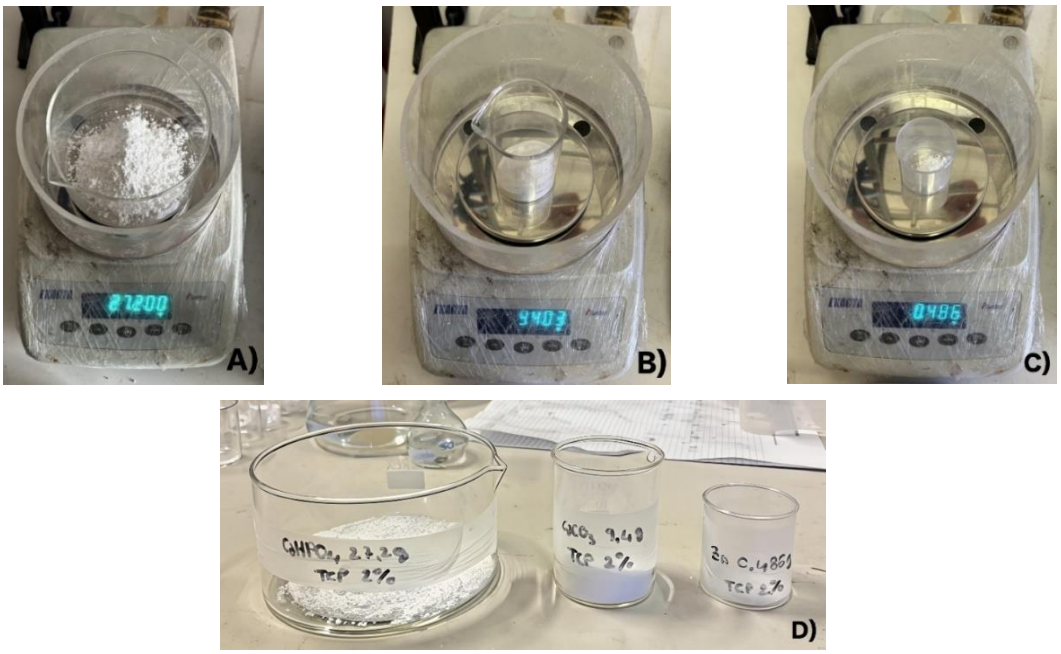

Figure 15: Preliminary steps in the preparation of the reagent mixture used for the synthesis of β-tricalcium phosphate (β-TCP) doped with Zn^{2+} ions, with a nominal doping percentage of 2%. The images show the weighing of the individual reagents on an analytical balance, specifically: (A) weighing of dibasic calcium phosphate ($CaHPO_4$); (B) weighing of calcium carbonate ($CaCO_3$); (C) weighing of zinc oxide (ZnO), used as a source of Zn^{2+} ions for doping; (D) the three weighed reagents placed in their respective containers, ready to be subsequently ground in a mortar and mixed together.

Weighing of the reagents for the synthesis of 5% Zn^{2+}-doped β-TCP

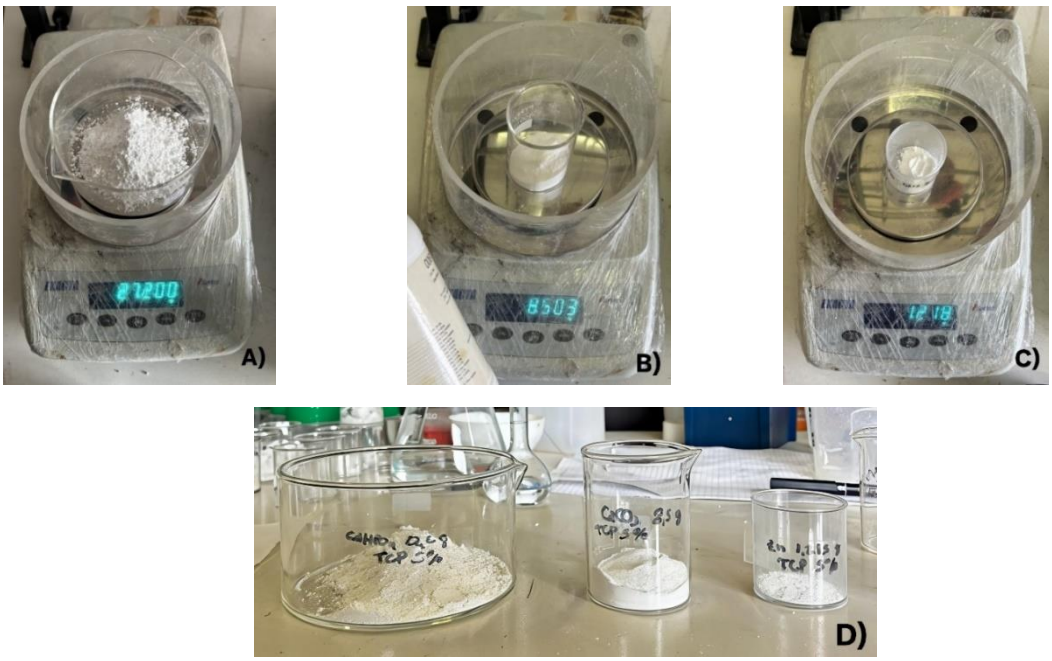

Figure 16: Preliminary steps in the preparation of the reagent mixture used for the synthesis of β-tricalcium phosphate (β-TCP) doped with Zn^{2+} ions, with a nominal doping percentage of 5%. The images show the weighing of the individual reagents on an analytical balance, specifically: (A) weighing of dibasic calcium phosphate ($CaHPO_4$); (B) weighing of calcium carbonate ($CaCO_3$); (C) weighing of zinc oxide (ZnO), used as a source of Zn^{2+} ions for doping; (D) the three weighed reagents placed in their respective containers, ready to be subsequently ground in a mortar and mixed together.

Weighing of the reagents for the synthesis of 10% Zn^{2+}-doped β-TCP

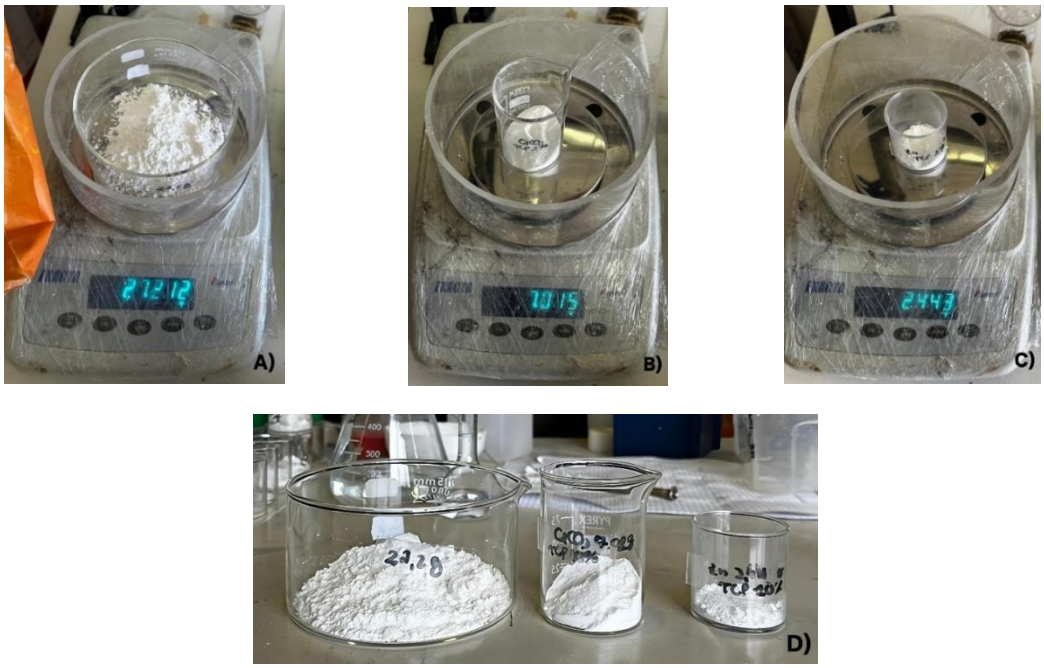

Figure 17: Preliminary steps in the preparation of the reagent mixture used for the synthesis of β-tricalcium phosphate (β-TCP) doped with Zn^{2+} ions, with a nominal doping percentage of 10%. The images show the weighing of the individual reagents on an analytical balance, specifically: (A) weighing of dibasic calcium phosphate ($CaHPO_4$); (B) weighing of calcium carbonate ($CaCO_3$); (C) weighing of zinc oxide (ZnO), used as a source of Zn^{2+} ions for doping; (D) the three weighed reagents placed in their respective containers, ready to be subsequently ground in a mortar and mixed together.

The powders of the individual reagents were initially ground and manually homogenized in a mortar, in order to reduce particle size and promote a uniform distribution of the components. The reagents were then carefully mixed until a homogeneous mixture was obtained.

For each doping percentage, the resulting mixture was placed in a mold and subjected to mechanical pressing, in order to obtain compact pellets suitable for facilitating the subsequent thermal treatment.

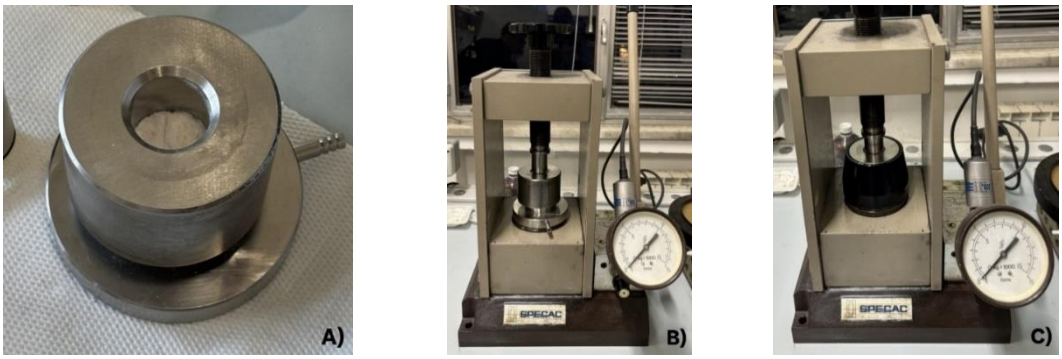

Figure 18: Steps for pellet preparation: (A) material placed inside the mold; (B) mold placed inside the press; (C) counter-mold inside the press for removing the pellets.

The pellets obtained were then placed in refractory crucibles and subjected to thermal treatment in a furnace for 12 hours, at a temperature close to 1000 °C, in order to promote the formation of the zinc-doped β-TCP crystalline phase.

At the end of the thermal treatment, the sintered samples were cooled to room temperature and subsequently reduced again to powder by mechanical grinding, thus obtaining zinc-doped β-TCP powder intended for the subsequent preparation of brushite cement.

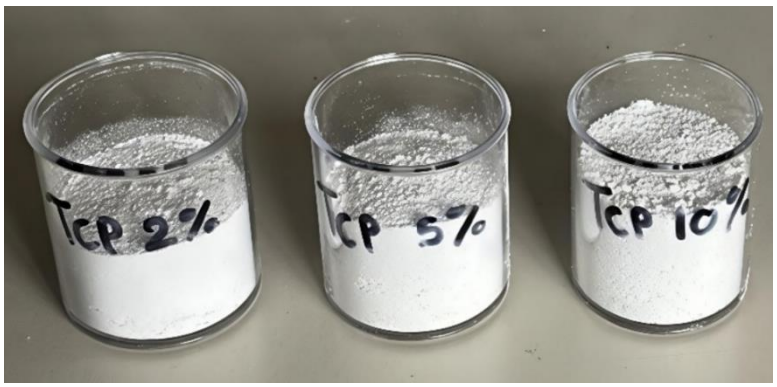

The entire procedure was repeated for each of the three planned formulations, corresponding to nominal zinc doping percentages of 2%, 5%, and 10%.

2.3. Preparation of brushite cement obtained from zinc-doped β-TCP

The second part of the experimental work concerned the preparation of zinc-doped brushite-based bone cements, obtained from:

- β-tricalcium phosphate doped with Zn^{2+} ions synthesized in the previous phase;
- Monocalcium phosphate monohydrate (MCPM);
- Distilled water;
- Trisodium citrate dihydrate.

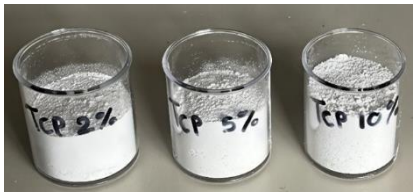

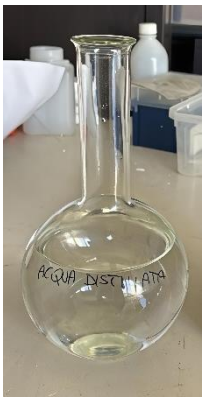
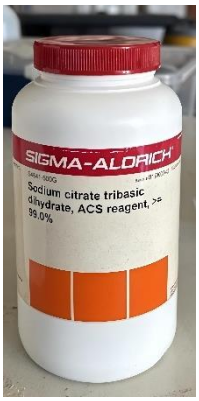

Before preparing the cement pastes, the liquid phase was prepared, consisting of distilled water containing trisodium citrate dihydrate. Citrate was used as a retarder of the setting reaction, since brushite formation occurs rapidly after contact between the reactive powders and water. Its addition to the liquid phase therefore made it possible to increase the working time of the cement paste, facilitating both the mixing of the reagents and the subsequent insertion of the material into the cylindrical molds.

For the preparation of the aqueous trisodium citrate dihydrate solution, the following parameters were considered:

- Molecular weight of citrate: 294,10 g/mol;
- Desired molarity of the solution: 1 M;
- Solution volume: 0,1 L.

Therefore, to calculate the amount of trisodium citrate dihydrate to be dissolved in 100 mL in order to obtain a 1 M solution, the following formula was applied:

$$m = M \times V \times PM = 1 \times 0{,}1 \times 294{,}10 = 29{,}41g$$

Thus, 29,41 g of trisodium citrate dihydrate were weighed, then transferred into a volumetric flask and dissolved in distilled water. Water was progressively added until the final volume mark of 100 mL was reached. Once the citrate had completely dissolved, the resulting solution was used as the retarding liquid phase for the preparation of the brushite cements.

At this point, the quantities of the reagents were determined based on the stoichiometry of the synthesis reaction:

$$Ca_3(PO_4)_2 + Ca(H_2PO_4)_2 \cdot H_2O + 7H_2O \rightarrow 4CaHPO_4 \cdot 2H_2O$$

Starting from the stoichiometry of the synthesis reaction, the quantities of reagents required for the preparation of the zinc-doped brushite cements were determined. The calculation was performed separately for each component of the mixture; therefore, the following were evaluated:

- the amount of Zn^{2+}-doped β-tricalcium phosphate;
- the amount of monocalcium phosphate monohydrate (MCPM);
- the amount of liquid phase, consisting of distilled water supplemented with trisodium citrate dihydrate.

Since the theoretical quantities calculated for the production of one mole of material were greater than the experimental requirements, the values obtained were initially divided by 10. Subsequently, in order to facilitate manual mixing of the reagents and improve the workability of the cement paste, each quantity was further divided into four aliquots, corresponding to four separate preparations for each doping percentage.

Amount of zinc-doped β-tricalcium phosphate

The amount of β-TCP to be used was calculated by taking into account the different theoretical molar mass of the material as a function of the nominal Zn^{2+} doping percentage. Indeed, the partial substitution of Ca^{2+} ions with Zn^{2+} ions within the β-TCP crystal lattice results in a slight variation in molecular weight compared with undoped β-TCP.

The theoretical molecular weight of pure β-TCP, $Ca_3(PO_4)_2$, is approximately 310 g/mol.

$$Ca_3(PO_4)_2 = (40 \cdot 3) + (31 \cdot 2) + (16 \cdot 8) = 120 + 62 + 128 = 310\ g/mol$$

However, in the doped formulations, part of the calcium ions is replaced by zinc ions; therefore, the molecular weight was recalculated for each doping percentage.

- 2% Zn^{2+}-doped β-TCP

  Calcium contribution = MW · number of atoms · % = 40 · 3 · 0,98 = 117,5 g/mol
  Zinc contribution = MW · number of atoms · % = 65,4 · 3 · 0,02 = 3,9 g/mol

  $$117,5 + 3,9 = 121,4\ g/mol$$

  $$PM\ \beta\text{-}TCP{:}Zn\ 2\% = 121,4 + (31 \cdot 2) + (16 \cdot 8) = 121,4 + 62 + 128 = 311,4\ g/mol$$

  Since the theoretical calculated amount of 311,4 g/mol for the production of one mole of material was greater than the experimental requirements, the value obtained was divided by 10 and subsequently divided by 4, in order to split the amount into four preparations and facilitate mixing.

  $$\beta - TCP{:}\,Zn\ 2\% = \frac{\left(\frac{311,4}{10}\right)}{4} = 7,79\ g$$

  Therefore, for each preparation of 2% brushite-Zn^{2+}, approximately 7,79 g of β-TCP:Zn 2% were used, corresponding to approximately 31,16 g for the four preparations.

- 5% Zn^{2+}-doped β-TCP

  Calcium contribution = MW · number of atoms · % = 40 · 3 · 0,95 = 114 g/mol
  Zinc contribution = MW · number of atoms · % = 65,4 · 3 · 0,05 = 9,8 g/mol

  $$114 + 9{,}8 = 123{,}8 \text{ g/mol}$$

  $$PM\ \beta\text{-}TCP{:}Zn\ 5\% = 123{,}8 + (31 \cdot 2) + (16 \cdot 8) = 123{,}8 + 62 + 128 = 313{,}8 \text{ g/mol}$$

  Since the theoretical calculated amount of 313,8 g/mol for the production of one mole of material was greater than the experimental requirements, the value obtained was divided by 10 and subsequently divided by 4, in order to split the amount into four preparations and facilitate mixing.

  $$\beta - TCP{:}Zn\ 5\% = \frac{\left(\frac{313{,}8}{10}\right)}{4} = 7{,}85\ g$$

  Therefore, for each preparation of 5% brushite-Zn^{2+}, approximately 7,85 g of β-TCP:Zn 5% were used, corresponding to approximately 31,38 g for the four preparations.

- 10% Zn^{2+}-doped β-TCP

  Calcium contribution = MW · number of atoms · % = 40 · 3 · 0,90 = 108 g/mol
  Zinc contribution = MW · number of atoms · % = 65,4 · 3 · 0,10 = 19,6 g/mol

  $$108 + 19{,}6 = 127{,}6 \text{ g/mol}$$

  $$PM\ \beta\text{-}TCP{:}Zn\ 10\% = 127{,}6 + (31 \cdot 2) + (16 \cdot 8) = 127{,}6 + 62 + 128 = 317{,}6 \text{ g/mol}$$

  Since the theoretical calculated amount of 317,6 g/mol for the production of one mole of material was greater than the experimental requirements, the value obtained was divided by 10 and subsequently divided by 4, in order to split the amount into four preparations and facilitate mixing.

  $$\beta - TCP{:}Zn\ 10\% = \frac{\left(\frac{317{,}6}{10}\right)}{4} = 7{,}94\ g$$

  Therefore, for each preparation of 10% brushite-Zn^{2+}, approximately 7,94 g of β-TCP:Zn 10% were used, corresponding to approximately 31,76 g for the four preparations.

Amount of monocalcium phosphate monohydrate (MCPM)

The amount of monocalcium phosphate monohydrate, $Ca(H_2PO_4)_2 \cdot H_2O$, was calculated based on the stoichiometry of the brushite formation reaction. Unlike β-TCP, the amount of MCPM does not vary as a function of the zinc doping percentage, since this reagent does not contain Zn^{2+} and is used in the same quantity for all formulations.

Considering a molecular weight of MCPM equal to 252 g/mol, in this case as well the theoretical amount was initially divided by 10 and subsequently divided into four aliquots.

$$Ca(H_2PO_4)_2 \cdot H_2O = 40 + (1 \cdot 6) + (31 \cdot 2) + (16 \cdot 9) = 40 + 6 + 62 + 144 = 252\ g/mol$$

$$MCPM = \frac{\left(\frac{252}{10}\right)}{4} = 6{,}3\ g$$

Therefore, for each preparation of doped brushite, approximately 6,3 g of MCPM were used, corresponding to approximately 25,2 g for the four preparations.

Amount of distilled water-citrate liquid phase

The amount of liquid phase to be added to the powders was determined by considering an indicative solid-to-liquid ratio of 3:1. Therefore, for each formulation, the total mass of the powders, consisting of β-TCP:Zn and MCPM, was divided by three, obtaining the amount of distilled water-citrate solution to be used for the preparation of the cement paste.

- For the 2% brushite-Zn^{2+} formulation, the total amount of liquid phase was calculated by dividing by 3 the total mass of the powders, consisting of β-TCP:Zn 2% and MCPM, according to a powder/liquid ratio of 3:1. Since the mixture was subsequently divided into four separate preparations, the total amount of liquid phase was also further divided by 4.

$$H2O + citrato = \frac{\left[\frac{(\beta - TCP{:}\ Zn\ 2\% \ +\ MCPM)}{3}\right]}{4} = \frac{\left[\frac{(31{,}16 + 25{,}2\ )}{3}\right]}{4} = \ 4{,}69\ g$$

  Therefore, for each preparation of 2% brushite-Zn^{2+}, approximately 4,69 g of distilled water-citrate solution were used, corresponding to approximately 18,78 g for the four preparations.

- For the 5% brushite-Zn^{2+} formulation, the total amount of liquid phase was calculated by dividing by 3 the total mass of the powders, consisting of β-TCP:Zn 5% and MCPM, according to a powder/liquid ratio of 3:1. Since the mixture was subsequently divided into four separate preparations, the total amount of liquid phase was also further divided by 4.

$$H2O + \ citrato = \frac{\left[\frac{(\beta - TCP{:}\, Zn\ 5\% \ + \ MCPM)}{3}\right]}{4} = \frac{\left[\frac{(31{,}38 + 25{,}2\ )}{3}\right]}{4} = \ 4{,}72\ g$$

  Therefore, for each preparation of 5% brushite-Zn^{2+}, approximately 4,72 g of distilled water-citrate solution were used, corresponding to approximately 18,86 g for the four preparations.

- For the 10% brushite-Zn^{2+} formulation, the total amount of liquid phase was calculated by dividing by 3 the total mass of the powders, consisting of β-TCP:Zn 10% and MCPM, according to a powder/liquid ratio of 3:1. Since the mixture was subsequently divided into four separate preparations, the total amount of liquid phase was also further divided by 4.

$$H2O + \ citrato = \frac{\left[\frac{(\beta - TCP{:}\, Zn\ 10\% \ + \ MCPM)}{3}\right]}{4} = \frac{\left[\frac{(31{,}76 + 25{,}2\ )}{3}\right]}{4} = \ 4{,}75\ g$$

  Therefore, for each preparation of 10% brushite-Zn^{2+}, approximately 4,75 g of distilled water-citrate solution were used, corresponding to approximately 18,99 g for the four preparations.

Based on the calculations described above, the overall quantities and those actually used for each single preparation are reported in Table 4.

Formulation	β-TCP:Zn			MCPM			Distilled water-citrate solution	
	Theoretical MW of β-TCP:Zn (g/mol)	Total amount used after division ×10 (g)	Amount per single preparation (g)	Theoretical MW of MCPM (g/mol)	Total amount used after division ×10 (g)	Amount per single preparation (g)	Total amount used based on powder mass (g)	Amount per single preparation (g)
Brushite-Zn^{2+} 2%	311,48	31,16	7,79	252	25,2	6,3	18,78	4,69
Brushite-Zn^{2+} 5%	313,81	31,38	7,85				18,86	4,72
Brushite-Zn^{2+} 10%	317,62	31,76	7,94				18,99	4,75

Table 4: Amounts of reagents used for each preparation of brushite cement doped with Zn^{2+}. The reported values derive from the stoichiometric calculation of the brushite formation reaction, from the reduction to one tenth of the theoretical quantities, and from the subsequent division into four aliquots, in order to facilitate manual mixing of the cement paste. The amount of liquid phase was calculated by maintaining an indicative powder/liquid ratio of 3:1.

Once the quantities of reagents had been defined, the experimental preparation of the cement pastes was carried out. For each formulation, the required amounts of β-TCP:Zn and MCPM were weighed into small plastic beakers using an analytical balance. The powders were then combined and manually mixed for a few minutes, in order to obtain the most homogeneous possible distribution of the two solid reagents.

Subsequently, the predetermined amount of distilled water-citrate solution was added to the powder mixture. After the addition of the liquid phase, the system was vigorously mixed for approximately 30 seconds, until a homogeneous cement paste was obtained. Following contact between the solid phase and the liquid phase, the mixture showed a progressive increase in consistency over a few minutes, compatible with the onset of the brushite setting reaction.

Before complete hardening, the cement paste was transferred into previously modified sterile 5 mL syringes, used as cylindrical molds for shaping the doped brushite samples.

The syringes were cut at the apical end using a small circular saw, in order to obtain an open cylinder with a uniform diameter. In addition, the rubber gasket was removed from the plunger, and the corresponding locking system was eliminated, in order to allow more uniform compaction of the material inside the mold.

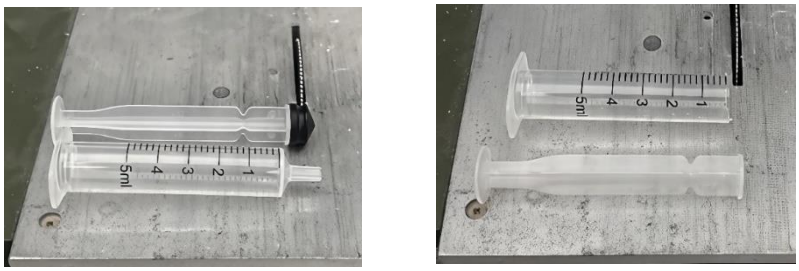

After filling, the end of the syringe was closed and the plunger was manually pressed to compact the cement paste and reduce the presence of macroscopic voids. The samples were then left to harden inside the syringes for at least four days, in order to allow completion of the setting reaction and obtain cylinders sufficiently stable for subsequent handling. At the end of hardening, the samples showed a cylindrical geometry with approximate dimensions of 12,5 mm in diameter and 25 mm in height.

Preparation of 2% Zn^{2+}-doped brushite

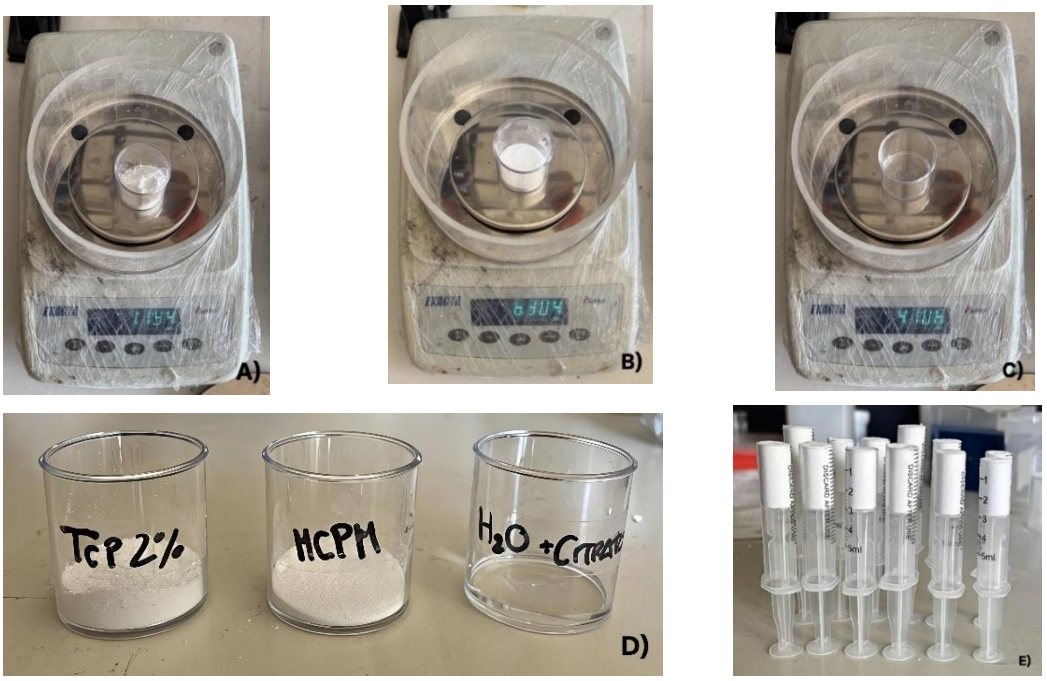

Figure 19: Preparation steps of 2% Zn^{2+}-doped brushite cement. The images show the main operations performed for reagent weighing, preparation of the cement mixture, and shaping of the cylindrical samples. In particular: (A) weighing of zinc-doped β-tricalcium phosphate (β-TCP:Zn 2%), used in an amount of approximately 7,79 g for each single preparation; (B) weighing of monocalcium phosphate monohydrate (MCPM), used in an amount of 6,30 g; (C) weighing of the distilled water-citrate solution, used as the liquid phase and as a retarder of the setting reaction, in an amount of approximately 4,69 g; (D) weighed reagents placed in their respective containers before mixing; (E) cylindrical samples obtained by inserting the cement paste into previously modified sterile 5 mL syringes.

Preparation of 5% Zn^{2+}-doped brushite

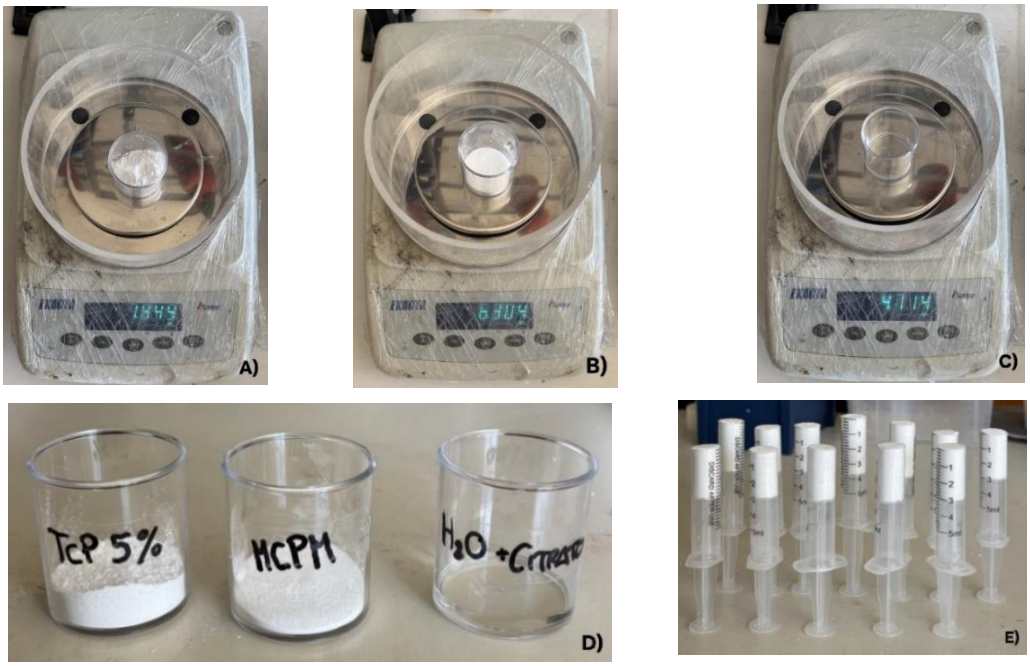

Figure 20: Preparation steps of 5% Zn^{2+}-doped brushite cement. The images show the main operations performed for reagent weighing, preparation of the cement mixture, and shaping of the cylindrical samples. In particular: (A) weighing of zinc-doped β-tricalcium phosphate (β-TCP:Zn 5%), used in an amount of approximately 7,85 g for each single preparation; (B) weighing of monocalcium phosphate monohydrate (MCPM), used in an amount of 6,30 g; (C) weighing of the distilled water-citrate solution, used as the liquid phase and as a retarder of the setting reaction, in an amount of approximately 4,72 g; (D) weighed reagents placed in their respective containers before mixing; (E) cylindrical samples obtained by inserting the cement paste into previously modified sterile 5 mL syringes.

Preparation of 10% Zn^{2+}-doped brushite

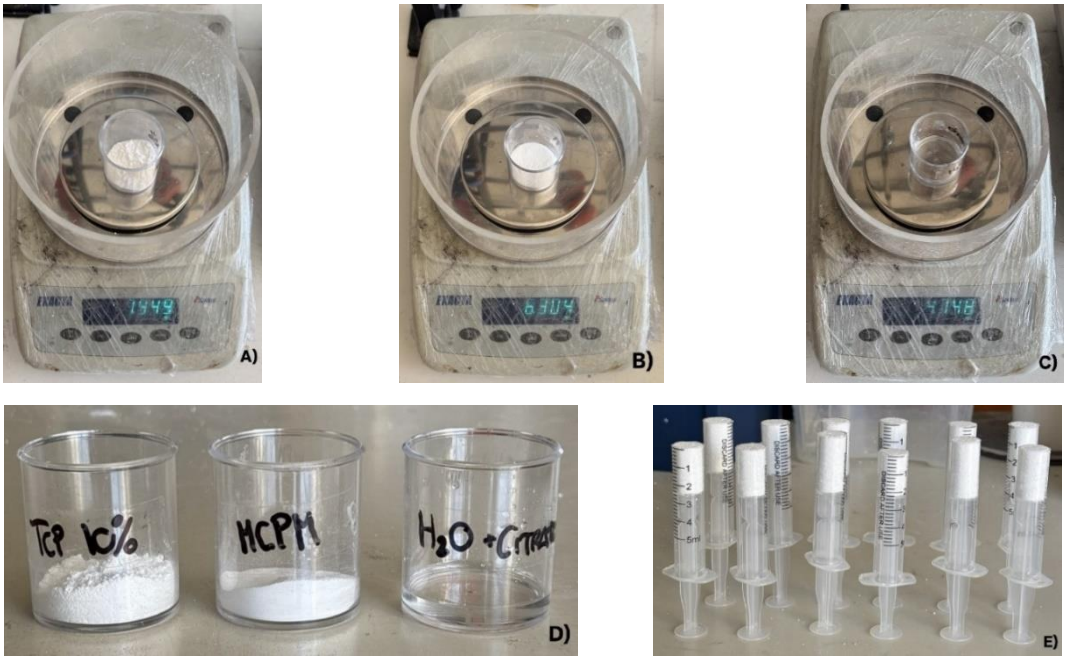

Figure 21: Preparation steps of 10% Zn^{2+}-doped brushite cement. The images show the main operations performed for reagent weighing, preparation of the cement mixture, and shaping of the cylindrical samples. In particular: (A) weighing of zinc-doped β-tricalcium phosphate (β-TCP:Zn 10%), used in an amount of approximately 7,94 g for each single preparation; (B) weighing of monocalcium phosphate monohydrate (MCPM), used in an amount of 6,30 g; (C) weighing of the distilled water-citrate solution, used as the liquid phase and as a retarder of the setting reaction, in an amount of approximately 4,75 g; (D) weighed reagents placed in their respective containers before mixing; (E) cylindrical samples obtained by inserting the cement paste into previously modified sterile 5 mL syringes.

2.4. Rationale for zinc doping

The introduction of Zn^{2+} ions into the structure of the material was designed with the aim of improving the biological properties of conventional calcium phosphate-based cements. Although these materials are characterized by high biocompatibility, bioactivity, and osteoconductivity, they generally show limited intrinsic antibacterial activity. This aspect represents a relevant critical issue in regenerative applications, since bacterial contamination of the surgical site may promote the onset of post-operative infections and compromise the healing process and integration of the biomaterial.

Zinc is an essential trace element involved in numerous biological processes, including the regulation of enzymatic activity, cell proliferation, protein synthesis, and bone tissue metabolism. In particular, Zn^{2+} ions have been described as elements capable of positively influencing osteoblast activity, promoting cell proliferation and differentiation, and contributing to bone matrix mineralization processes. For this reason, the integration of zinc into calcium phosphate-based biomaterials represents a promising strategy to enhance the osteogenic response of the material.

In addition to its possible osteogenic effect, zinc also shows potential antibacterial properties. The incorporation of Zn^{2+} ions into the structure of calcium phosphates may contribute to limiting bacterial adhesion and proliferation on the surface of the biomaterial, reducing the risk of microbial colonization in the phases following implantation. This aspect is particularly important in the development of materials intended for bone regeneration, where the presence of local infections may compromise clot stability, cellular colonization, and the formation of new bone tissue.

Ionic doping may also modify some chemical and physical properties of the material, such as crystallinity, solubility, and degradation rate. Since brushite is a relatively soluble and bioresorbable calcium phosphate phase, the partial substitution of Ca^{2+} ions with Zn^{2+} ions could influence the behavior of the cement during degradation and ion release into the surrounding microenvironment. These modifications may play a relevant role in the interaction between the biomaterial and the cells of the host tissue.

In the present study, three nominal zinc doping concentrations were selected, equal to 2%, 5%, and 10%, with the aim of evaluating the effect of Zn^{2+} content on the properties of the material. The choice of multiple doping percentages makes it possible

to compare formulations with different ionic contents and to investigate the possible influence of zinc on the chemical-structural and mechanical behavior of the biomaterial. In particular, the formulations obtained were subjected to preliminary mechanical compression tests, characterization analyses by FT-IR spectroscopy and X-ray diffraction, and were subsequently used for the preparation of doped brushite-PCL composites. From these composites, rectangular specimens intended for flexural mechanical testing and discs intended for preliminary biological evaluations were produced by 3D printing. The latter, although included in the overall experimental project, will be mainly investigated within the parallel thesis dedicated to the biological evaluation of the developed materials.

2.5 Preparation of pure brushite cement as a control sample

In parallel with the preparation of zinc-doped brushite cements, a pure brushite cement was also produced and used as a control sample. This undoped formulation was prepared with the aim of obtaining a reference material to be compared with the 2%, 5%, and 10% brushite-Zn^{2+} formulations in the subsequent preliminary mechanical compression tests and chemical-structural characterization analyses by FT-IR spectroscopy and X-ray diffraction.

The preparation of pure brushite was carried out using pure β-tricalcium phosphate (β-TCP), monocalcium phosphate monohydrate (MCPM), and the same distilled water-citrate solution previously prepared and used for the doped formulations.

Unlike the zinc-doped β-TCP, the pure β-TCP used in this phase was not synthesized during the present experimental work, but was used directly as a starting reagent for the preparation of the undoped brushite cement.

The formation reaction of pure brushite is analogous to that described for the doped formulations and can be represented by the following equation:

$$Ca_3(PO_4)_2 + Ca(H_2PO_4)_2 \cdot H_2O + 7H_2O \rightarrow 4CaHPO_4 \cdot 2H_2O$$

The quantities of the reagents were determined based on the stoichiometry of the reaction:

- For pure β-TCP, with the chemical formula $Ca_3(PO_4)_2$, a theoretical molar mass of approximately 310 g/mol was considered. As performed for the doped formulations, this value was initially divided by 10 and subsequently divided into four separate preparations:

$$Ca_3(PO_4)_2 = (40 \cdot 3) + (31 \cdot 2) + (16 \cdot 8) = 120 + 62 + 128 = 310 \text{ g/mol}$$

$$\beta - TCP = \frac{\left(\frac{310,0}{10}\right)}{4} = 7,75\ g$$

  Therefore, for each preparation of pure brushite, approximately 7,75 g of β-TCP were used, corresponding to approximately 31,0 g for the four preparations.

- For monocalcium phosphate monohydrate (MCPM), a molar mass of 252 g/mol was considered. In this case as well, the theoretical amount was divided by 10 and subsequently divided into four aliquots:

  $Ca(H_2PO_4)_2 \cdot H_2O = 40 + (1 \cdot 6) + (31 \cdot 2) + (16 \cdot 9) = 40 + 6 + 62 + 144 = 252\ g/mol$

  $$MCPM = \frac{\left(\frac{252}{10}\right)}{4} = 6{,}3\ g$$

  Therefore, for each preparation of pure brushite, approximately 6,3 g of MCPM were used, corresponding to approximately 25,2 g for the four preparations.

- The liquid phase, consisting of the distilled water-citrate solution, was calculated by dividing by 3 the total mass of the powders, consisting of β-TCP and MCPM, according to a powder/liquid ratio of 3:1. Since the mixture was subsequently divided into four separate preparations, the total amount of liquid phase was also divided by 4.

  $$H2O + \ citrato = \frac{\left[\frac{(\beta - TCP + MCPM)}{3}\right]}{4} = \frac{\left[\frac{(31{,}0 + 25{,}2\ )}{3}\right]}{4} = \ 4{,}69\ g$$

  Therefore, for each preparation of pure brushite, approximately 4,69 g of distilled water-citrate solution were used, corresponding to approximately 18,78 g for the four preparations.

The quantities of the reagents used for the preparation of pure brushite cement are reported in Table 5.

	β-TCP			**MCPM**			**Distilled water-citrate solution**	
	Theoretical MW of β-TCP (g/mol)	**Total amount used after division ×10 (g)**	**Amount per single preparation (g)**	**Theoretical MW of MCPM (g/mol)**	**Total amount used after division ×10 (g)**	**Amount per single preparation (g)**	**Total amount used based on powder mass (g)**	**Amount per single preparation (g)**
Pure brushite	310,0	31,0	7,75	252	25,2	6,3	18,78	4,69

Table 5: Amounts of reagents used for the preparation of pure brushite cement. The reported values derive from the stoichiometric calculation of the brushite formation reaction, from the reduction to one tenth of the theoretical quantities, and from the subsequent division into four aliquots, in order to facilitate manual mixing of the cement paste. The amount of liquid phase was calculated by maintaining an indicative powder/liquid ratio of 3:1.

Once the quantities of the reagents had been defined, pure β-TCP and MCPM were weighed into small plastic beakers using an analytical balance. The powders were then combined and manually mixed for a few minutes, in order to obtain a homogeneous distribution of the solid reagents. Subsequently, the distilled water-citrate solution was added, and the mixture was vigorously mixed until a homogeneous cement paste was obtained.

The paste thus obtained was transferred into previously modified sterile 5 mL syringes, used as cylindrical molds, according to the same procedure described for the doped formulations. After filling, the syringes were closed and the plunger was manually pressed to compact the material and reduce the presence of macroscopic voids.

The samples were left to harden inside the syringes for at least four days, in order to allow completion of the setting reaction and obtain pure brushite cylinders sufficiently stable for subsequent handling. The samples thus obtained were used as a reference for comparison in the preliminary mechanical compression tests and for characterization analyses by FT-IR and XRD.

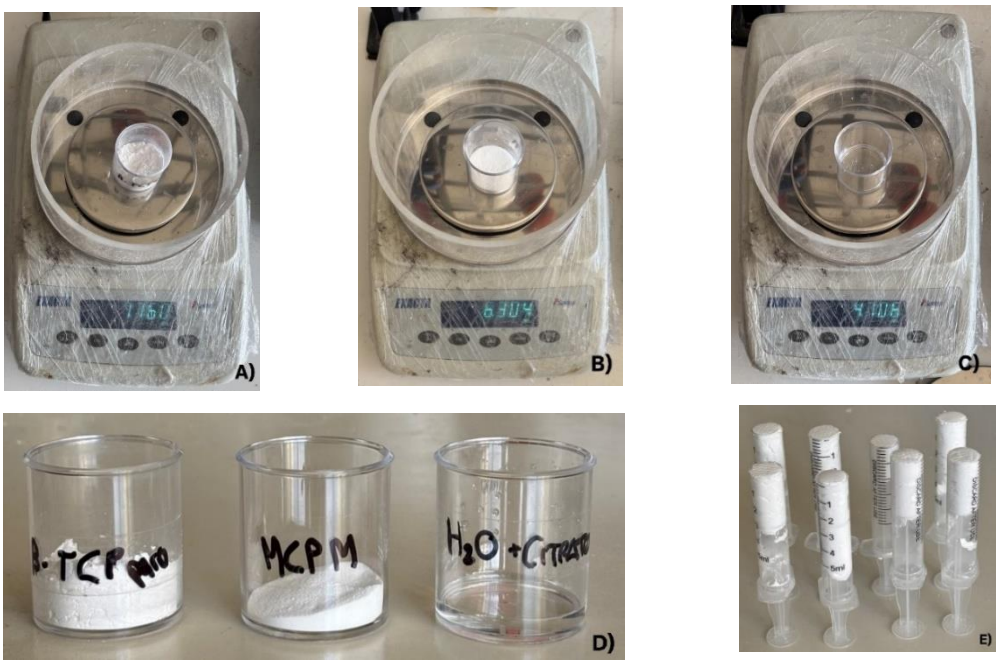

Figure 22: Preparation steps of pure brushite cement. The images show the main operations performed for reagent weighing, preparation of the cement mixture, and shaping of the cylindrical samples. In particular: (A) weighing of β-tricalcium phosphate, used in an amount of approximately 7,75 g for each single preparation; (B) weighing of monocalcium phosphate monohydrate (MCPM), used in an amount of 6,30 g; (C) weighing of the distilled water-citrate solution, used as the liquid phase and as a retarder of the setting reaction, in an amount of approximately 4,69 g; (D) weighed reagents placed in their respective containers before mixing; (E) cylindrical samples obtained by inserting the cement paste into previously modified sterile 5 mL syringes.

2.6 Sample preparation and preliminary mechanical compression testing of brushite cements

After completion of the setting reaction, the Zn^{2+}-doped brushite samples and the pure brushite samples were removed from the sterile 5 mL syringes previously used as cylindrical molds. The cylinders obtained were then macroscopically observed and selected based on shape regularity and dimensional similarity, in order to reduce geometrical variability during the mechanical tests.

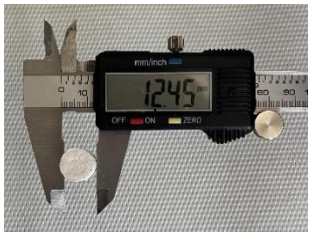

For each formulation, five representative cylinders were selected, characterized by a diameter of approximately 12,5 mm, corresponding to the internal diameter of the syringes used for molding, and an indicative height ranging between 25 and 26 mm.

The formulations considered included pure brushite, used as the control sample, and the three zinc-doped brushite formulations, namely brushite-Zn^{2+} 2%, brushite-Zn^{2+} 5%, and brushite-Zn^{2+} 10%.

The preliminary mechanical compression tests were performed using a Zwick/Roell universal testing machine, with testXpert III software for data acquisition and processing. Each cylinder was positioned vertically between two parallel plates: a fixed lower plate and a movable upper plate. During the test, the upper plate was progressively brought into contact with the upper surface of the sample, allowing axial application of the compressive load and the most uniform possible distribution of the force over the cross-section of the cylinder.

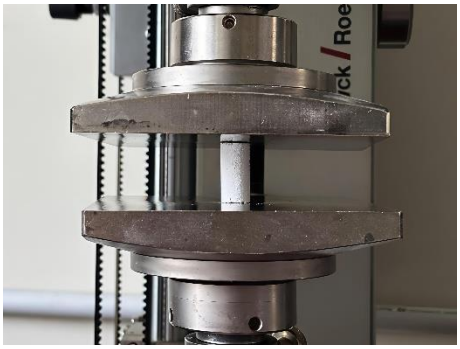

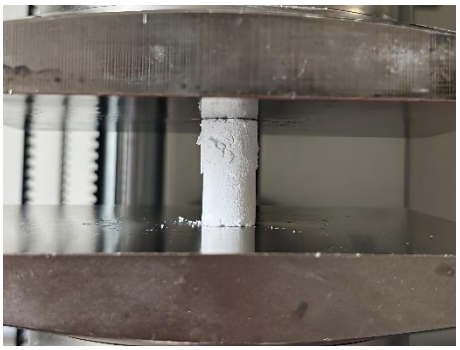

For each sample, the mechanical response of the material during compression was recorded, obtaining stress-strain curves, in which percentage strain was plotted on the x-axis and stress on the y-axis. The acquired data made it possible to obtain the main mechanical parameters describing the behavior of the cements, including the compressive elastic modulus, maximum stress, and the corresponding strain.

The tests were conducted with the aim of obtaining a preliminary evaluation of the mechanical properties of the brushite cements and comparing the behavior of the pure formulation with that of the formulations doped with different nominal percentages of Zn^{2+}. The detailed analysis of the results obtained and the comparison among the different formulations will be discussed in the chapter dedicated to the results and discussion.

At the end of the mechanical tests, the doped brushite and pure brushite samples were subsequently subjected to mechanical grinding until fine powders were obtained. This step was necessary both to allow the subsequent chemical-structural characterization analyses by FT-IR spectroscopy and X-ray diffraction, and to make the doped brushite usable in the subsequent preparation steps of the brushite-PCL composites by melt blending.

2.7 Characterization of the materials

After the preliminary mechanical compression tests, the cylindrical samples of pure brushite and Zn^{2+}-doped brushite were further processed for use in the subsequent chemical-structural characterization steps. In particular, both the cylinders subjected to mechanical testing and the remaining unused samples were fragmented and subsequently ground until a fine and as homogeneous as possible powder was obtained.

This powdering step was necessary for two main reasons. On the one hand, it allowed the samples to be prepared in a form suitable for analysis by X-ray diffraction and FT-IR spectroscopy, techniques that require a uniform distribution of the material to be analyzed. On the other hand, it made it possible to obtain a powder that was easier to handle and could subsequently be used for the preparation of PCL- and brushite-based polymeric composites.

For each formulation, namely pure brushite, brushite-Zn^{2+} 2%, brushite-Zn^{2+} 5%, and brushite-Zn^{2+} 10%, the total amount of powder obtained was divided into four aliquots. One portion was intended for chemical-structural characterization analyses, while the remaining three aliquots were stored for the subsequent preparation of PCL-brushite composites, obtained by maintaining an indicative ratio of 80 wt% PCL and 20 wt% pure or doped brushite. The procedure for the preparation of the composites will be described in detail in the following section.

Material characterization was performed using two complementary techniques: X-ray diffraction, referred to as XRD, and Fourier-transform infrared spectroscopy, referred to as FT-IR. The combined use of these two methods made it possible to obtain different but complementary information on the nature of the samples produced. The combination of the two techniques is particularly useful in the study of calcium phosphates, since XRD allows investigation of the crystalline structure of the material, whereas FT-IR makes it possible to analyze the molecular vibrations associated with the chemical bonds and functional groups present.

X-ray diffraction

X-ray diffraction is a characterization technique used to study the crystalline structure of materials. The principle underlying the analysis is based on the interaction between an X-ray beam and the crystallographic planes of the sample. When the material has an ordered structure, X-rays are diffracted at specific angles, generating a diffractogram consisting of characteristic peaks. The position, intensity, and shape of the peaks can provide information on the crystalline phase present, phase purity, and, qualitatively, the degree of crystallinity of the material. In general, sharper, narrower, and more intense peaks are indicative of higher crystallinity, whereas broader or less defined peaks may suggest lower crystallinity or the presence of structural modifications.

In the present work, XRD analysis was performed with the aim of verifying the formation of the brushite phase in the cements produced and comparing the behavior of the undoped sample with that of the samples containing Zn^{2+}. Brushite, or dicalcium phosphate dihydrate, has the chemical formula $CaHPO_4 \cdot 2H_2O$ and is characterized by a specific diffraction pattern.

Its identification by XRD is therefore useful for confirming that the reaction between β-TCP, MCPM, and the liquid phase occurred during cement setting. Furthermore, in the doped samples, comparison of the diffractograms may provide qualitative indications of possible differences in crystallinity, relative peak position, or the presence of residual or secondary phases. Indeed, in the literature, XRD analysis is frequently used in calcium phosphate-based cements to verify the presence of the expected hydrated phase and to identify any incompletely transformed reagents or secondary crystalline phases.

For the analysis, a small amount of powder from each sample was distributed on the sample holder in order to obtain a thin and as uniform as possible layer. This preparation is necessary to promote regular exposure of the material to the incident beam and reduce surface irregularities that could interfere with diffractogram acquisition. The samples analyzed were: pure brushite, brushite-Zn^{2+} 2%, brushite-Zn^{2+} 5%, and brushite-Zn^{2+} 10%.

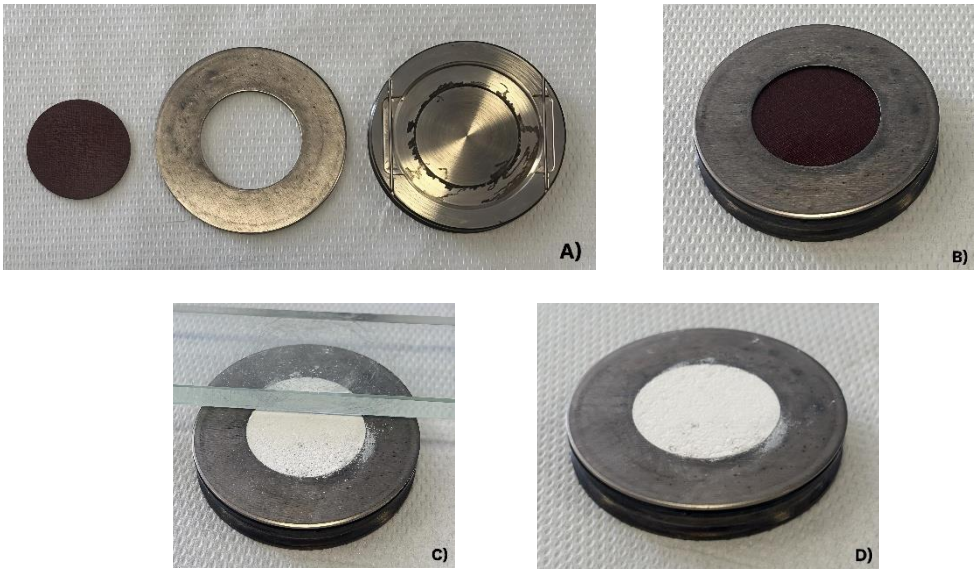

Figure 23: Preparation of the powder sample for XRD analysis. (A) Mold disassembled into its different components; (B) mold assembled before insertion of the material; (C) distribution and surface leveling of the powder by sliding a glass plate, in order to obtain a layer as uniform as possible; (D) sample inserted into the mold and ready for diffractometric acquisition.

The acquisitions were performed using a PANalytical AERIS diffractometer. The diffractograms were acquired over a scanning range approximately between 20° and 90° 2θ. At the end of the acquisition, which lasted approximately thirty minutes for each sample, the obtained data were visualized using DataViewer software. The diffractograms will subsequently be analyzed and discussed in the results section, with particular attention to the presence of the characteristic brushite peaks and to the comparison between the control sample and the Zn^{2+}-doped formulations.

Figure 24: Acquisition of diffractograms by XRD analysis. (A) PANalytical AERIS diffractometer used for the analysis of powder samples; (B) insertion of the mold containing the material into the analysis chamber of the instrument.

FT-IR spectroscopy

Fourier-transform infrared spectroscopy is an analytical technique based on the interaction between infrared radiation and matter. When a sample is crossed or irradiated by infrared radiation, specific chemical groups absorb energy at specific wavenumbers, depending on the bonds present and their vibrational modes.

Each functional group therefore has characteristic absorption bands, which can be used to identify the chemical composition of the material. The FT-IR spectrum represents absorbance, or transmittance depending on the acquisition mode, as a function of wavenumber, expressed in cm^{-1}.

In the case of calcium phosphates, FT-IR allows identification of the bands associated with phosphate groups PO_4^{3-}, hydrogen phosphate groups HPO_4^{2-}, and water molecules present in the crystalline structure or adsorbed on the surface of the material. This information is particularly relevant in the study of brushite, since it is a dicalcium phosphate dihydrate and contains crystallization water within its structure.

In the literature, FT-IR spectra of brushite show bands attributable to vibrations of phosphate groups, P–O(H) vibrations, and vibrations associated with water molecules, such as O–H stretching and H–O–H bending.

Therefore, FT-IR analysis represents a useful support to XRD for confirming the chemical nature of the cements obtained.

Furthermore, in materials doped with metal ions, possible variations in the position, intensity, or shape of the FT-IR bands may be related to modifications of the local chemical environment of the functional groups. The introduction of doping ions may in fact alter, even to a limited extent, the interactions between phosphate groups, water molecules, and the calcium phosphate crystal lattice. These variations should not necessarily be interpreted as direct and quantitative proof of ion incorporation into the lattice, but may represent a qualitative indication of possible structural and chemical modifications induced by doping.

In the present work, FT-IR spectroscopy was performed on powder samples of pure brushite and brushite doped with Zn^{2+} at 2%, 5%, and 10%.

Before spectrum acquisition, the instrument was calibrated by background acquisition. This operation is necessary to correct for the contribution of the measurement

environment, particularly that due to the presence of atmospheric components that may interfere with the analysis, such as humidity and carbon dioxide.

After background acquisition, a small amount of powder was placed on the instrument support and analyzed.

The analyses were performed using a Thermo Nicolet Nexus 380 FT-IR spectrometer with OMNIC software. For each sample, 100 scans were acquired in order to improve signal quality and reduce instrumental noise. The spectra were obtained in absorbance mode, over a range approximately between 4000 and 400 cm^{-1}. At the end of the acquisition, the obtained spectra were visualized using OMNIC software and subsequently compared with each other.

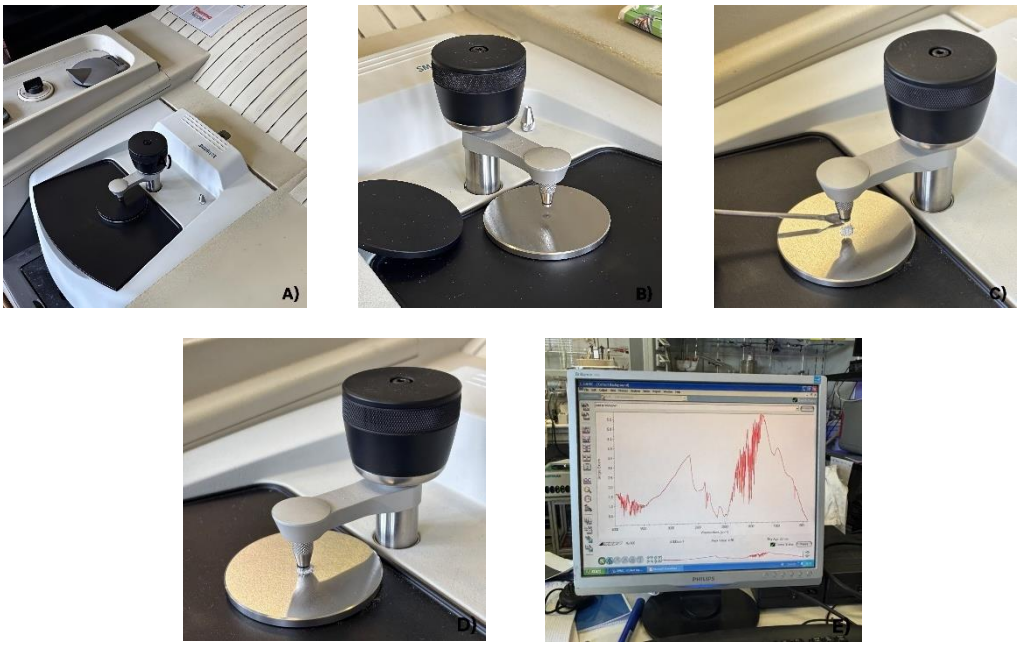

Figure 25: Acquisition of spectra by FT-IR spectroscopy. (A) Thermo Nicolet Nexus 380 FT-IR spectrometer used for the analysis of powder samples; (B) background acquisition before sample analysis; (C) placement of a small amount of powder on the instrument support; (D) material compressed on the support and ready for spectrum acquisition; (E) visualization of the spectrum using OMNIC software during acquisition of the 100 scans.

The aim of FT-IR analysis was to identify the characteristic bands of brushite and to compare the spectra of the doped samples with that of pure brushite. In particular, attention was focused on the spectral regions associated with phosphate and hydrogen phosphate groups and on the bands attributable to structural water. In the results section, comparison among the different formulations will allow evaluation of whether the increase in the nominal percentage of Zn^{2+} is associated with qualitative variations in the spectral profile.

Overall, XRD and FT-IR analyses were used as preliminary characterization tools for the cements obtained, with the aim of confirming brushite formation and comparing the undoped and zinc-doped formulations. The results obtained from these analyses will be discussed in the following sections together with the data derived from mechanical testing, in order to evaluate in an integrated manner the effect of Zn^{2+} doping on the chemical-structural and mechanical properties of the materials produced.

2.8 Preparation of the PCL-brushite composite

In order to make the developed material more processable by additive manufacturing techniques, a composite consisting of polycaprolactone (PCL) and Zn^{2+}-doped brushite was prepared. The fabrication of a polymer-ceramic composite was designed with the aim of combining the bioactive and osteoconductive properties of the inorganic calcium phosphate-based component with the greater processability and flexibility of the polymeric matrix. In particular, PCL is a biodegradable polymer widely used in tissue engineering, owing to its biocompatibility, low melting temperature, and possibility of being processed by extrusion and 3D printing techniques.

The introduction of the polymeric component also makes it possible to overcome some typical limitations of calcium phosphate-based cements, such as brittleness, poor deformability, and limited direct processability by additive manufacturing techniques. Conversely, the ceramic component allows the composite to acquire greater affinity with bone tissue compared with the polymer alone, while maintaining the biological rationale of the material developed in the previous phases. For this reason, the PCL-brushite composite was considered an intermediate formulation useful for the subsequent steps of extrusion, filament production, and 3D printing.

In this experimental phase, only the 2%, 5%, and 10% Zn^{2+}-doped brushite formulations were used. Pure brushite, instead, was not added to PCL, as it was used as a control material in the preliminary mechanical compression tests and in the chemical-structural characterization analyses by XRD and FT-IR. In this way, the initial comparison between the pure cement and the doped cements was maintained in the cement characterization phase, whereas composite preparation was focused exclusively on the zinc-containing formulations.

As described in the previous section, after compression testing and characterization analyses, the Zn^{2+}-doped brushite samples were reduced to powder by fragmentation and mechanical grinding. For each doping percentage, namely 2%, 5%, and 10%, the total amount of brushite obtained was divided into four aliquots, each equal to 12,5 g. One of the four aliquots was intended for chemical-structural characterization analyses, while the remaining three aliquots were used for the preparation of the PCL-brushite composites. This subdivision allowed three independent preparations to be obtained for each doping formulation, with the aim of promoting better

homogenization of the material and making the subsequent processing of the composite more controlled.

In parallel, the PCL, initially available as a filament wound on a spool, was manually cut into small portions. This preliminary operation was performed to facilitate the subsequent melting of the polymer and make mixing with the ceramic component easier.

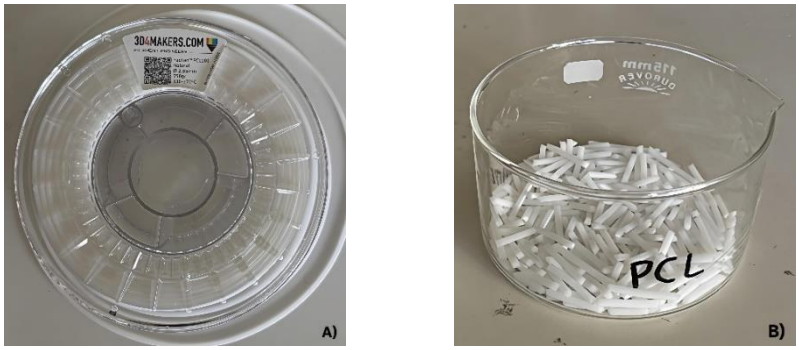

Figure 26: Preliminary preparation of PCL for the fabrication of the PCL-brushite composite. (A) Polycaprolactone (PCL) spool used as the polymeric matrix; (B) PCL cut into small portions in order to promote the subsequent melting of the material and facilitate its mixing with the ceramic component.

For each preparation, a compositional ratio of 80 wt% PCL and 20 wt% Zn^{2+}-doped brushite was maintained. Specifically, for each single preparation, 12.5 g of doped brushite, corresponding to 20 wt% of the final composite, and 50 g of PCL, corresponding to 80 wt%, were used. For each doping percentage, three distinct preparations were therefore carried out, obtaining PCL-brushite-Zn^{2+} 2%, PCL-brushite-Zn^{2+} 5%, and PCL-brushite-Zn^{2+} 10% composites.

Figure 27: Weighing of the components for the preparation of the PCL-brushite composite. (A) Weighing of Zn^{2+}-doped brushite, used as the ceramic component of the composite; (B) weighing of polycaprolactone (PCL), used as the polymeric matrix.

The composite was prepared by melt blending. In particular, the previously fragmented PCL was placed inside a beaker and positioned on a heating plate. Although a processing temperature range between approximately 130 °C and 170 °C was indicated on the material spool, during the experimental trials it was necessary to

set the heating plate to a temperature of approximately 190 °C. This choice was made to obtain adequate fluidity for mixing with the ceramic powder, also considering the probable dispersion of part of the heat between the surface of the plate, the beaker, and the material contained inside it.

Once the PCL had reached a sufficiently fluid consistency, the Zn^{2+}-doped brushite powder was progressively added to the molten polymeric matrix. The gradual addition of the powder was carried out to facilitate incorporation of the ceramic component and limit the formation of aggregates. The mixture was then manually processed using a spatula, with the aim of promoting the most uniform possible dispersion of the brushite particles within the molten PCL. This phase represented a critical step of the procedure, since the homogeneity of the composite directly depends on the distribution of the inorganic phase within the polymeric matrix.

During mixing, the material progressively acquired a viscous and dense consistency, compatible with the presence of the ceramic component dispersed within the polymer. Manual processing was continued until a macroscopically homogeneous mixture was obtained, in which the brushite powder appeared to be as fully incorporated as possible into the PCL matrix.

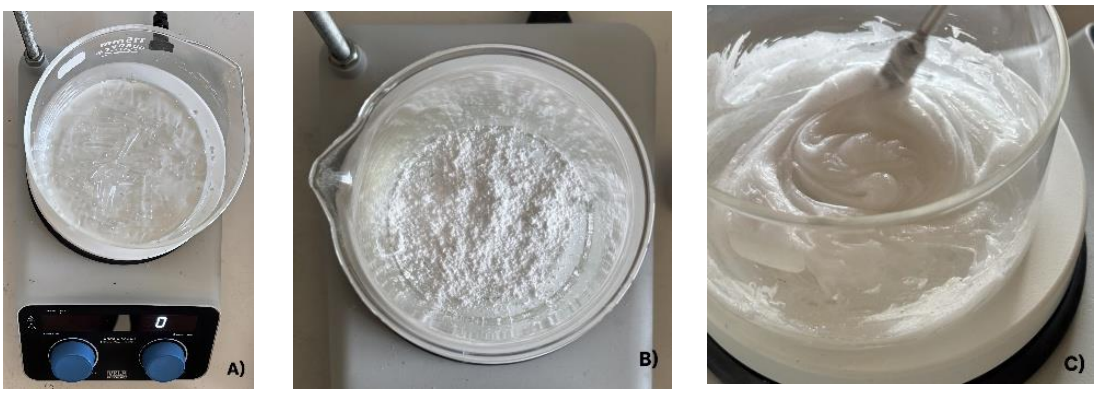

Figure 28: Preparation of the PCL-brushite composite by melt blending. (A) Melting of PCL fragments inside a beaker placed on a heating plate; (B) progressive addition of small amounts of Zn^{2+}-doped brushite to the molten PCL; (C) manual mixing using a spatula until a macroscopically homogeneous composite was obtained.

Once mixing was completed, small amounts of the still-warm composite were collected and inserted into a syringe, used as a manual extrusion system.

The PCL-brushite composite material was then manually extruded onto a heat-resistant glass surface, in order to obtain thin strips of material. The use of the glass support promoted cooling of the composite and allowed more easily manageable solid portions to be obtained. Once cooled, the resulting strips were cut into small segments, in order to produce pellets of reduced size.

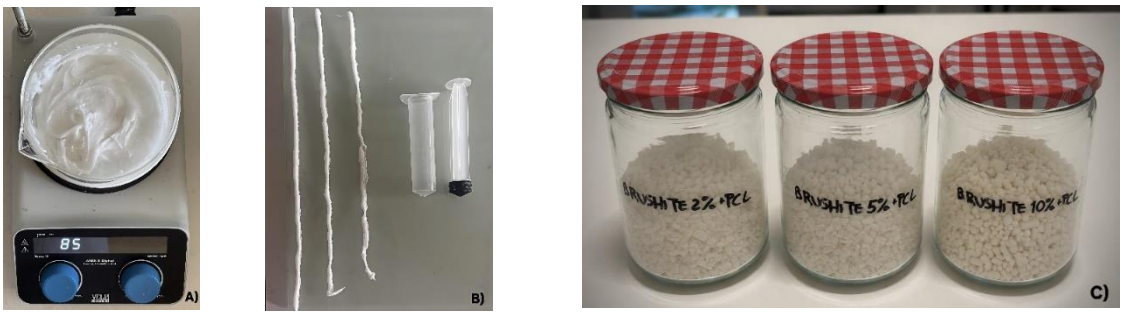

Figure 29: Manual extrusion and production of PCL-brushite composite pellets. (A) PCL-brushite composite at the end of mixing, ready to be inserted into the syringe and manually extruded; (B) syringe used for manual extrusion and composite strips obtained on a glass surface; (C) PCL-brushite composite pellets obtained and separated according to the Zn^{2+} doping percentage of the brushite: 2%, 5%, and 10%.

Pellet production represented an intermediate step necessary to make the composite more easily usable in the subsequent processing procedures. Indeed, the pellets obtained from the different formulations were intended for the subsequent filament extrusion phase, with the final aim of obtaining a PCL-brushite composite material processable by 3D printing. In this way, composite preparation constituted the connecting step between the synthesis and characterization of zinc-doped brushite cements and the development of a material potentially usable for additive manufacturing applications in the regenerative field.

2.9 Production of the composite filament by extrusion

The PCL-brushite composite pellets obtained in the previous phase were subsequently used as starting material for the production of the composite filament intended for 3D printing. This phase represented a fundamental step of the experimental work, as it made it possible to transform the composite previously prepared by melt blending into a continuous material, potentially compatible with fused deposition additive manufacturing systems.

Filament production was carried out using a Felfil Evo polymer material extruder. This instrument is designed to produce plastic filament for 3D printers starting from industrial pellets or appropriately fragmented plastic materials. In the present work, the Felfil Evo was used to extrude the PCL-brushite composite in the form of a continuous filament. The instrument is equipped with an upper hopper for material loading, a screw conveyor for transporting the pellets toward the heated zone, and a nozzle through which the molten material is extruded in the form of filament.

Figure 30: Felfil Evo extruder used for the production of the composite filament. (A) Front view of the instrument, with a display for visualization of the main process parameters, including temperature, screw rotation speed, and electrical absorption; the parameter adjustment knob and the upper hopper for pellet loading are also visible. (B) Side view of the instrument, with particular emphasis on the nozzle through which the filament is extruded.

The operating principle of the extruder is therefore based on the insertion of the pellets into the hopper, from which the material is progressively dragged by the screw conveyor toward the heating chamber. During this path, the composite is subjected to heating and compression until it reaches a sufficiently fluid consistency to be pushed through the extrusion nozzle. The outgoing material thus takes the form of a continuous filament, whose diameter mainly depends on the nozzle used, the set temperature, the screw rotation speed, and the cooling conditions of the freshly extruded material.

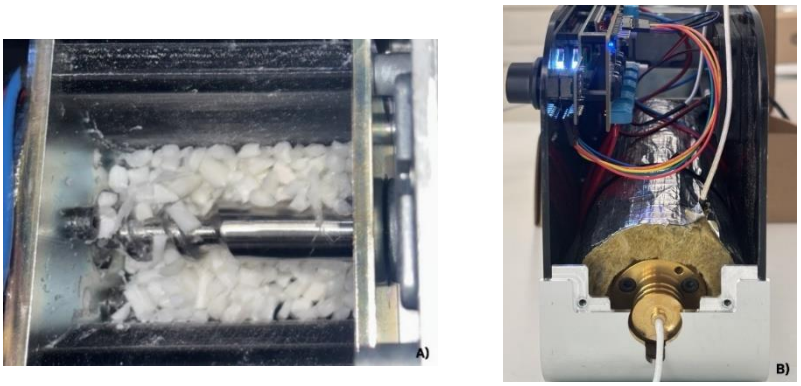

Figure 31: Pellet loading and extrusion phase of the Zn^{2+}-containing PCL-brushite composite, after removal of the instrument cover, performed to facilitate material loading. (A) Composite pellets inserted into the hopper and progressively dragged by the screw conveyor are visible. (B) Side view of the instrument during extrusion of the composite filament through the nozzle.

In an initial phase of the work, the extruder had been configured with a 2.85 mm nozzle, since the subsequent printing of the material using an Ultimaker S3 printer, compatible with filaments of this diameter, had been hypothesized. However, due to the difficulties encountered when using this printer with the developed composite material, it was subsequently decided to replace the 2.85 mm nozzle with a 1.75 mm nozzle. This modification was made with the aim of obtaining a filament with a smaller diameter, potentially more suitable for use with 3D printers compatible with 1.75 mm filaments and easier to manage in the subsequent printing trials.

Filament production required several preliminary trials to identify extrusion parameters suitable for the PCL-brushite composite. During an initial trial, the instrument temperature was set to approximately 170 °C. This choice was initially influenced by the previous composite preparation phase by melt blending, during which it had been necessary to set the heating plate to temperatures close to 190 °C in order to obtain sufficient fluidity of the PCL inside the beaker. However, the use of such a high temperature in the extruder proved to be suboptimal.

Although it was initially possible to obtain a filament, this appeared darker than the filaments produced subsequently, suggesting a possible effect of thermal treatment on the material. In addition, the excessive temperature caused heating that was not limited to the melting chamber alone, but also extended to the portion of the screw conveyor and to the feeding zone. As a result, the pellets present in the upper hopper began to soften prematurely, becoming malleable and aggregating with each other. This phenomenon led to the formation of a single block of material inside the hopper,

preventing the screw conveyor from correctly dragging the pellets toward the heated zone and interrupting the regular extrusion process.

Figure 32: First extrusion trial of the PCL-brushite composite using a 2,85 mm nozzle, performed by setting a temperature of approximately 170 °C. The filament obtained appears macroscopically darker than the filaments produced in the subsequent trials, suggesting a possible effect of excessive thermal treatment on the material.

This critical issue highlighted the need to markedly reduce the working temperature compared with that used during the melt blending phase. After the initial trials, the extruder temperature was therefore set at around 90 °C. This value proved to be more suitable for allowing controlled melting of the polymeric component without causing excessive heating of the feeding zone. The screw rotation speed was set at 6 rpm, in order to promote continuous advancement of the material inside the extruder.

During the extrusion process, the composite pellets undergo partial remelting of the polymeric matrix. This phase may contribute to further improving the distribution of the ceramic component within the PCL, since the material is once again heated, compressed, and forced through the nozzle. In this sense, extrusion does not represent only a filament-shaping step, but also an additional reprocessing step of the composite, potentially useful for increasing the macroscopic homogeneity of the material.

A further critical aspect concerned the cooling phase of the filament exiting the nozzle. The Felfil Evo is designed to operate on a surface, generally a table, allowing the extruded filament to fall downward before reaching the underlying surface. This vertical distance is referred to as the drop and, according to the instrument instructions, can be modified depending on the material used in order to obtain a more constant filament. In the case of the PCL-brushite composite, the high deformability of the freshly extruded material made it necessary to modify this configuration.

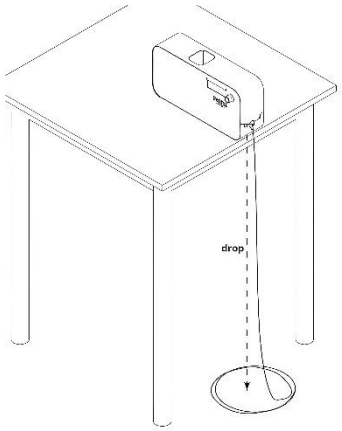

Figure 33: Operating scheme of the Felfil Evo extruder reported in the instrument manual. The image shows the standard configuration of use, in which the extruder is placed on a work surface and the extruded filament falls downward before reaching the underlying surface. This vertical distance, defined as the drop, can be modified according to the processed material in order to improve filament regularity.

In particular, when the filament was allowed to fall freely from the nozzle, the weight of the still-warm material tended to stretch and excessively thin the filament, compromising its dimensional regularity. To reduce this phenomenon, the extruder was positioned so as to maintain only a short falling distance between the nozzle and the collection surface. For this purpose, the glass build plate of the Ultimaker S3 printer was placed below the nozzle, allowing the freshly extruded filament to rapidly come into contact with a cold surface after only a few centimeters of travel.

The use of the glass plate also made it possible to manually guide the filament and progressively slide it during extrusion, preventing the material from accumulating directly below the nozzle. This precaution allowed the formation of still-warm composite masses to be reduced, limited the thinning caused by the weight of the filament, and promoted more regular cooling of the extruded material. Manual management of the exiting filament was therefore necessary to maintain greater continuity of the produced material and to reduce macroscopic irregularities.

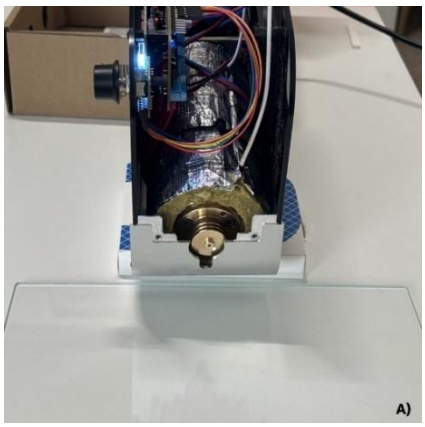

Figure 34: Set-up used for the production and cooling of the Zn^{2+}-containing PCL-brushite composite filament. (A) Positioning of the extruder with the glass build plate of the Ultimaker S3 printer placed below the nozzle. (B) Freshly extruded composite filament, which, after a short falling distance, comes into contact with the glass plate. During extrusion, the filament was manually guided and made to slide over the glass surface, in order to promote cooling and avoid accumulation of the material directly below the nozzle.

Filament production was overall slow and laborious. Due to the low extrusion speed, the need to manually control cooling, and the particular composition of the material, the production of each filament required approximately 3–4 hours. The filament obtained was collected manually and macroscopically evaluated in terms of continuity, regularity, and handling.

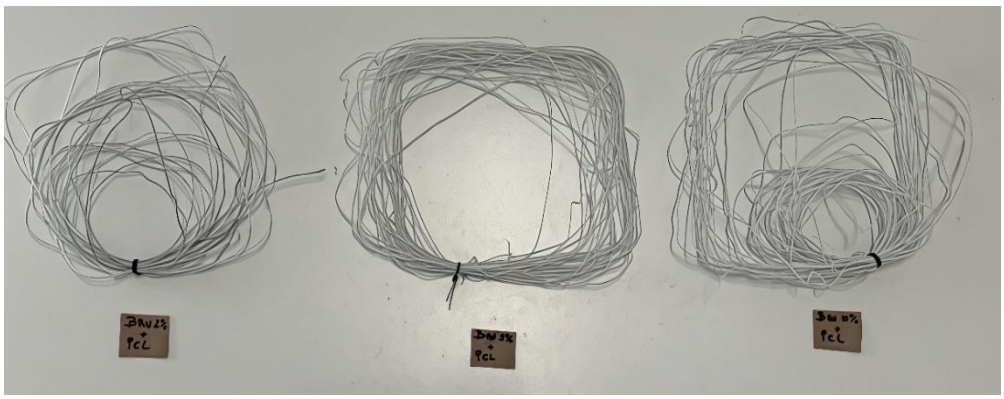

Figure 35: Composite filaments obtained by extrusion starting from Zn^{2+}-containing PCL-brushite pellets. The filaments were produced in the three formulations containing brushite doped with Zn^{2+} at 2%, 5%, and 10%.

Obtaining a sufficiently homogeneous filament with adequate mechanical consistency represents an essential requirement for subsequent feeding into the 3D printer and for ensuring controlled material deposition during the printing process. Overall, the production of the composite filament using the Felfil Evo represented a particularly delicate experimental phase, characterized by the need to progressively optimize temperature, extrusion speed, and cooling conditions.

The difficulties encountered highlighted how the behavior of the PCL-brushite composite differs from that of a pure commercial polymer and therefore requires specific processing parameters. Despite these critical issues, this phase made it possible to obtain a composite filament based on PCL and Zn^{2+}-doped brushite, usable as starting material for the subsequent 3D printing trials.

2.10 Fabrication of samples for mechanical testing and biological evaluation by 3D printing

After production of the PCL-brushite composite filament by extrusion, the material obtained was used for the fabrication of samples intended for subsequent mechanical testing and biological evaluation. This phase represented the final step of the experimental material transformation process, starting from the synthesis of zinc-doped brushite cements and leading to the production of three-dimensional specimens by 3D printing.

The additive manufacturing of the samples was preceded by the digital design of the models to be printed. The samples were designed using the 3D modeling software Tinkercad, which was used to create simple and controlled geometries. Two different types of samples were designed: rectangular specimens intended for flexural mechanical testing and discs intended for subsequent biological analyses.

The specimens for flexural testing were designed with dimensions of 70 mm in length, 8 mm in width, and 3 mm in thickness. These dimensions were selected with reference to the geometries commonly used for flexural tests on polymeric and composite materials, according to the indications of ISO 178 and ASTM D790 standards. The discs for biological analyses were instead designed with a diameter of 18 mm and a thickness of 0,8 mm. This geometry was chosen to allow insertion of the samples into a multiwell plate, thereby making them compatible with the subsequent experimental phases of biological evaluation.

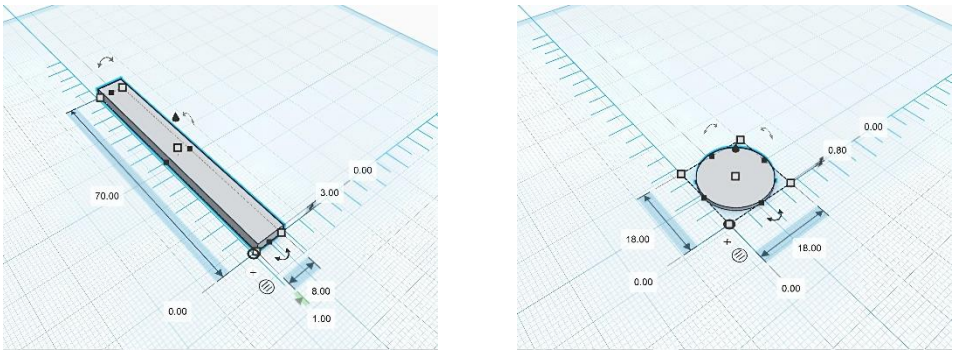

Figure 36: Digital modeling of the samples using Tinkercad software.

Once digital modeling had been completed, the samples were exported in STL format. This format is one of the most commonly used formats in 3D printing, as it describes the three-dimensional geometry of the object through a mesh of triangular surfaces. The STL files were subsequently imported into slicing software, which is necessary to

convert the three-dimensional model into instructions that can be interpreted by the 3D printer. The slicer allows the model to be virtually divided into successive layers and generates the G-code file, containing the commands related to machine movements, temperatures, printing speed, material extrusion, and other operating settings.

In an initial phase, Ultimaker Cura software was considered for slicing the models, since sample printing was initially planned using an Ultimaker S3 printer. The Ultimaker S3 is an enclosed Cartesian 3D printer, in which movements along the X and Y axes are mainly managed by the print head, while the build plate moves vertically along the Z axis. However, during the preliminary trials, difficulties were encountered in loading and managing the composite filament produced. These difficulties were likely related to the experimental nature of the filament, characterized by greater softness, possible diameter irregularity, and the presence of the ceramic component dispersed within the polymeric matrix. For this reason, the use of the Ultimaker S3 was abandoned and the choice was directed toward a bed-slinger printer.

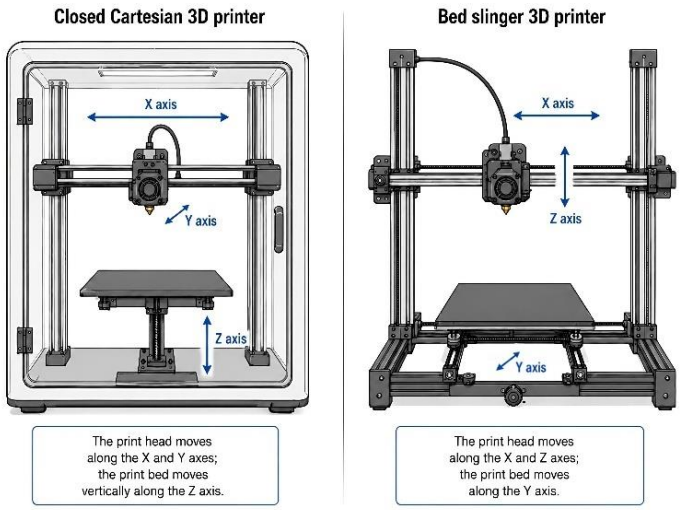

Figure 37: Schematic comparison between an enclosed Cartesian 3D printer and a bed-slinger 3D printer. In the enclosed Cartesian printer, the print head moves along the X and Y axes, while the build plate moves vertically along the Z axis. In the bed-slinger printer, instead, the print head moves along the X and Z axes, while the build plate moves along the Y axis.

Bed-slinger printers have a different configuration compared with enclosed Cartesian printers: the extruder moves along the X and Z axes, while the build plate moves along the Y axis. Initially, the possibility of using a Prusa Mini was evaluated. However, in this case as well, difficulties were encountered in loading the composite filament. In particular, during the feeding phase, the filament tended to twist near the drive gear, without being able to correctly reach the nozzle. This problem was attributed to the distance between the filament feeding system and the hot-end, which is typical of

configurations in which the filament must travel a relatively long path before reaching the melting zone.

To overcome this critical issue, a printer equipped with a filament feeding system integrated into the extruder assembly was selected, so that the drive gear was positioned close to the hot-end. The final choice therefore fell on the Anycubic Kobra 3, a bed-slinger printer characterized by a compact extruder assembly, in which the filament feeding system is located close to the melting zone. This configuration proved to be more suitable for processing the PCL-brushite composite filament, as it reduced the distance that the filament had to travel before reaching the nozzle, limiting the risk of deformation, bending, or loss of feeding during loading.

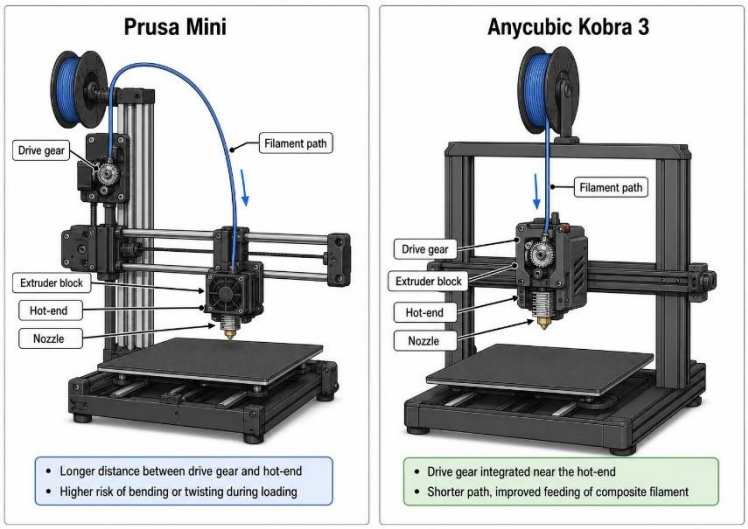

Figure 38: Schematic comparison between the filament feeding configuration in the Prusa Mini and in the Anycubic Kobra 3. In the Prusa Mini, the feeding system, represented by the drive gear, is separated from the hot-end and nozzle, forcing the filament to travel a longer distance before reaching the melting zone. This configuration may increase the risk of bending, twisting, or loss of feeding in the case of soft experimental filaments or filaments with a not perfectly constant diameter. In the Anycubic Kobra 3, instead, the feeding system is integrated into the extruder block and positioned close to the hot-end and nozzle, reducing the filament path and facilitating feeding of the PCL-brushite composite.

Once the 3D printer to be used had been selected, it was also necessary to modify the software management of the machine. In a 3D printer, firmware can be defined as the internal software that controls the operation of the machine, coordinating axis movement, temperature management, extruder control, safety procedures, and G-code execution. The original firmware of the Anycubic Kobra 3 has some operational limitations, including internal locks that prevent extrusion below a certain temperature, generally to avoid cold extrusion phenomena and protect the filament feeding system.

Initially, it was hypothesized that the PCL-brushite composite should be extruded at temperatures below 100 °C, similarly to what was observed during the filament extrusion phase with the Felfil Evo. For this reason, the Rinkhals firmware was installed, allowing more flexible management of the printer through a control environment compatible with the Fluidd interface. The installation of Rinkhals made it possible to use the printer in a more controllable way than with the original firmware, allowing different machine parameters to be monitored and modified, G-code files generated by external slicers to be uploaded, nozzle and bed temperatures to be managed, the extruder to be manually controlled, and configuration files to be edited.

In an initial phase, this modification was useful to lower the minimum extrusion limit and verify the behavior of the material at reduced temperatures. Subsequently, during the printing trials, it was observed that the temperature actually required to print the composite was not below 100 °C, but approximately 190 °C. Nevertheless, the installation of Rinkhals still proved to be decisive, not so much for the regulation of the final printing temperature, but rather for the possibility of manually controlling the rotation of the drive gear and facilitating the loading of the composite filament.

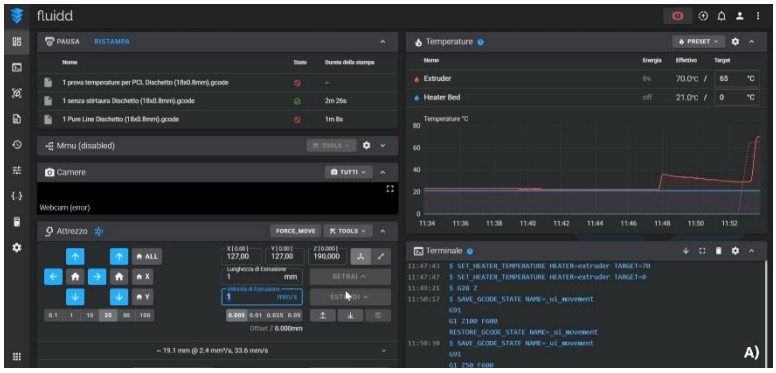

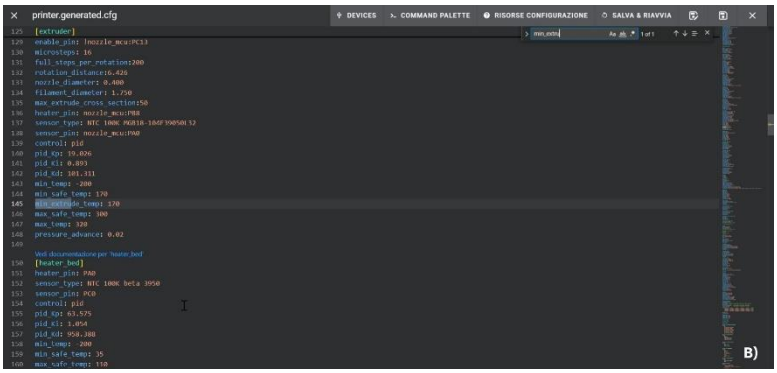

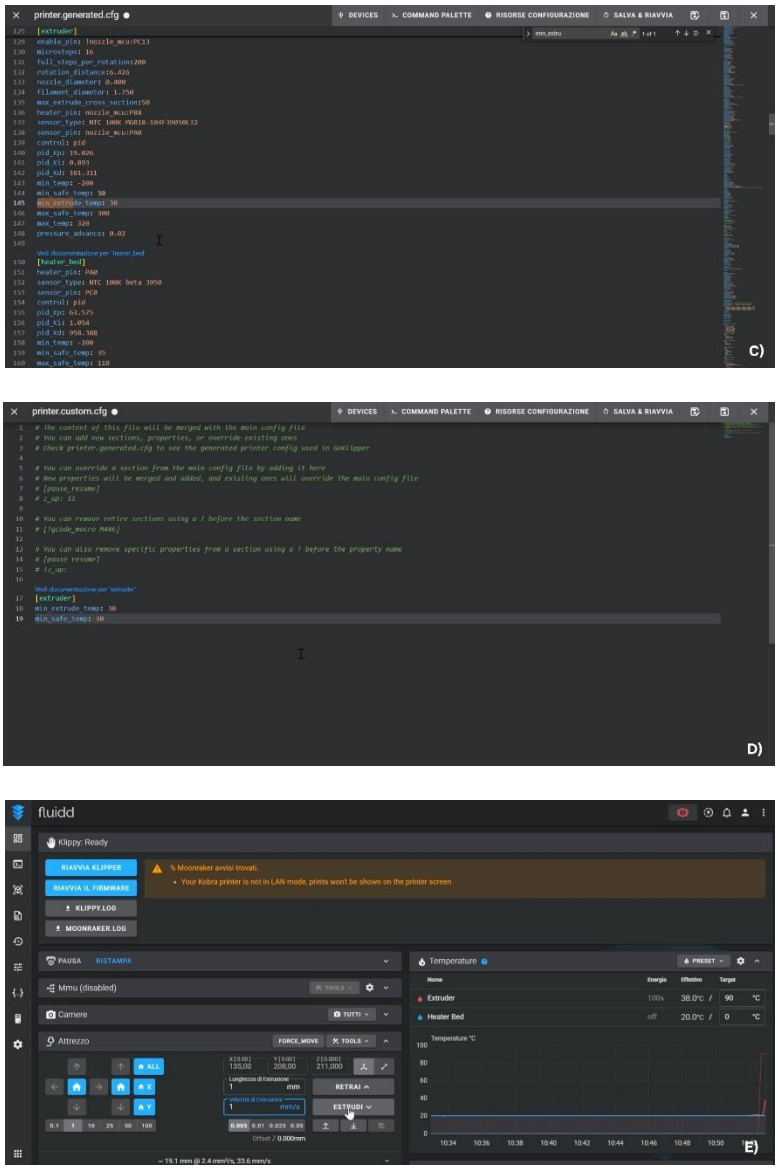

Figure 39: Modification of the extruder safety limits and manual control of filament advancement through the Fluidd interface. (A) Fluidd interface used to control the Anycubic Kobra 3, with the extruder management panel and the “Extrude” button to manually command filament advancement through rotation of the drive gear. With the initial configuration, manual extrusion was not allowed below the minimum temperature set by the firmware. (B) Original configuration file, in which the min_extrude_temp and min_safe_temp parameters were set to 170 °C. (C) Modification of the min_extrude_temp and min_safe_temp parameters, both lowered to 30 °C to allow extrusion trials at lower temperatures. (D) Insertion of the modification into the printer.custom.cfg file, used to override the parameters of the main configuration. (E) Fluidd interface after the modification, in which manual filament extrusion can be commanded even with an extruder temperature slightly above 30 °C.

Filament loading in fact represented one of the most delicate phases of the process. The experimentally produced filament had characteristics different from those of a standard commercial filament: it was softer, less regular in diameter, and consisted of a polymeric matrix loaded with ceramic particles. These characteristics made feeding less predictable and required more accurate control of material advancement. The Fluidd interface made it possible to manually command extrusion and to verify in real

time the behavior of the filament during loading, facilitating its reaching of the hot-end and reducing the risk of clogging.

In parallel with printer configuration, the slicing workflow was also optimized. Initially, attempts were made using OrcaSlicer, configuring the printer as a machine compatible with the Klipper/Moonraker environment. However, during the trials, difficulties were encountered related to sending or executing the print files. Subsequently, PrusaSlicer was used, creating a custom profile for the Anycubic Kobra 3. The profile was set considering a machine compatible with Klipper firmware, with a build volume suitable for the printer dimensions and with parameters that could be modified according to the experimental material used.

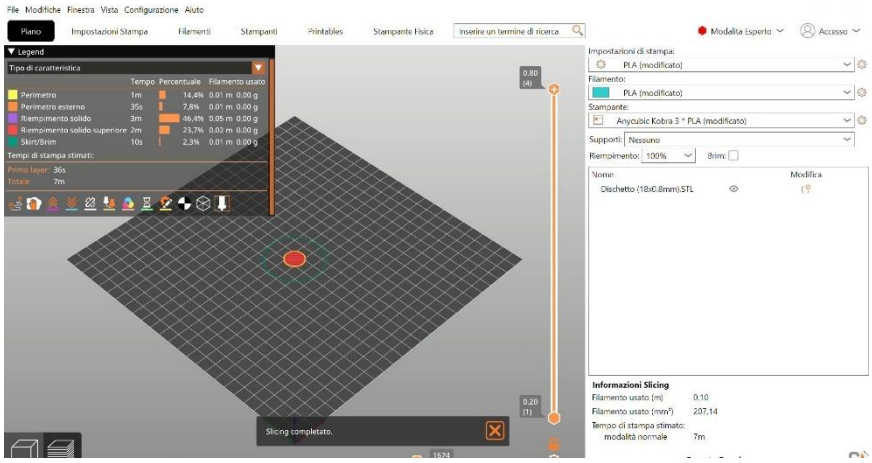

Figure 40: Slicing of the digital model using PrusaSlicer. After designing the samples in Tinkercad and exporting them in STL format, the models were imported into PrusaSlicer for generation of the G-code file.

With PrusaSlicer, it was possible to generate G-code files compatible with management through Fluidd. The initial G-code was also modified to reduce some problems observed during the first trials. In particular, during the homing and initial leveling phases, early heating of the nozzle caused material leakage and the formation of residues or curling near the nozzle. To limit this phenomenon, a start-up sequence was set in which the build plate was brought to the working temperature before the nozzle, keeping the latter at a low temperature during the preliminary positioning and calibration phases. Only after homing had been completed was the nozzle brought to the printing temperature. In addition, a purge line and an initial nozzle-cleaning phase were introduced, useful for stabilizing extrusion before the beginning of sample printing. The final G-code was also modified so as to lift the extruder further at the end of printing, facilitating sample removal and nozzle cleaning.

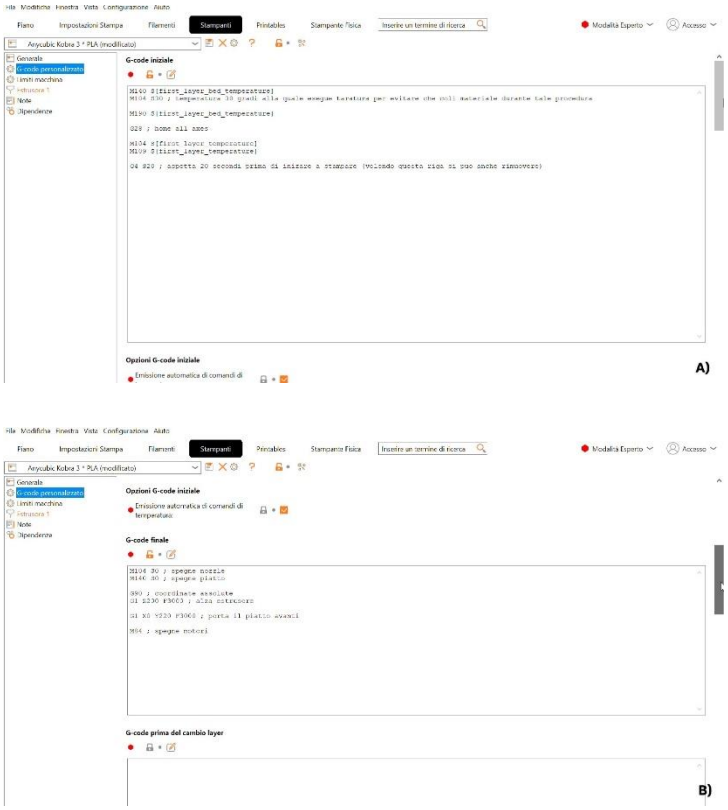

Figure 41: Customization of the initial and final G-code in PrusaSlicer. (A) Modification of the initial G-code of the Anycubic Kobra 3, set to initially heat the build plate and keep the nozzle at a low temperature during the preliminary homing and calibration phases, in order to limit premature material leakage and the formation of residues on the nozzle. Only after completion of these operations is the nozzle brought to the printing temperature. (B) Modification of the final G-code, set to turn off the nozzle and build plate, lift the extruder, and move the build plate forward, facilitating sample removal and nozzle cleaning at the end of printing.

Once the PrusaSlicer-Fluidd-Anycubic Kobra 3 system had been configured, slicing of the two types of samples, namely discs and rectangular specimens, was performed. The main printing parameters were selected taking into account the composite nature of the material. In particular, a 1 mm diameter nozzle was used. The use of a nozzle with a large diameter compared with those commonly used in FFF printing was motivated by the presence of ceramic particles dispersed within the polymeric matrix, which could have increased the risk of nozzle clogging with smaller diameters.

The nozzle temperature was set to 190 °C, a value that allowed sufficient fluidity of the material during deposition. The build plate temperature was set to 40 °C, with the aim of promoting initial adhesion of the sample without causing excessive heating of the deposited material. The layer height was set to 0.2 mm, while the infill was set to 100%, in order to obtain samples that were as full and compact as possible, suitable for subsequent mechanical testing and biological evaluations. The printing speed was

kept low, equal to 5 mm/s, to promote more controlled deposition of the composite and reduce the risk of irregularities during extrusion.

Before printing the actual sample, the generation of two skirt loops at a distance of approximately 15 mm from the model was set. The skirt was used as a preliminary strategy to stabilize material flow and verify correct extrusion before the beginning of sample deposition. This phase proved particularly useful considering the experimental nature of the filament and the need to ensure continuous and regular extrusion.

Parameter	Value used
3D printer	Anycubic Kobra 3
Firmware/control interface	Rinkhals / Fluidd
Slicing software	PrusaSlicer
Nozzle diameter	1 mm
Nozzle temperature	190 °C
Build plate temperature	40 °C
Layer height	0.2 mm
Infill	100%
Printing speed	5 mm/s
Skirt	2 loops
Skirt distance from the sample	15 mm
Disc printing time	approximately 7 min
Rectangular specimen printing time	approximately 40 min

Table 6: Main parameters used for 3D printing of the PCL-brushite composite samples.

The G-code files thus obtained were uploaded through the Fluidd interface and sent to the Anycubic Kobra 3 for printing. The printing time varied depending on the sample geometry. In particular, printing one disc required approximately 7 minutes, whereas printing one rectangular specimen for flexural testing required approximately 40 minutes.

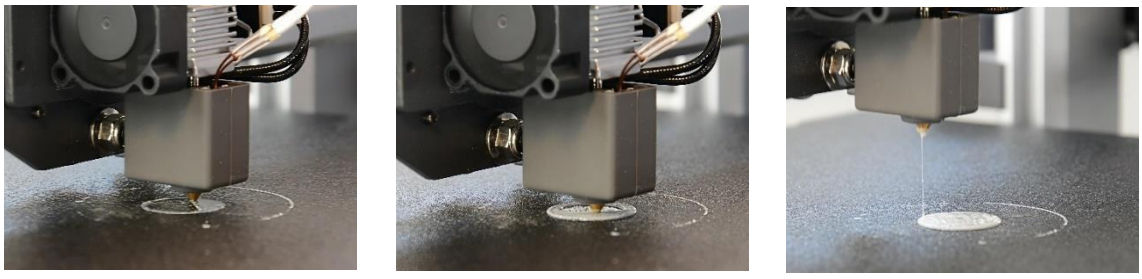

Figure 42: 3D printing steps of the PCL-brushite composite discs intended for biological evaluation. The images show the progressive deposition of the material using the Anycubic Kobra 3: initial stabilization of extrusion and deposition of the skirt around the model, subsequent deposition of the composite material onto the build plate, and completion of the disc with a circular geometry.

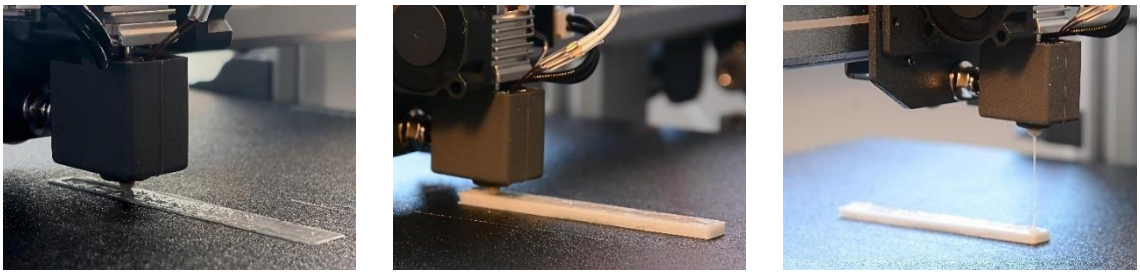

Figure 43: 3D printing steps of the PCL-brushite composite rectangular specimens intended for flexural mechanical testing. The images show the deposition of the composite material during fabrication of the specimen, from the initial printing phase to completion of the rectangular specimen, obtained with full infill and a geometry defined according to the designed dimensions.

For each Zn^{2+} doping percentage of brushite, namely 2%, 5%, and 10%, 10 discs intended for biological evaluation and 5 rectangular specimens intended for flexural mechanical testing were produced. Overall, 30 discs and 15 rectangular specimens were therefore fabricated. At the end of printing, the samples were removed from the build plate and macroscopically evaluated in terms of integrity, geometrical regularity, and continuity of deposition.

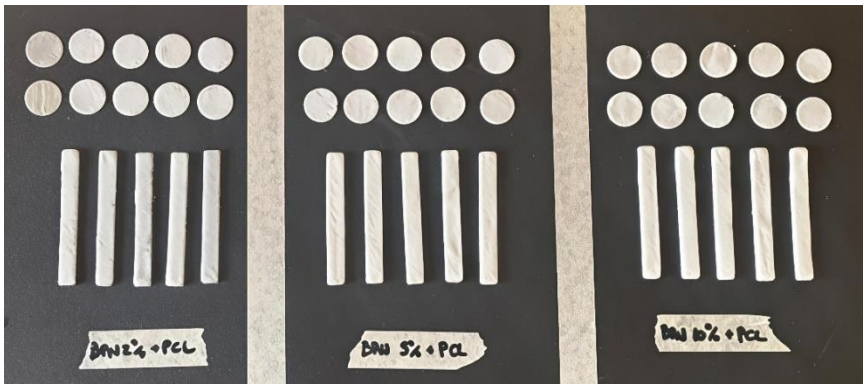

Figure 44: 3D-printed PCL-brushite composite samples obtained for the three Zn^{2+} doping formulations. For each formulation, namely brushite-Zn^{2+} 2%, 5%, and 10%, 10 discs intended for biological evaluation and 5 rectangular specimens intended for flexural mechanical testing were produced.

Overall, the fabrication of the samples by 3D printing required a preliminary phase of both hardware and software optimization. The choice of the printer, firmware modification, manual management of filament loading, nozzle selection, and definition of the slicing parameters were necessary steps to adapt the FFF process to an experimental composite material based on PCL and Zn^{2+}-doped brushite. This phase allowed the production of printed samples intended for flexural mechanical testing and biological evaluation, completing the experimental pathway of material transformation from the initial cement phase to the final three-dimensional manufactured object.

2.11 Flexural mechanical testing

The mechanical properties of the Zn^{2+}-doped PCL-brushite composites were evaluated by three-point bending tests, performed on the rectangular specimens previously obtained by 3D printing. This test was carried out with the aim of preliminarily characterizing the mechanical behavior of the printed composites and comparing the three formulations containing brushite doped with Zn^{2+} at 2%, 5%, and 10%.

The tests were performed using the Zwick/Roell universal testing machine, already used for the mechanical compression tests, but configured with a different testing device specifically designed for flexural testing. In particular, a system consisting of two lower supports, on which the specimen was positioned, and a central upper loading nose, intended to apply the load in the middle region of the sample, was mounted. The distance between the two lower supports, also defined as the span length, was set at 50 mm. In this configuration, the specimen is therefore subjected to a centrally applied load, resulting in progressive flexural deformation.

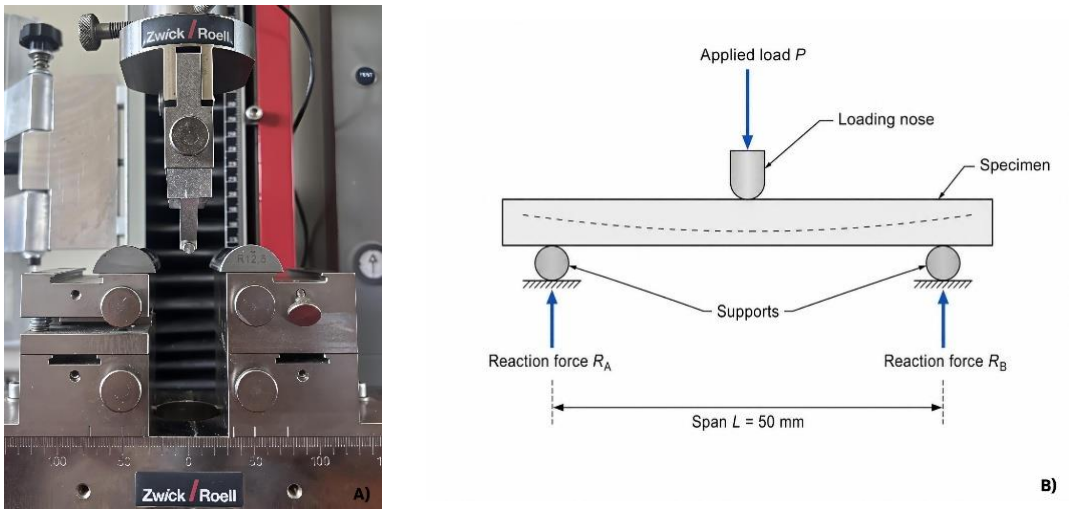

Figure 45: Set-up of the three-point bending mechanical test. (A) Flexural testing device mounted on the Zwick/Roell universal testing machine, with two lower supports and a central upper loading nose for load application. (B) Representative scheme of the three-point bending test, showing the centrally applied load, the support reactions at the two supports, and the span length of 50 mm.

Before performing the test, each printed rectangular specimen was measured using a digital caliper, in order to record the actual dimensions of the sample cross-section. In particular, the thickness and width of the specimen were measured, as these parameters were necessary for the subsequent processing of the mechanical data. Based on these values, the cross-sectional area of the sample, indicated as A_0, was defined. This step was necessary because, since the samples were obtained by 3D printing from an experimental composite filament, the actual dimensions of the

specimens could show slight differences compared with the theoretical dimensions set during the modeling phase.

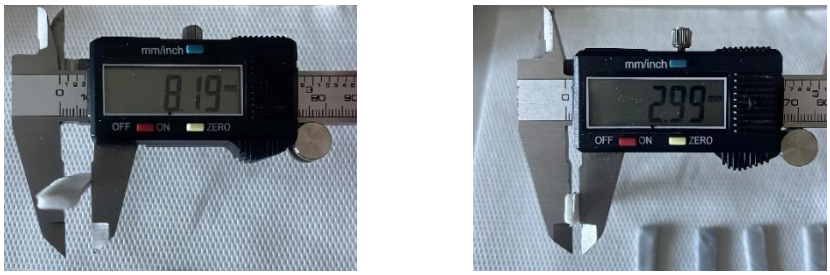

Figure 46: Preliminary dimensional measurement of the 3D-printed rectangular specimens using a digital caliper. The images show the measurement of the specimen thickness and width, parameters necessary for defining the sample cross-section and for the subsequent processing of the mechanical data obtained from the flexural test.

After dimensional measurement, the rectangular specimen was positioned horizontally on the two lower supports of the flexural testing device, taking care to center the sample with respect to the upper loading nose. The loading nose was then brought into correspondence with the central portion of the specimen, and the test was started using testXpert III software, used for machine control and experimental data acquisition.

Figure 47: Execution steps of the three-point bending test on PCL-brushite composite rectangular specimens. The images show the positioning of the specimen on the two lower supports, the alignment of the upper loading nose in the central region of the sample, and the progressive deformation of the specimen during load application using the Zwick/Roell universal testing machine.

During the test, the upper loading nose progressively applied the load in the central region of the rectangular specimen, inducing bending of the sample until the predetermined deformation or the maximum recorded mechanical response was reached. The software allowed acquisition of the flexural stress-strain curve, from which the main mechanical parameters of the material were obtained. In particular, the flexural elastic modulus (E_f), maximum flexural stress (σ_{fM}), and strain corresponding to the maximum stress (ε_{fM}) were considered. The dimensional values of the samples, namely thickness (h), width (b), and cross-sectional area (A_0), were also recorded.

The tests were performed on samples belonging to the three Zn^{2+}-doped PCL-brushite composite formulations. For each doping percentage, namely 2%, 5%, and 10%, five 3D-printed rectangular specimens were tested, for a total of fifteen flexural tests. The results obtained were subsequently organized in tables and represented by stress-strain graphs, in order to compare the mechanical behavior of the different formulations.

2.12 Biological evaluation

The biological evaluation of the Zn^{2+}-doped PCL-brushite composite samples was set up as a preliminary phase to analyze cell behavior in contact with the discs obtained by 3D printing. Since the complete investigation of the biological tests represents the subject of the parallel thesis of a colleague, the present work reports a general summary of the procedure performed.

Before the biological tests, the 3D-printed discs were subjected to cold chemical sterilization. Autoclave sterilization was not used, since the high temperatures and steam pressure could have altered the polycaprolactone matrix, deformed the geometry of the samples, or modified the structure of the polymer-ceramic composite. For this reason, Sporigerm Peracetic Plus was used, a powder product capable of generating peracetic acid after dissolution in water.

The sterilizing solution was prepared according to the manufacturer's instructions by dissolving the powder in warm water at approximately 35 °C and allowing it to activate for approximately 15 minutes. The discs were kept separated according to the zinc doping percentage, namely 2%, 5%, and 10%, in order to avoid cross-contamination among the experimental groups. The procedure included a first decontamination/disinfection phase with Sporigerm Peracetic Plus at a concentration of 8 g/L for 10 minutes, followed by rinsing, and a subsequent sterilization phase at a concentration of 16 g/L for 10 minutes.

At the end of the treatment, the samples were thoroughly rinsed with sterile water and/or sterile saline solution, in order to remove any residues of the sterilizing agent. Subsequently, the discs were left to dry under sterile conditions on sterile gauze, protected with an additional gauze, and then packaged while keeping the different experimental groups separated. Before cell seeding, the samples were visually inspected to verify the absence of evident macroscopic alterations, such as deformation, swelling, softening, fragmentation, or surface disintegration.

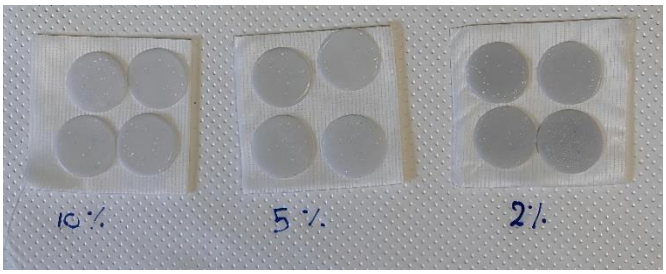

Figure 48: Zn^{2+}-doped PCL-brushite composite discs after the cold chemical sterilization procedure. The samples were kept separated according to the doping percentage, namely 2%, 5%, and 10%, in order to avoid cross-contamination among the different experimental groups.

The cells used for the biological evaluation were stem/mesenchymal cells derived from dental pulp, referred to as dental pulp stem cells (DPSCs) or dental pulp-derived mesenchymal/stromal cells. Dental pulp was obtained from extracted teeth, and the cells were isolated by enzymatic digestion with collagenase I and dispase. The isolated cells were then maintained in culture in DMEM supplemented with fetal bovine serum (FBS), penicillin, and streptomycin, in an incubator at 37 °C, 5% CO_2, and humidified atmosphere.

An important critical issue of this phase is represented by the high risk of contamination of primary cultures from dental pulp, since extracted teeth come from the oral cavity, an environment naturally colonized by microorganisms. For this reason, only viable, adherent, proliferating, and contamination-free cultures were used.

Before seeding onto the discs, the adherent cells were detached using 1X trypsin-EDTA, centrifuged, and resuspended in fresh medium. The number of available cells was determined using a Neubauer chamber, in order to prepare a cell suspension suitable for seeding. Approximately 50.000 cells were seeded onto each disc in an initial volume of approximately 300 µL, selected to promote direct contact between the cells and the material surface. After approximately 1 hour of incubation, necessary to promote initial adhesion, fresh medium was added until a final volume of approximately 2 mL per well was reached.

The experimental groups included PCL-brushite composite discs doped with Zn^{2+} at 2%, 5%, and 10%. For each group, 2 discs were seeded. A control was also included, consisting of cells seeded directly onto the plastic surface of the well, without a disc, useful for verifying cell viability and proliferative capacity under standard conditions.

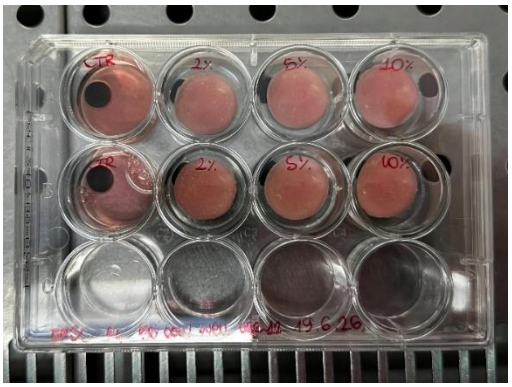

Figure 49: PCL-brushite composite discs placed inside a multiwell plate for the preliminary biological evaluation phase. The sterilized samples were inserted into the wells and subsequently used for the seeding of stem/mesenchymal cells derived from dental pulp.

The biological tests considered included cell viability/metabolism assays, such as the MTT assay, staining procedures for the analysis of cell adhesion and morphology, such as phalloidin staining, and possible evaluations of osteogenic differentiation by Alizarin Red staining. In the present work, these analyses are mentioned as part of the preliminary biological phase, whereas the detailed description of the results and cellular response is assigned to the thesis dedicated to the biological evaluation.

3 RESULTS

3.1 Preliminary mechanical compression testing of brushite cements

The preliminary mechanical compression tests were performed on cylindrical samples of pure brushite and brushite doped with Zn^{2+} at 2%, 5%, and 10%. The aim of this phase was to evaluate the mechanical behavior of the cements before their subsequent grinding and use as the ceramic phase within the PCL-brushite composites.

For each formulation, five valid tests were considered. From the stress-strain curves, the compressive elastic modulus (E_c), maximum stress (σ_M), and corresponding strain (ε_M) were obtained. Mean values and standard deviations are reported in Table 7.

Formulation	E_c (MPa)	σ_M (MPa)	ε_M (%)	d_o (mm)	A_o (mm²)	l_o (mm)
Pure brushite	637,59 ± 215,76	6,75 ± 2,25	2,21 ± 0,50	12,50 ± 0,00	122,72 ± 0,00	25,82 ± 0,60
Brushite-Zn^{2+} 2%	97,71 ± 35,02	0,94 ± 0,17	2,79 ± 0,89	12,50 ± 0,00	122,72 ± 0,00	25,68 ± 0,48
Brushite-Zn^{2+} 5%	71,96 ± 33,65	0,61 ± 0,31	3,20 ± 1,31	12,50 ± 0,00	122,72 ± 0,00	25,47 ± 0,86
Brushite-Zn^{2+} 10%	42,46 ± 20,79	0,81 ± 0,13	3,93 ± 0,34	12,50 ± 0,00	122,72 ± 0,00	23,00 ± 2,59

Table 7: Mechanical and dimensional parameters obtained from compression tests on pure brushite and Zn^{2+}-doped brushite cements. Values are reported as mean ± standard deviation. E_c: compressive elastic modulus; σ_M: maximum compressive stress; ε_M: strain corresponding to maximum stress; d_o: initial diameter; A_o: initial cross-sectional area; l_o: initial height of the sample.

Pure brushite, used as the control sample, showed the highest values of elastic modulus and maximum stress compared with all the other formulations analyzed. In particular, the mean elastic modulus was 637,59 MPa, while the mean maximum stress was 6,75 MPa. The stress-strain curves showed a progressive increase in stress up to the maximum value, followed by a more or less abrupt reduction in load, consistent with the brittle behavior expected for a calcium phosphate-based ceramic cement.

The zinc-doped formulations showed markedly lower values than the undoped control. The mean elastic modulus decreased to 97,71 MPa for brushite-Zn^{2+} 2%, to 71,96 MPa for brushite-Zn^{2+} 5%, and to 42,46 MPa for brushite-Zn^{2+} 10%. The mean maximum stress was also clearly lower than that of pure brushite, with values of 0,94 MPa, 0,61 MPa, and 0,81 MPa for the 2%, 5%, and 10% formulations, respectively.

At the same time, the doped samples showed higher mean strain values than pure brushite. The strain at maximum stress increased from 2,21% in the control sample to 2,79%, 3,20%, and 3,93% in the 2%, 5%, and 10% formulations, respectively. This

finding indicates that, although the doped cements showed lower stiffness and lower strength, they reached maximum stress at, on average, higher deformation values.

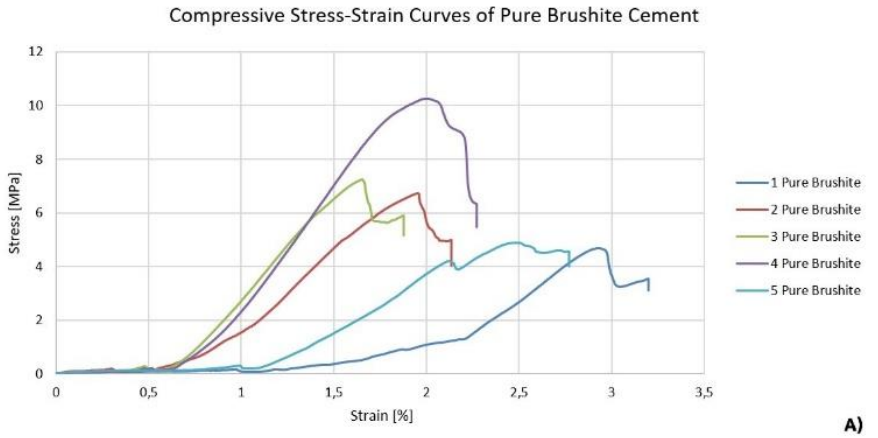

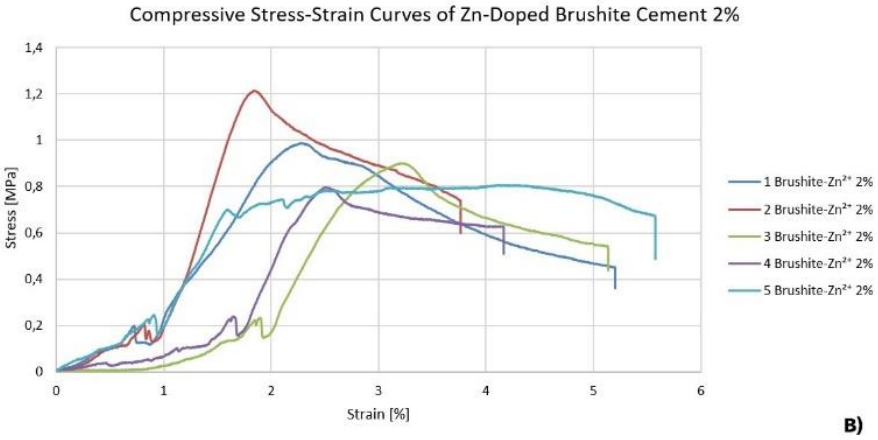

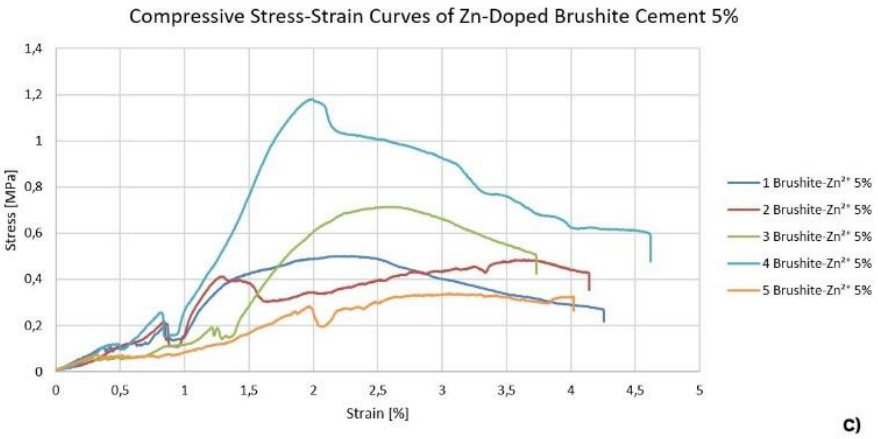

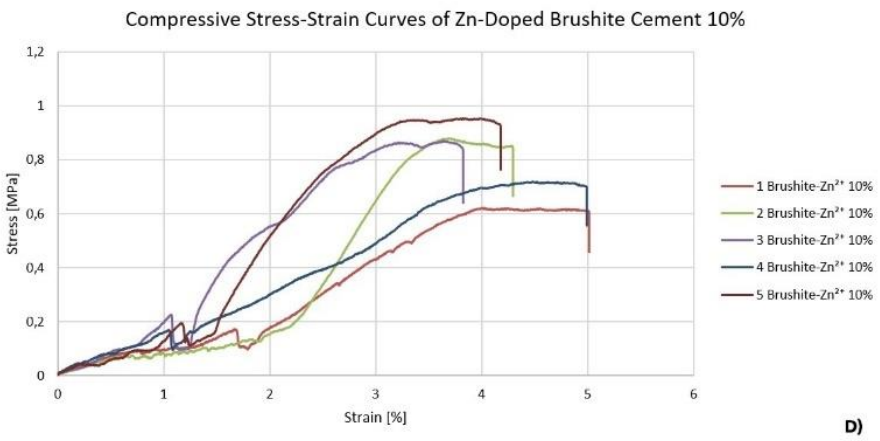

Figure 50: Stress-strain curves obtained from compression tests on pure brushite and Zn^{2+}-doped brushite cements. A) pure brushite; B) brushite-Zn^{2+} 2%; C) brushite-Zn^{2+} 5%; D) brushite-Zn^{2+} 10%. The curves show a reduction in maximum stress and elastic modulus in the doped samples compared with pure brushite.

Overall, the results of the compression tests indicate a marked reduction in the mechanical properties of the cements following Zn^{2+} doping. However, considering the preliminary nature of the tests and the variability observed, these data should be interpreted as indicative of a general trend rather than as a definitive evaluation of the mechanical performance of the material.

3.2 Characterization by X-ray diffraction

XRD analysis was performed on powder samples of pure brushite and brushite doped with Zn^{2+} at 2%, 5%, and 10%, with the aim of verifying the formation of the brushite phase and evaluating possible differences between the control sample and the doped formulations.

The diffractograms obtained are reported in Figure 51. In all the samples analyzed, well-defined peaks were present, indicating the presence of a crystalline phase. The main signals observed were approximately located in the 2θ regions between 20° and 35°, with additional lower-intensity peaks between 40° and 60°. In particular, peaks were observed at approximately 21°, 26–27°, 29–31°, 34–35°, 37°, 41–42°, and 50° 2θ.

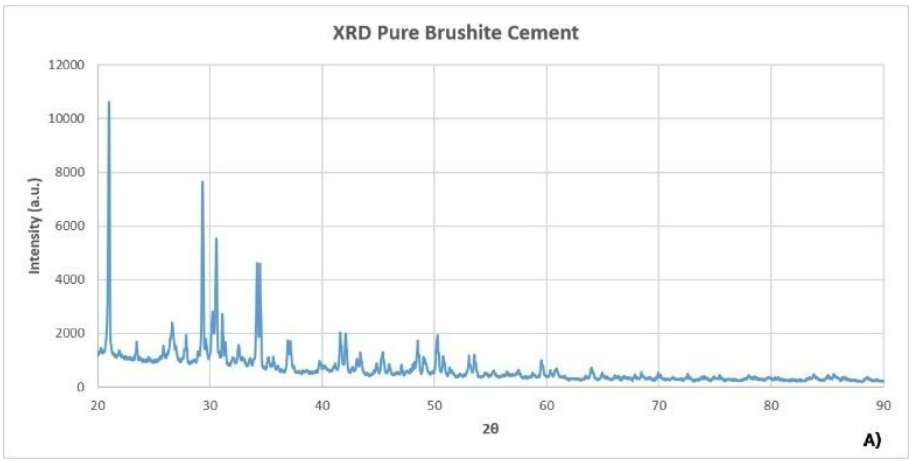

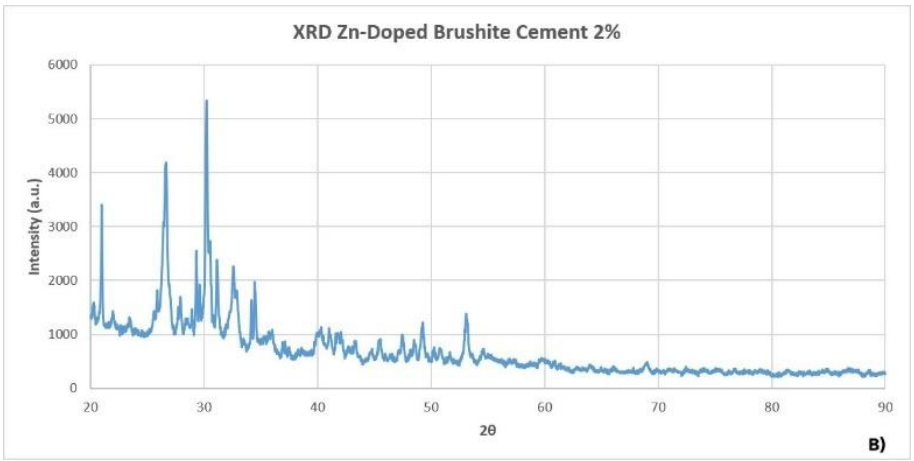

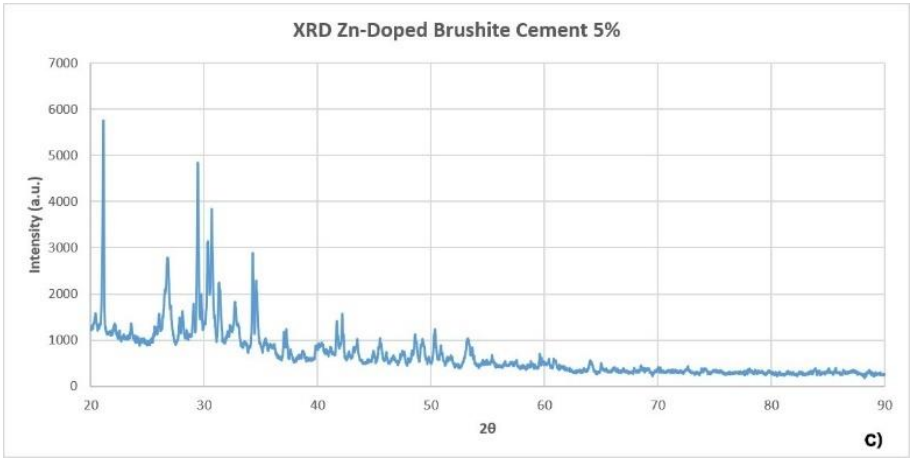

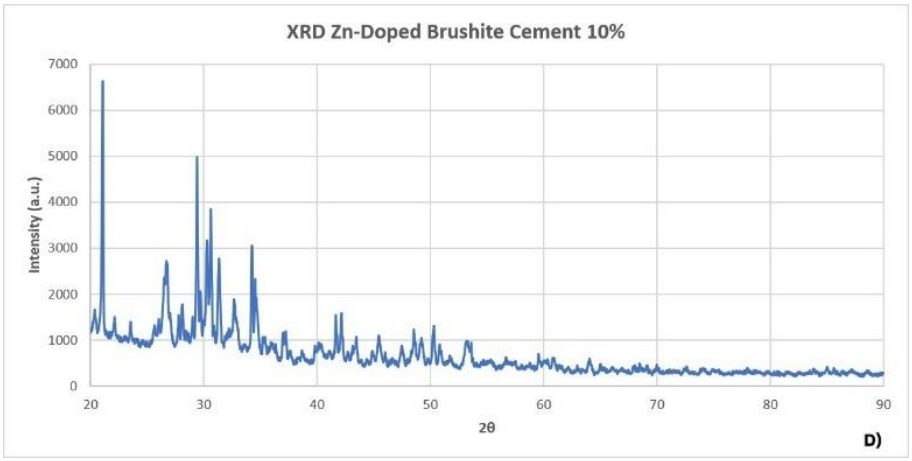

Figure 51: XRD diffractograms of pure brushite and Zn^{2+}-doped brushite samples. A) pure brushite; B) brushite-Zn^{2+} 2%; C) brushite-Zn^{2+} 5%; D) brushite-Zn^{2+} 10%. The diffractograms show the presence of crystalline peaks in the characteristic regions of brushite.

Pure brushite showed intense and clearly recognizable peaks, particularly in the regions around 21°, 29–31°, and 34° 2θ. The zinc-doped samples showed an overall similar profile, with peaks located in the same main regions. This result suggests that the predominant crystalline phase in the produced materials is compatible with brushite, or dicalcium phosphate dihydrate, $CaHPO_4 \cdot 2H_2O$.

In the brushite-Zn^{2+} 2% sample, a slightly different profile was observed compared with the other samples, with a different distribution of the relative peak intensities. This difference could be related to variations in crystallinity, preferential orientation of the crystals, powder particle size, or the presence of different amounts of residual phases. In the brushite-Zn^{2+} 5% and 10% samples, instead, the diffractometric profile appeared more similar to that of pure brushite, although with differences in relative intensities.

No systematic and progressive shift of the main peaks was observed with increasing nominal Zn^{2+} percentage. This finding suggests that, under the experimental conditions adopted, zinc doping did not produce macroscopic modifications of the crystalline structure that were easily detectable by simple qualitative comparison of the diffractograms.

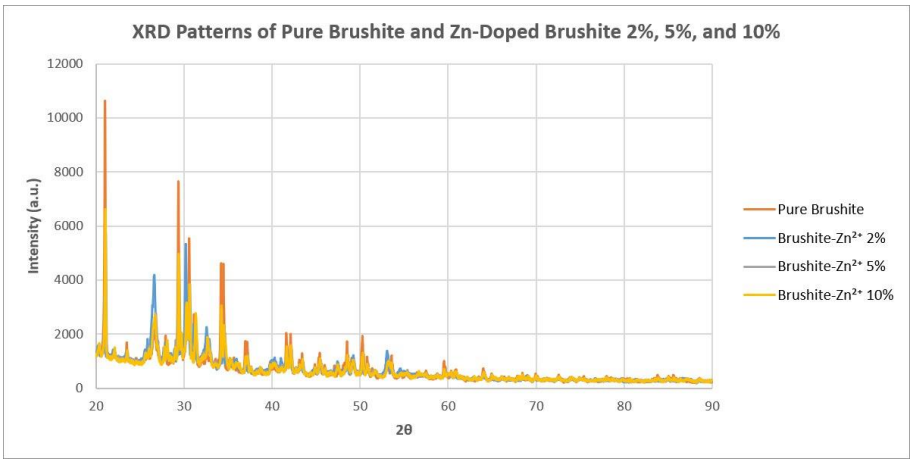

Figure 52: Comparison of XRD diffractograms of pure brushite and brushite-Zn^{2+} 2%, 5%, and 10% formulations. The profiles show the preservation of the main peaks attributable to the brushite phase.

Overall, XRD analysis confirms the presence of a crystalline phase compatible with brushite in all the produced samples. However, based on the acquired diffractograms alone, it is not possible to directly and quantitatively demonstrate the actual incorporation of Zn^{2+} into the brushite crystal lattice. For a more in-depth evaluation, complementary analyses such as Rietveld refinement, SEM-EDS, ICP-OES, or ion release analysis would be required.

3.3 Characterization by FT-IR spectroscopy

FT-IR analysis was performed on powder samples of pure brushite and brushite doped with Zn^{2+} at 2%, 5%, and 10%, with the aim of identifying the main functional groups present and comparing the spectral profile of the different formulations. The FT-IR spectra obtained are reported in Figure 53, while the offset-scale comparison among the four samples is shown in Figure 54.

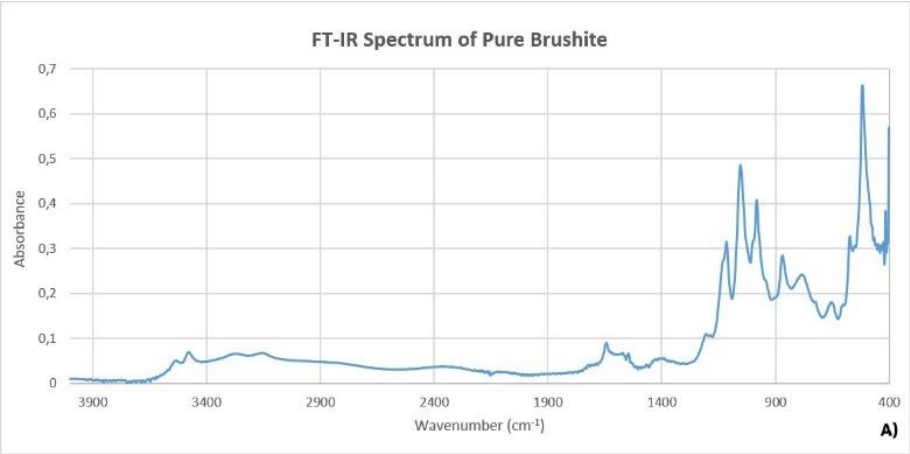

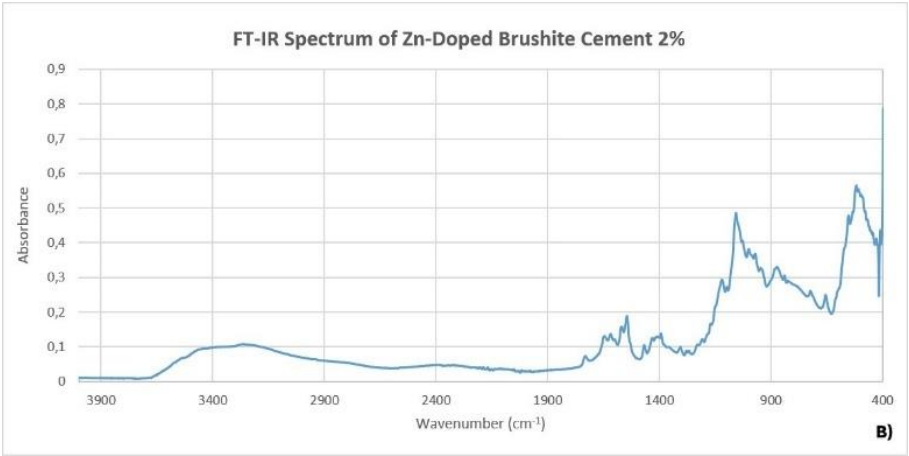

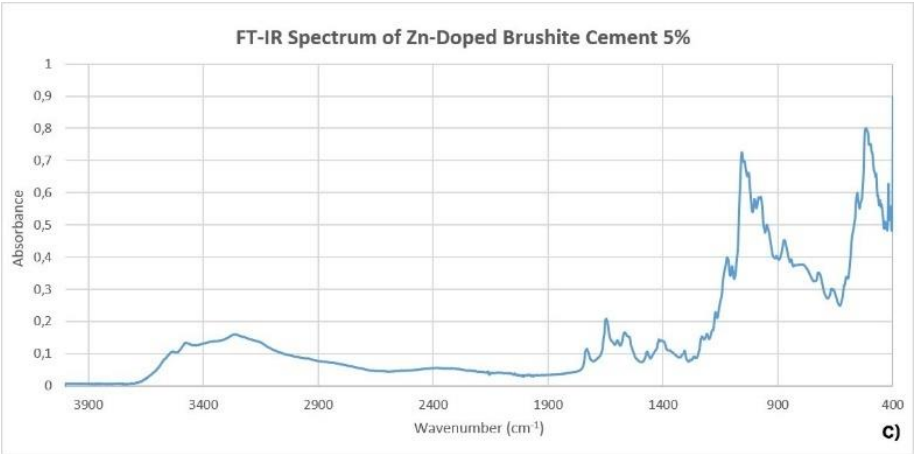

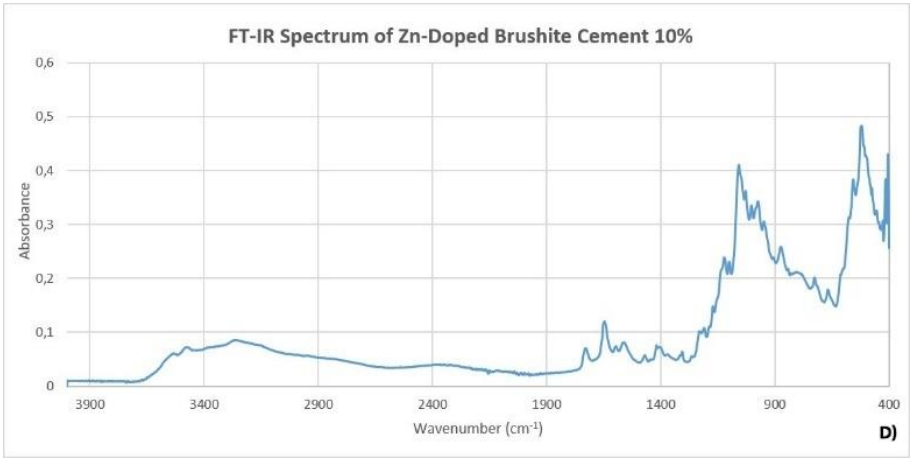

Figure 53: FT-IR spectra of pure brushite and Zn^{2+}-doped brushite samples. A) pure brushite; B) brushite-Zn^{2+} 2%; C) brushite-Zn^{2+} 5%; D) brushite-Zn^{2+} 10%.

Starting from the numerical data obtained from the spectra, the main absorption bands were identified and are reported in Table 8. The vibrational assignments were made based on the characteristic regions reported in the literature for brushite and hydrated calcium phosphates. [66–69]

Region/vibrational assignment	Pure brushite	Brushite-Zn^{2+} 2%	Brushite-Zn^{2+} 5%	Brushite-Zn^{2+} 10%
O–H stretching of structural/adsorbed water	3479; 3157	3402; 3265	3475; 3261	3477; 3261
H–O–H bending of water	1645	1618; 1645	1645	1645
P–O stretching of HPO_4^{2-}/PO_4^{3-} groups	1117; 1055	1121; 1057	1119; 1055	1121; 1057
P–O / HPO_4^{2-} vibrations	984; 955	999; 945	978; 945	974; 945
P–O(H) / HPO_4^{2-} band	872	874	872	872
Bending of phosphate/hydrogen phosphate groups	787; 656; 573; 519	810; 656; 554; 519	798; 663; 554; 515	804; 665; 554; 521

Table 8: Main FT-IR bands observed in pure brushite and Zn^{2+}-doped brushite samples. Values are reported in cm^{-1} and were rounded to the nearest unit. The vibrational assignments should be considered qualitative.

All the samples analyzed showed an overall profile compatible with a brushite-like calcium phosphate. In the high-wavenumber region, approximately between 3600 and 3100 cm^{-1}, bands attributable to O–H stretching vibrations of structural and/or adsorbed water molecules were present. In pure brushite, maxima were observed at approximately 3479 and 3157 cm^{-1}, whereas in the doped samples bands were recognizable in the same region, with main maxima between approximately 3261 and 3477 cm^{-1}.

In the region around 1650–1600 cm^{-1}, signals attributable to H–O–H bending vibrations of water were observed. Pure brushite showed a maximum at approximately 1645 cm^{-1}; similar values were also observed in the brushite-Zn^{2+} 5% and 10% samples, whereas in the brushite-Zn^{2+} 2% sample, signals were detected in the 1618–1645 cm^{-1} region.

The most intense bands were located in the region between approximately 1200 and 900 cm^{-1}, mainly attributable to stretching vibrations of phosphate PO_4^{3-} and hydrogen phosphate HPO_4^{2-} groups. In particular, maxima around 1117–1121 cm^{-1} and 1055–1057 cm^{-1} were identified in all samples. Additional bands were present in the 1000–945 cm^{-1} region, which is also attributable to P–O vibrations of phosphate/hydrogen phosphate groups.

A characteristic band was also observed around 872–874 cm^{-1}, attributable to P–O(H) vibrations associated with HPO_4^{2-} hydrogen phosphate groups. In the lower-wavenumber region, between approximately 800 and 500 cm^{-1}, further bands attributable to bending vibrations of phosphate/hydrogen phosphate groups were observed, with main maxima around 656–665 cm^{-1}, 553–573 cm^{-1}, and 515–521 cm^{-1}.

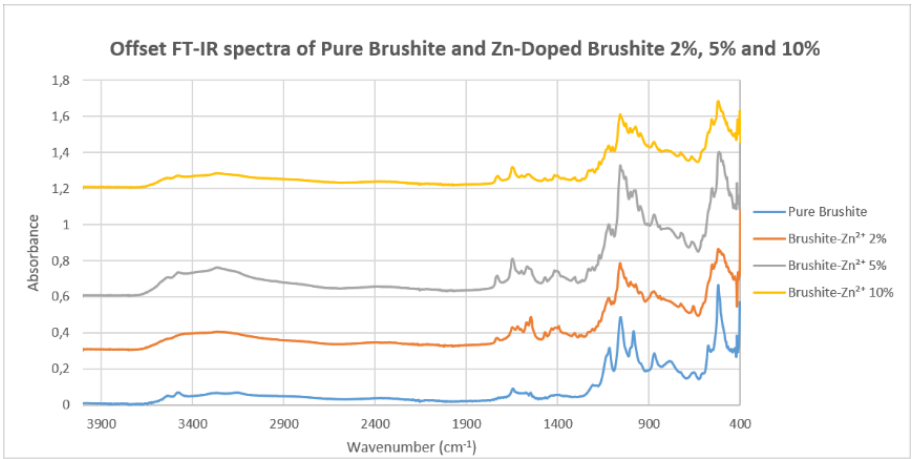

Figure 54: Offset-scale comparison of FT-IR spectra of pure brushite and brushite-Zn^{2+} 2%, 5%, and 10% formulations. The vertical offset representation allows better visualization of the position and shape of the main characteristic bands.

The comparison among the spectra shows that the main characteristic bands of brushite are present in all the analyzed formulations. No new bands clearly attributable to zinc-containing species were observed.

3.4 Processability of the PCL/brushite-Zn^{2+} composite and fabrication of printed samples

In addition to the characterization of the brushite cements, a further result of the present work was the transformation of Zn^{2+}-doped brushite into a composite processable by extrusion and 3D printing. Brushite-Zn^{2+} powders at 2%, 5%, and 10% were incorporated into a polycaprolactone matrix by melt blending, maintaining a weight ratio of 80% PCL and 20% doped brushite.

The composite material obtained was subsequently transformed into pellets and used for filament production by extrusion. This phase required several preliminary trials and optimization of the processing parameters, particularly temperature, extrusion speed, and material cooling conditions. Despite the difficulties related to the experimental nature of the composite, it was possible to obtain filaments suitable for the subsequent 3D printing trials.

The 3D printing phase required further hardware and software optimization, including the choice of the printer, firmware management, controlled filament loading, the use of a 1 mm nozzle, and the definition of the slicing parameters. The samples were printed using an Anycubic Kobra 3, with PrusaSlicer for G-code generation and the Fluidd interface for machine control.

For each Zn^{2+} doping percentage of brushite, namely 2%, 5%, and 10%, 10 discs intended for preliminary biological evaluation and 5 rectangular specimens intended for flexural mechanical testing were produced. Overall, 30 discs and 15 rectangular specimens were therefore fabricated. At the end of printing, the samples were macroscopically evaluated in terms of integrity, geometrical regularity, and continuity of deposition.

Overall, this phase demonstrated the possibility of transforming Zn^{2+}-doped brushite into a PCL/brushite composite processable by extrusion and 3D printing. This result represents a relevant step in the experimental workflow, as it allows the transition from the initial cement phase to three-dimensional samples with controlled geometry, intended for subsequent mechanical and biological evaluations.

3.5 Flexural mechanical testing of PCL/brushite-Zn^{2+} composites

Three-point bending mechanical tests were performed on the rectangular specimens 3D printed in the three PCL/brushite-Zn^{2+} composite formulations at 2%, 5%, and 10%.

For each formulation, five tests were performed. From the stress-strain curves, the flexural elastic modulus (E_f), maximum flexural stress (σ_{fM}), and strain corresponding to the maximum stress (ε_{fM}) were obtained. Mean values and standard deviations are reported in Table 9.

Formulation	E_f (MPa)	σ_{fM} (MPa)	ε_{fM} (%)	h (mm)	b (mm)	A_o (mm^2)
PCL/brushite-Zn^{2+} 2%	526,43 ± 40,59	25,90 ± 1,73	7,70 ± 0,28	2,84 ± 0,05	8,44 ± 0,05	23,97 ± 0,51
PCL/brushite-Zn^{2+} 5%	522,59 ± 54,95	26,95 ± 1,43	8,20 ± 0,43	3,02 ± 0,13	9,18 ± 0,11	27,73 ± 1,51
PCL/brushite-Zn^{2+} 10%	496,30 ± 50,99	25,41 ± 2,00	8,20 ± 0,27	3,00 ± 0,07	9,22 ± 0,11	27,66 ± 0,74

Table 9: Mechanical and dimensional parameters obtained from flexural tests on PCL/brushite-Zn^{2+} composites. Values are reported as mean ± standard deviation. E_f: flexural elastic modulus; σ_{fM}: maximum flexural stress; ε_{fM}: strain corresponding to maximum stress; h: sample thickness; b: sample width; A_0: cross-sectional area.

The stress-strain curves of the composites showed a regular and reproducible trend. In all samples, stress progressively increased with strain until reaching a maximum value, followed by a slight reduction in load or by a plateau-like trend. This behavior differs from that observed in the cements subjected to compression and is compatible with the contribution of the PCL polymeric matrix, which provides the composite material with greater deformation capacity. The curves obtained from the flexural tests are reported in Figure 55.

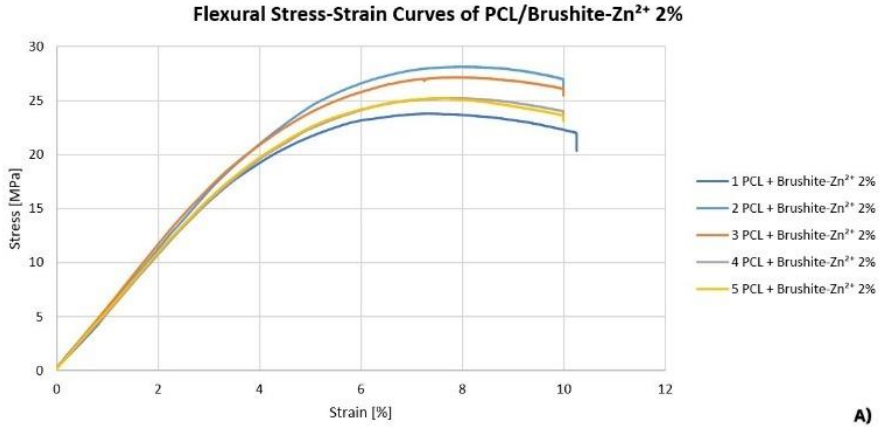

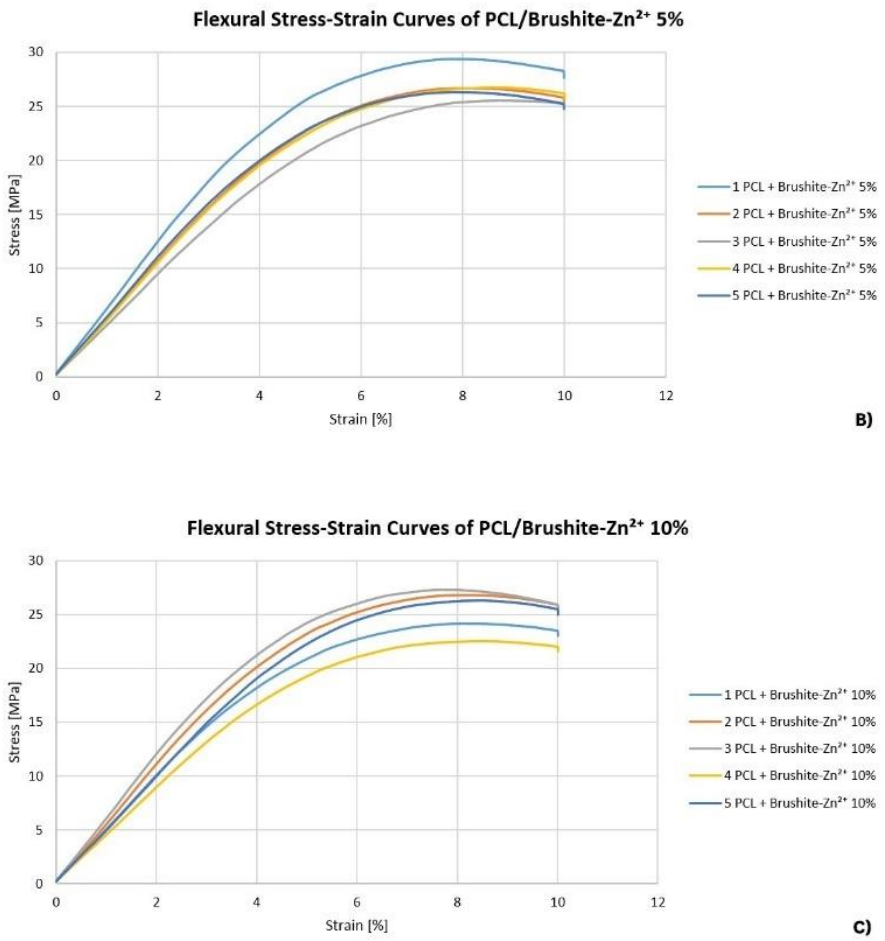

Figure 55: Stress-strain curves obtained from flexural tests on PCL/brushite-Zn^{2+} composites. A) PCL/brushite-Zn^{2+} 2%; B) PCL/brushite-Zn^{2+} 5%; C) PCL/brushite-Zn^{2+} 10%.

The mean flexural modulus was 526,43 MPa for the composite containing brushite-Zn^{2+} 2%, 522,59 MPa for the composite containing brushite-Zn^{2+} 5%, and 496,30 MPa for the composite containing brushite-Zn^{2+} 10%. The differences among the three formulations were limited and did not show a clear dose-dependent trend.

Regarding maximum flexural stress, the highest value was observed in the PCL/brushite-Zn^{2+} 5% group, with a mean value of 26,95 MPa. The PCL/brushite-Zn^{2+} 2% and PCL/brushite-Zn^{2+} 10% samples showed mean values of 25,90 MPa and 25,41 MPa, respectively. In this case as well, the differences among the groups were limited.

The strain at maximum stress was 7,70% for the 2% composite and 8,20% for the 5% and 10% composites. These values indicate that the printed samples maintained good deformation capacity before reaching the maximum load.

Overall, the flexural tests showed that increasing the nominal Zn^{2+} percentage in the brushite phase did not cause a marked worsening of the mechanical properties of the

PCL/brushite composites. Indeed, the flexural performance was similar among the three formulations, suggesting that the mechanical response of the printed samples was strongly influenced by the PCL polymeric matrix and sample geometry, in addition to the incorporated ceramic phase.

4 DISCUSSION

4.1 General interpretation of the results

The aim of the present study was the development and preliminary characterization of composite materials based on zinc-doped calcium phosphates and PCL, with a view to their possible future application in the fabrication of customized three-dimensional scaffolds for bone regeneration. In particular, brushite formulations doped with Zn^{2+} at 2%, 5%, and 10% were prepared and subsequently characterized from a mechanical and chemical-structural point of view. Part of the doped brushite powder was then used for the preparation of PCL/brushite composites, processed by extrusion and 3D printing.

Brushite, or dicalcium phosphate dihydrate, $CaHPO_4 \cdot 2H_2O$, is a calcium phosphate of interest in the biomaterials field due to its greater solubility compared with apatitic phases and its potential resorbability in a physiological environment. Calcium phosphates are widely studied as bone substitutes, cements, scaffolds, and drug delivery materials because of their similarity to the mineral component of bone and their biocompatibility and osteoconductivity. [70–73] In this context, brushite represents a particularly interesting phase among calcium phosphates used for bone repair applications. [35,36]

The introduction of bioactive metal ions, including Zn^{2+}, Ag^{+}, Cu^{2+}, Sr^{2+}, and Mg^{2+}, has been proposed in the literature as a strategy to modulate the chemical, biological, and antimicrobial properties of calcium phosphates. In particular, Zn^{2+} is considered of interest for bone metabolism, as it may influence osteoblast proliferation and differentiation and also possesses antimicrobial properties. [41–46] However, its effect on the physicomechanical properties and microstructure of phosphate cements can be complex and may depend on the formulation, ionic content, and synthesis conditions.

Overall, the results obtained show that Zn^{2+} doping did not prevent the formation of a phase compatible with brushite, as evidenced by XRD and FT-IR analyses. However, the mechanical properties of the doped cements showed a marked reduction compared with pure brushite. Conversely, once incorporated into the PCL polymeric matrix, the doped brushite phase allowed printed composites to be obtained with relatively similar flexural properties among the different doping percentages.

4.2 Effect of Zn^{2+} doping on the mechanical properties of the cements

The compression tests showed a marked reduction in mechanical properties in the Zn^{2+}-doped cements compared with pure brushite. In particular, the mean elastic modulus decreased from 637.59 MPa in pure brushite to 97.71 MPa, 71.96 MPa, and 42.46 MPa for the 2%, 5%, and 10% formulations, respectively. The maximum compressive stress also decreased markedly, from 6.75 MPa in pure brushite to values below 1 MPa in the doped samples.

This trend suggests that, under the experimental conditions adopted, the introduction of zinc negatively influenced the mechanical strength of the brushite cement. This effect could be related to a modification of the setting kinetics, brushite crystallization, internal porosity, or degree of conversion of the initial reagents. In brushite cements, the setting reaction is generally described as an acid-base reaction between β-TCP and MCPM, with brushite formation as the main hydrated product. [74] The growth rate of brushite crystals is high, which is why setting retarders are often used to control cement workability. [75–77]

The effect of metal ions on the hydration reaction of brushite cements has also been discussed in studies on β-TCP doped with other divalent ions. For example, in the case of Cu^{2+}, it has been observed that β-TCP doping may lead to a significant slowing of the hydration reaction and a modification of hydrated phase formation. [39,78,79] Although the present work concerns Zn^{2+} and not Cu^{2+}, these data suggest that the presence of metal ions in the β-TCP precursor may influence the setting kinetics and final microstructure of the cement.

The reduction in compressive strength could also be related to the presence of residual β-TCP or incompletely reacted phases. In the literature, residual β-TCP particles have been reported to act as fillers and contribute to stabilization of the cement microstructure; however, a non-optimal distribution of particles or an excessive amount of inclusions may generate stress concentration areas and promote crack propagation. [80–82] In the present study, the absence of microstructural analyses by SEM does not allow this hypothesis to be directly verified.

A further element to consider is data variability, which was particularly evident in the compression tests. The coefficients of variation of the elastic modulus and maximum stress were high, especially in the doped groups. This variability could depend on

macroscopic defects in the cylinders, air bubbles, microfractures, differences in paste compaction inside the syringes, or inhomogeneity in the distribution of zinc and reactive phases. For this reason, the mechanical data obtained for the cements should be interpreted as preliminary.

4.3 Interpretation of XRD analyses

The XRD diffractograms showed, in all samples, the presence of crystalline peaks compatible with brushite. The preservation of the main peaks in the doped samples indicates that the introduction of Zn^{2+} did not prevent the formation of the brushite phase. This finding is consistent with the literature, in which brushite is identified as a characteristic crystalline phase of cements obtained from the reaction between β-TCP and MCPM. [74]

No systematic shift of the main peaks was observed in the analyzed samples with increasing nominal Zn^{2+} percentage. This aspect is relevant because a regular shift of XRD peaks could suggest modifications of lattice parameters due to ionic substitution. However, the absence of an evident shift does not exclude the presence of zinc in the material. Zn^{2+} could be present in amounts below the detection limit of the technique, mainly localized in amorphous or poorly crystalline phases, associated with residual doped β-TCP, or distributed in a manner insufficient to produce a measurable variation in the brushite peaks.

In studies on cements based on zinc-doped β-TCP, it has been reported that zinc may preferentially occupy the β-TCP lattice rather than that of the final cementitious phase. In particular, in monetite cements obtained from Znβ-TCP, XRD analysis revealed the presence of unreacted Znβ-TCP and monetite, suggesting that zinc could remain preferentially associated with the β-TCP precursor. [82] Although the final phase in the present work is brushite and not monetite, this finding suggests caution in directly attributing zinc to the brushite lattice on the basis of diffractograms alone.

Therefore, XRD analysis supports the formation of brushite as the main phase, but does not allow the localization of zinc to be established with certainty. To confirm doping and distinguish between zinc incorporated into the lattice, zinc associated with residual phases, or zinc present in amorphous form, complementary analyses would be required. In particular, SEM-EDS would allow evaluation of the elemental distribution of zinc, whereas ICP-OES or ICP-MS would allow quantification of its total content and release into solution. Possible Rietveld refinement could also allow a more accurate evaluation of the crystalline phases present.

4.4 Interpretation of FT-IR spectra

The FT-IR spectra confirmed the presence of the main functional groups characteristic of brushite. The bands observed in the 3600–3000 cm^{-1} region are attributable to O-H stretching of structural and/or adsorbed water, while the band around 1650–1600 cm^{-1} is attributable to bending of water molecules. The bands between approximately 1200 and 900 cm^{-1} are attributable to vibrations of phosphate and hydrogen phosphate groups, whereas those in the 650–500 cm^{-1} region are associated with bending vibrations of phosphate/hydrogen phosphate groups. [66,83–88]

The comparison between pure brushite and doped samples showed general preservation of the spectral profile, confirming that Zn^{2+} doping did not substantially alter the chemical nature of the material. However, some variations were observed in the position and relative intensity of specific bands, especially in the regions associated with structural water and phosphate/hydrogen phosphate groups.

In the literature, in metal-doped brushite samples, variations in the position and intensity of FT-IR bands have been interpreted as possible indications of modifications of the local chemical environment of functional groups due to the presence of doping ions. [89–92] In particular, the introduction of metal ions may alter hydrogen bonding interactions and the local organization of water molecules and phosphate/hydrogen phosphate groups. However, these variations do not represent direct and quantitative proof of zinc incorporation into the crystal lattice.

FT-IR analysis can therefore be considered complementary to XRD: both techniques support the formation of a material compatible with brushite, but neither of them alone allows Zn^{2+} to be localized with certainty. Furthermore, the intensity of FT-IR bands can be influenced by experimental factors such as sample amount, powder particle size, contact with the support, and baseline correction. For this reason, the intensity differences observed among the samples should be interpreted with caution and not as direct quantitative data.

4.5 Processability of the composite and fabrication by 3D printing

A further relevant aspect of the present work concerns the possibility of transforming Zn^{2+}-doped brushite into a composite material actually processable by extrusion and 3D printing. Although the brushite cement phase alone is of interest due to its bioactive and bioresorbable nature, it does not possess adequate workability characteristics to be directly used in fused deposition additive manufacturing processes. The introduction of PCL therefore played a fundamental role in providing the material with greater continuity, deformability, and processability.

In the present study, Zn^{2+}-doped brushite powders were incorporated into a PCL matrix by melt blending, with an 80/20 weight ratio. The composite thus obtained was subsequently transformed into pellets, extruded in the form of filament, and finally used for 3D printing of samples with controlled geometries. This result represents an important step, as it demonstrates the feasibility of an integrated experimental pathway allowing transition from a calcium phosphate-based cement to a printable composite material.

The filament extrusion phase and subsequent 3D printing, however, highlighted some critical issues related to the experimental nature of the material. In particular, the PCL/brushite-Zn^{2+} composite required optimization of processing parameters, including temperature, extrusion speed, cooling management, nozzle diameter, and filament loading method. These difficulties may be attributed to the presence of the ceramic phase dispersed within the polymeric matrix, possible filament irregularity, and the different thermomechanical response of the composite compared with a commercial polymeric filament.

Despite these critical issues, it was possible to obtain three-dimensionally printed samples in the three doping formulations considered. In particular, rectangular specimens intended for flexural mechanical testing and discs intended for preliminary biological evaluations were produced. This finding supports the potential applicability of the PCL/brushite-Zn^{2+} composite as a starting material for future additive manufacturing strategies of customized scaffolds.

Indeed, 3D printing represents a technology of particular interest in bone tissue engineering, as it allows the fabrication of structures with controlled geometry, potentially adaptable to the anatomical defect and designed to guide tissue

regeneration. Scaffold microarchitecture, pore size, interconnection, and spatial distribution of the material can influence cell colonization, nutrient diffusion, and new tissue formation. [63,93] In the present work, complex porous scaffolds were not yet produced, but the possibility of printing discs and rectangular specimens represents a first step toward the development of more advanced geometries.

Before possible application in the regenerative field, it will be necessary to further optimize filament regularity, deposition quality, printing reproducibility, and the final microarchitecture of the scaffolds. It will also be important to evaluate the effect of printing parameters on the distribution of the ceramic phase, porosity, mechanical properties, and cellular response.

4.6 Mechanical behavior of PCL/brushite-Zn^{2+} composites

The flexural tests on 3D-printed PCL/brushite-Zn^{2+} composites provided results different from those obtained in compression tests on the isolated cements. While the doped cements showed a marked reduction in mechanical properties compared with pure brushite, the PCL/brushite-Zn^{2+} composites maintained relatively similar values of flexural modulus and maximum stress among the three doping percentages.

The mean flexural modulus ranged between approximately 496 and 526 MPa, while the maximum flexural stress remained around 25–27 MPa. The PCL/brushite-Zn^{2+} 5% formulation showed the highest mean maximum stress value, equal to 26.95 MPa, but the difference compared with the 2% and 10% formulations was limited. Therefore, no clear dose-dependent effect of the nominal Zn^{2+} percentage on the flexural mechanical properties of the composite emerged.

This result suggests that, in the printed samples, the mechanical response is mainly dominated by the PCL polymeric matrix and by specimen geometry, rather than by the mechanical properties of the isolated brushite cement. The ceramic phase, incorporated at 20 wt%, may contribute to the bioactivity and functionalization of the composite, while PCL provides structural continuity, greater deformability, and improved handling of the material.

The flexural curves also showed greater reproducibility than the compression curves of the cements. This finding suggests that the melt blending, extrusion, and 3D printing process produced samples that were relatively homogeneous from a macroscopic point of view. However, it should be considered that the mechanical response of printed composites may depend on numerous factors, including filament orientation, interlayer adhesion, distribution of the ceramic phase, presence of agglomerates, printing parameters, and degree of crystallinity of PCL.

To interpret these results more completely, it would also be useful to include a control group consisting of printed PCL alone and a PCL/pure brushite composite. These comparisons would allow the effect of the ceramic phase to be better distinguished from the specific effect of Zn^{2+} doping.

4.7 Limitations of the study

The present work represents a preliminary characterization of the materials produced and has some limitations that should be considered when interpreting the results.

First, the number of samples analyzed was limited, and no inferential statistical analyses were performed. The mechanical data should therefore be considered descriptive and indicative of a trend. Second, the variability observed in the compression tests suggests the need to further optimize the preparation of the cylinders and to more accurately control parameters such as porosity, paste homogeneity, and the presence of internal defects. Third, XRD and FT-IR analyses confirm the formation of a phase compatible with brushite, but they do not allow Zn^{2+} to be localized with certainty or its incorporation to be quantified. For this purpose, complementary analyses such as SEM-EDS, ICP-OES/ICP-MS, XPS, or ion release tests would be necessary.

A further limitation concerns the absence, at this stage, of a microstructural characterization of the printed composites. SEM analysis could allow evaluation of the distribution of brushite powder within the PCL, the possible presence of agglomerates, the quality of the polymer-ceramic interface, and the surface morphology of the printed samples.

Finally, although mechanical and chemical-structural properties are fundamental, they are not sufficient to draw definitive conclusions on the suitability of the material for bone regeneration applications. These results will need to be integrated with preliminary biological tests, such as evaluations of biocompatibility, cell adhesion, proliferation, cell viability, and possible osteogenic response. This aspect is particularly relevant for materials containing Zn^{2+}, since the biological response may depend not only on the presence of zinc, but also on its concentration, release rate, and interaction with the cellular matrix. [82,94–97]

4.8 Future perspectives

The results obtained suggest that PCL/brushite-Zn^{2+} composites represent a promising platform for further developments in the field of additive manufacturing of biomaterials for bone regeneration. The possibility of combining a polymeric matrix processable by 3D printing with a zinc-doped brushite ceramic phase could, in perspective, allow the fabrication of customized scaffolds with tunable mechanical, chemical, and biological properties.

Future experimental activities should focus on several aspects. First, it will be necessary to optimize the formulation of the doped brushite cements in order to improve the mechanical properties of the ceramic phase and reduce sample variability. Second, it will be important to characterize the distribution of zinc and its possible release in aqueous or biological environments. Third, it will be useful to compare PCL/brushite-Zn^{2+} composites with appropriate controls, such as pure PCL, PCL/pure brushite, and, possibly, formulations with different percentages of ceramic phase.

A further development will concern the biological evaluation of the printed materials. Cell viability test, adhesion, proliferation, and osteogenic differentiation tests will make it possible to verify whether the introduction of Zn^{2+} confers actual biological advantages compared with undoped brushite. Only the integration of mechanical, chemical-structural, and biological results will allow a more complete evaluation of the potential of the material for bone regeneration applications.

5 CONCLUSIONS

The aim of the present thesis was the development and preliminary characterization of composite materials based on Zn^{2+}-doped brushite and polycaprolactone, with the objective of evaluating their potential processability by extrusion and 3D printing techniques for future applications in the field of bone regeneration.

First, Zn^{2+}-doped brushite cements were obtained at three different nominal percentages, equal to 2%, 5%, and 10%, using zinc-doped β-TCP as the precursor for the cementitious reaction. Pure brushite was instead prepared as a control material for the preliminary mechanical compression tests and chemical-structural analyses.

The compression tests highlighted a marked reduction in mechanical properties in the doped cements compared with pure brushite. In particular, both the elastic modulus and the maximum compressive stress were markedly lower in the samples containing Zn^{2+}. This finding suggests that, under the experimental conditions adopted, zinc doping negatively influenced the mechanical strength of the cementitious phase, probably by interfering with the setting reaction, crystallization, or final microstructure of the cement.

XRD and FT-IR analyses confirmed the presence of features compatible with brushite formation in the produced samples. The diffractograms showed crystalline peaks attributable to a calcium phosphate-based phase, while the FT-IR spectra showed bands associated with phosphate groups, hydrogen phosphate groups, and structural water, consistent with the chemical nature of brushite. However, based on XRD and FT-IR analyses alone, it was not possible to establish with certainty the localization of Zn^{2+} within the material or to definitively confirm its incorporation into the brushite crystal lattice.

A relevant result of this work was the possibility of incorporating Zn^{2+}-doped brushite into a PCL polymeric matrix, obtaining PCL/brushite-Zn^{2+} composites with an 80/20 weight ratio. The composite was subsequently transformed into pellets, extruded in the form of filament, and used for the fabrication, by 3D printing, of samples with controlled geometry. Despite the experimental difficulties related to filament production and printing of a non-commercial composite material, it was possible to obtain discs intended for preliminary biological evaluation and rectangular specimens intended for flexural mechanical testing.

The flexural tests performed on the printed composites showed a more regular and reproducible mechanical behavior compared with the brushite cements tested in compression. The three formulations containing brushite-Zn^{2+} at 2%, 5%, and 10% showed relatively similar mean values of flexural elastic modulus and maximum flexural stress, without a clear monotonic trend associated with the increase in doping percentage. This suggests that, in the printed composites, the mechanical behavior was mainly dominated by the PCL polymeric matrix and by the quality of the printing process, rather than by the different nominal percentage of zinc present in the ceramic phase.

Overall, the results obtained demonstrate the feasibility of an experimental pathway that allows the transition from a Zn^{2+}-doped brushite-based cement to a PCL/brushite composite processable by extrusion and 3D printing. This represents a first step toward the development of bioactive and potentially customizable composite materials for future applications in bone regeneration.

However, the study should be considered preliminary. Further investigations will be necessary to optimize the cement formulations, improve the mechanical properties of the brushite phase, clarify the actual distribution of Zn^{2+}, evaluate ion release, analyze the microstructure of the composites, and further investigate the biological response of the printed samples. In particular, future analyses by SEM-EDS, degradation tests, zinc release assays, and more extensive biological evaluations will be essential to understand the real application potential of the PCL/brushite-Zn^{2+} composites developed in the present work.

In conclusion, this thesis made it possible to develop and preliminarily characterize a composite material based on PCL and zinc-doped brushite, demonstrating the possibility of transforming it into filament and using it for 3D printing of experimental samples. Although further optimization is required, this approach represents a promising strategy for the future fabrication of customized, bioresorbable, and bioactive scaffolds intended for the regeneration of bone defects.

References:

[1] Schroeder HE. Handbook of microscopic anatomy. Vol. 5. The periodontium. Berlin: Springer-Verlag, 1986: 12± 323

[2] Bronner-Fraser M. Origins and developmental potential of the neural crest. Exp Cell Res 1995: 218: 405±417

[3] Cho MI, Garant PR. Development and general structure of the periodontium. Periodontol 2000. 2000 Oct;24:9-27. Doi: 10.1034/j.1600-0757.2000.2240102.x. PMID: 11276876.

[4] Tallgren, A. The continuing reduction of the residual alveolar ridges in complete denture wearers: a mixed longitudinal study covering 25 years. Journal of Prosthetic Dentistry 1972; 27, 120–132.

[5].Nadir M. Maraldi, Carlo Tacchetti, “Istologia Medica” Edi-Ermes

[6].A.Mjor-O.Fejerskov, “Embriologia e Istologia del cavo orale” Edi-Ermes

[7].Adamo S., Siracusa G., Carinci P., Stefanini M., Molinaro M., Ziparo E. Istologia di V. Monesi. Piccin.

[8] Omi M, Mishina Y. Roles of osteoclasts in alveolar bone remodeling. Genesis. 2022 Sep;60(8-9):e23490. doi: 10.1002/dvg.23490. Epub 2022 Jun 27. PMID: 35757898; PMCID: PMC9786271.

[9] Schroeder HE. Oral structural biology. New York: Time Medical Publishers, 1991.

[10] Luciano Fonzie, “Anatomia Funzionale e Clinica dello Splancno-Cranio”, Edi-Ermes.

[11] Araújo M.G., Lindhe J. Dimensional ridge alterations following tooth extraction. An experimental study in dog. J Clin Periodontol. 2005;32:212-218.

[12] Ten Cate A, Mills C, Solomon G. The development of the periodontium. A transplantation and autoradiographic study. Anat Rec 1971: 170: 365±380.

[13] Ten Cate AR, Mills C. The development of the periodontium: the origin of alveolar bone. Anat Rec 1972: 170: 365± 380.

[14] Cahill DR. Eruption pathway formation in the presence of experimental tooth impaction in puppies. Anat Rec 1969: 164: 67±78.

[15] Marks SC, Cielinski MJ, Sundquist K, Wise GE, Gorski JP. The role of bone resorption in tooth eruption. In: Davidovitch Z, ed. Proceedings of the International Conference on Biological Mechanisms of Tooth Eruption, Resorption and Replacement by Implants. Birmingham, AL: EBSCO Press, 1994: 483±488.

[16] Sakakura Y, Yajima T, Tsuruga E. Confocal laser scanning microscopic study of tartrate-resistant acid phosphatasepositive cells in the dental follicle during early morphogenesis of mouse embryonic molar teeth. Arch Oral Biol 1998: 43: 353±360.

[17] Wise G, Fan W. Changes in the tartrate-resistant acid phosphatase cell population in dental follicles and bony crypts of rat molars during tooth eruption. J Dent Res 1989: 68: 150±156.

[18] Wise GE. The biology of tooth eruption. J Dent Res 1998: 77: 1576±1579.

[19] Wise GE, Lin F. The molecular biology of initiation of tooth eruption. J Dent Res 1995: 74: 303±306.

[20] Wise GE, Lin F, Zhao L. Immunolocalization of interleukin-1b in rat mandibular molars and its enhancement after in vivo injection of epidermal growth factor. Cell Tissue Res 1995: 280: 21±26.

[21] Wise GE, Lin F, Zhao L. Transcription and translation of CSF-1 in the dental follicle. J Dent Res 1995: 74: 1551± 1557.

[22] Shafizadeh M, Tehranchi A, Shirvani A, Motamedian SR. Alveolar bone thickness overlying healthy maxillary and mandibular teeth: A systematic review and meta-analysis. Int Orthod. 2021 Sep;19(3):389-405. doi: 10.1016/j.ortho.2021.07.002. Epub 2021 Aug 6. PMID: 34366263.

[23] Monje A, Chan HL, Galindo-Moreno P, Elnayef B, Suarez-Lopez del Amo F, Wang F, Wang HL. Alveolar Bone Architecture: A Systematic Review and Meta-Analysis. J Periodontol. 2015 Nov;86(11):1231-48. doi: 10.1902/jop.2015.150263. Epub 2015 Jul 16. PMID: 26177631.

[24] Filice N. Valutazione clinica e radiografica del rimodellamento volumetrico degli innesti ossei autologhi nelle ricostruzioni maxillo-facciali delle creste atrofiche a fini implantari ed analisi a cluster dei geni coinvolti nei processi di rimodellamento osseo. Tesi di dottorato. Milano: Università degli Studi di Milano-Bicocca; 2011.

[25] Safiotti A. Una nuova sistematica per la compattazione di osso di bassa qualità tramite frese rotanti. Tesi di laurea magistrale in Odontoiatria e Protesi Dentaria. Genova: Università degli Studi di Genova; 2020.

[26] Araújo MG, Wennström JL, Lindhe J. Modeling of the buccal and lingual bone walls of fresh extraction sites following implant installation. Clin Oral Implants Res. 2006 Dec;17(6):606-14. doi: 10.1111/j.1600-0501.2006.01315.x. PMID: 17092217.

[27] Kim S, Kim SG. Advancements in alveolar bone grafting and ridge preservation: a narrative review on materials, techniques, and clinical outcomes. Maxillofac Plast Reconstr Surg. 2024 Apr 16;46(1):14. doi: 10.1186/s40902-024-00425-w. PMID: 38625426; PMCID: PMC11021384.

[28] Ferraz MP. Bone Grafts in Dental Medicine: An Overview of Autografts, Allografts and Synthetic Materials. Materials (Basel). 2023 May 31;16(11):4117. doi: 10.3390/ma16114117. PMID: 37297251; PMCID: PMC10254799.

[29] Inchingolo F, Hazballa D, Inchingolo AD, Malcangi G, Marinelli G, Mancini A, Maggiore ME, Bordea IR, Scarano A, Farronato M, Tartaglia GM, Lorusso F, Inchingolo AM, Dipalma G. Innovative Concepts and Recent Breakthrough for Engineered Graft and Constructs for Bone Regeneration: A Literature Systematic Review. Materials (Basel). 2022 Jan 31;15(3):1120. doi: 10.3390/ma15031120. PMID: 35161065; PMCID: PMC8839672.

[30] Demir-Oğuz Ö., Boccaccini A.R., Loca D. "Injectable bone cements: What benefits the combination of calcium phosphates and bioactive glasses could bring?" Bioact Mater, 2022: 19:217-236. 10.1016/j.bioactmat.2022.04.007.

[31] Sivakumar P.M., Yetisgin A.A., Demir E., Sahin S.B., Cetinel S. "Polysaccharidebioceramic composites for bone tissue engineering: A review.", Int J Biol Macromol , 2023: 1;250:126237. 10.1016/j.ijbiomac.2023.126237.

[32] M. Aqib, A. Anwar, H. Ajaz, S. Akbar, A. Manzoor, M. Abid, Z. Waheed, Q. Kanwal, Metal-doped brushite cement for bone regeneration, JBE (2023) 1–16.

[33] G. Cama, F. Barberis, R. Botter, P. Cirillo, M. Capurro, R. Quarto, S. Scaglione, E. Finocchio, V. Mussi, U. Valbusa, Preparation and properties of macroporous brushite bone cements, Acta Biomater. 5 (2009) 2161–2168.

[34] Zhang J., Liu W., Schnitzler V., Tancret F., Bouler J.M. "Calcium phosphate cements for bone substitution: chemistry, handling and mechanical properties.", Acta Biomater, 2014: 10(3):1035-49. 10.1016/j.actbio.2013.11.001.

[35] F. Tamimi, Z. Sheikh, J. Barralet, Dicalcium phosphate cements: brushite and monetite, Acta Biomater. 8 (2012) 474–487, https://doi.org/10.1016/j. actbio.2011.08.005.

[36] D. Pham Minh, N. Lyczko, H. Sebei, A. Nzihou, P. Sharrock, Synthesis of calcium hydroxyapatite from calcium carbonate and different orthophosphate sources: a comparative study, Mater. Sci. Eng. B 177 (2012) 1080–1089, https://doi.org/ 10.1016/J.MSEB.2012.05.007.

[37] K. Issa, A. Alanazi, K.A. Aldhafeeri, O. Alamer, M. Alshaaer, Applications, brushite: synthesis, properties, and biomedical applications, Cryst. Appl. 80113 (2022) 1–15.

[38] A. Anwar, S.J.A.P.T. Akbar, Continuous microwave assisted flow synthesis and characterization of calcium deficient hydroxyapatite nanorods 29 (2018) 1493–1498.

[39] Hurle K., Oliveira J.M., Reis R.L., Pina S., Goetz-Neunhoeffer F. "Ion-doped Brushite Cements for Bone Regeneration.", Acta Biomater, 2021: 123:51-71. 10.1016/j.actbio.2021.01.004.

[40] Liu H., Li P., Tang Z., Liu H., Zhang R., Ge J., Yang H., Ni X., Lin X., Yang L. "Study on injectable silver-incorporated calcium phosphate composite with enhanced antibacterial and biomechanical properties for fighting bone cement-associated infections." Colloids Surf B Biointerfaces, 2023: 227:113382. 67 10.1016/j.colsurfb.2023.113382.

[41] K. Hasimoto, K. Yoshida, Y. Toda, T. Kanazawa, S. Udagawa, Antimicrobial properties and synthesis of tricalcium phosphate doped with alkali metal and silver ions, Phosphorus Res. Bull. 13 (2002) 123–126.

[42] M.M. Almoudi, A.S. Hussein, M.I.A. HassaSaudi Dent Jn, N.M. Zain, A systematic review on antibacterial activity of zinc against Streptococcus mutans, The Saudi dental journal 30 (2018) 283–291.

[43] X. Li, G. Li, K. Zhang, Z. Pei, S. Zhao, J. Li, Cu-loaded Brushite bone cements with good antibacterial activity and operability, J. Biomed. Mater. Res. B Appl. Biomater. 109 (2021) 877–889.

[44] P.A. Krokhicheva, M.A. Goldberg, A.S. Fomin, D.R. Khayrutdinova, O.S. Antonova, A.S. Baikin, A.A. Konovalov, A.V. Leonov, I.V. Mikheev, E.M. Merzlyak, Enhanced bone repair by silver-doped magnesium calcium phosphate bone cements, Ceram. Int. 49 (2023) 19249–19264.

[45] A. Anwar, D.J. Petrino Jr., N.V. Alstine, X. Yu, Biodegradable electrospun nanofibrous scaffolds for bone tissue engineering, Biomed Eng Technol. 2 (2022) 693–711. Springer.

[46] Z. Nawaz, H.N. Khalid, A. Sajid, F. Arshed, E. Ahmed, A. Sharif, I.H. Khan, A. Javaid, A. Sajid, A new bioactive steroid isolated from Nerium oleander L, Int. J. Biol. Biotechnol. 20 (2023).

[47] P.A. Krokhicheva, M.A. Goldberg, A.S. Fomin, D.R. Khayrutdinova, O.S. Antonova, A.S. Baikin, A.V. Leonov, E.M. Merzlyak, I.V. Mikheev, V.A. Kirsanova, Zn-Doped Calcium Magnesium Phosphate Bone Cements Based on Struvite and Their Antibacterial Properties, 2023.

[48] E. Boanini, M. Gazzano, A. Bigi, Ionic substitutions in calcium phosphates synthesized at low temperature, Acta Biomater. 6 (2010) 1882–1894, https://doi. org/10.1016/J.ACTBIO.2009.12.041.

[49] A. Anwar, S. Akbar, M. Kazmi, A. Sadiqa, S.R. Gilani, Novel synthesis and antimicrobial studies of nanoscale titania particles, Ceram. Int. 44 (2018) 21170–21175.

[50] Scheitz CJF, Peck LJ, Groban ES (2018) Biotechnology software in the digital age: are you winning? Journal of Industrial Microbiology & Biotechnology 45(7):529–534. https://doi.org/10.1007/s10295-018-2009-5

[51] Loh QL, Choong C (2013) Three-dimensional scaffolds for tissue engineering applications: role of porosity and pore size. Tissue Eng Part B Rev 19(6):485502. https://doi.org/10.1089/ten.TEB.2012.0437

[52] Awad HA, O'Keefe RJ, Lee CH, Mao JJ (2014) Chapter 83- bone tissue engineering: clinical challenges and emergent advances in orthopedic and craniofacial surgery. In: Lanza R, Langer R, Vacanti J (eds) Principles of Tissue Engineering (Fourth Edition). Academic Press, Boston, pp 1733-1743. doi: https://doi.org/10.1016/B978-0-12-398358-9.00083-5

[53] Bružauskaitė I, Bironaitė D, Bagdonas E, Bernotienė E (2016) Scaffolds and cells for tissue regeneration: different scaffold pore sizes-different cell effects. Cytotechnology 68(3):355–369. https://doi.org/10.1007/s10616-0159895-4

[54] Karageorgiou V, Kaplan D (2005) Porosity of 3D biomaterial scaffolds and osteogenesis. Biomaterials 26(27):5474–5491. https://doi.org/10.1016/j. biomaterials.2005.02.002

[55] Hölzl K, Lin S, Tytgat L, Van Vlierberghe S, Gu L, Ovsianikov A (2016) Bioink properties before, during and after 3D bioprinting. Biofabrication 8. https:// doi.org/10.1088/1758-5090/8/3/032002

[56] Padovani GCFVP, Sauro S, Tay FR, Durán G, Paula AJ, Durán N (2015) Advances in dental materials through nanotechnology: facts, perspectives and toxicological aspects. Trends Biotechnol 33:621–636

[57] Saad B, Suter UW (2001) Biodegradable polymeric materials. In: Buschow KHJ, Cahn RW, Flemings MC et al (eds) Encyclopedia of Materials: Science and Technology. Elsevier, Oxford, pp 551–555. https://doi.org/10.1016/B008-043152-6/00105-4

[58] Raghavendra SS, Jadhav GR, Gathani KM, Kotadia P (2017) Bioceramics in endodontics- a review. J Istanb Univ Fac Dent 51 (3 Suppl 1):S128-S137. doi:https://doi.org/10.17096/jiufd.63659

[59] Fernandes HR, Gaddam A, Rebelo A, Brazete D, Stan GE, Ferreira JMF (2018) Bioactive glasses and glass-ceramics for healthcare applications in bone regeneration and tissue engineering. Materials (Basel) 11(12):2530. https:// doi.org/10.3390/ma11122530

[60] Ishikawa K, Matsuya S, Miyamoto Y, Kawate K (2003) 9.05- bioceramics. In: Milne I, Ritchie RO, Karihaloo B (eds) Comprehensive Structural Integrity. Pergamon, Oxford, pp 169–214. https://doi.org/10.1016/B0-08-043749-4/ 09146-1

[61] Lin K, Sheikh R, Romanazzo S, Roohani I (2019) 3D printing of bioceramic scaffolds-barriers to the clinical translation: from promise to reality, and future perspectives. Materials (Basel) 12(17):2660. https://doi.org/10.3390/ ma12172660

[62] Rajzer I (2014) Fabrication of bioactive polycaprolactone/hydroxyapatite scaffolds with final bilayer nano-/micro-fibrous structures for tissue engineering application. Journal of Materials Science 49(16):5799–5807. https://doi.org/10.1007/s10853-014-8311-3

[63] Bose S, Vahabzadeh S, Bandyopadhyay A (2013) Bone tissue engineering using 3D printing. Materials Today 16(12):496–504. https://doi.org/10.1016/j. mattod.2013.11.017

[64] Hollister SJ, Murphy WL (2011) Scaffold translation: barriers between concept and clinic. Tissue Eng Part B Rev 17(6):459–474. https://doi.org/10. 1089/ten.TEB.2011.0251

[65] P. Fray, J.L. Trouillet, N. Rouquet, E. Azimus, A. Autefage, Osseointegration of macroporous calcium phosphate ceramics having a different chemical composition, Biomaterials 14 (1993) 423–429.

[66] Hirsch A., Azuri I., Addadi L., Weiner S., Yang K., Curtarolo S., Kronik L. "Infrared Absorption Spectrum of Brushite from First Principles.", Chemistry of Materials, 2014: 26 (9), 2934-2942. 10.1021/cm500650t.

[67] Mevellec J.Y., Quillard S., Deniard P., Mekmene O., Gaucheron F., et al. "Polarized infrared reflectance spectra of brushite (CaHPO4 center dot 2H(2)O) crystal investigation.", Spectrochimica Acta Part A: Molecular and Biomolecular Spectroscopy [1994-..], 2013: 111, pp.7. 10.1016/j.saa.2013.03.047.

[68] Ravaglioli A., Krajewski A. "Ceramics, cells, and tissues : surface-reactive biomaterials as scaffolds and coatings, interactions with cells and tissues.", Seminar and Meeting on Ceramics Cells and Tissues (12th 2009 Faenza Italy). 310-311.

[69] Muhammad Aqib, Muneerah Alomar, Aneela Anwar, Khalida Naseem, Arshad Javaid, Azeem Intisar, Shahzeb Khan, Humayun Ajaz, Iqra Haider Khan, Synthesis, characterization and antimicrobial

analysis of metal-doped (Zn2+ and Ag+) brushite powder for bone regeneration, Materials Chemistry and Physics, Volume 320, 2024, 129460, ISSN 0254-0584, https://doi.org/10.1016/j.matchemphys.2024.129460.

[70] C. Drouet, C. Rey, Nanostructured calcium phosphates for hard tissue engineering and nanomedicine, Nanostruct. Biomater. Regen. Med. (2020) 223–254, https:// doi.org/10.1016/B978-0-08-102594-9.00008-5.

[71] H. Mabroum, H. Noukrati, H. Ben Youcef, B. Lefeuvre, H. Oudadesse, A. Barroug, Physicochemical, setting, rheological, and mechanical properties of a novel bio- composite based on apatite cement, bioactive glass, and alginate hydrogel, Ceram. Int. 47 (2021) 23973–23983, https://doi.org/10.1016/J.CERAMINT.2021.05.106.

[72] M. Lakrat, M. Jabri, M.H. Fernandes, M.M. Alves, L.L. Elansari, C. Santos, E. M. Mejdoubi, Optimized consolidation process at a near-room temperature of nano-hydroxyapatite and sodium silicate glass composites for bone healing applications, Mater. Technol. (2022), https://doi.org/10.1080/ 10667857.2022.2053405.

[73] M. Tourbin, F. Brouillet, B. Galey, N. Rouquet, P. Gras, N. Abi Chebel, D. Grossin, C. Frances, Agglomeration of stoichiometric hydroxyapatite: Impact on particle size distribution and purity in the precipitation and maturation steps, Powder.

[74] M. Bohner, Calcium orthophosphates in medicine: from ceramics to calcium phosphate cements, Injury 31 (2000) S-D37eS-D47, https://doi.org/10.1016/ S0020-1383(00)80022-44.

[75] C. Oliveira, A. Ferreira, F. Rocha, Dicalcium phosphate dihydrate precipitation: characterization and crystal growth, Chem. Eng. Res. Des. 85 (2007) 1655e1661, https://doi.org/10.1016/S0263-8762(07)73209-4.

[76] S. Meininger, C. Blum, M. Schamel, J.E. Barralet, A. Ignatius, U. Gbureck, Phytic acid as alternative setting retarder enhanced biological performance of dicalcium phosphate cement in vitro, Sci. Rep. 7 (2017) 1e10, https://doi.org/ 10.1038/s41598-017-00731-6.

[77] K. Hurle, J. Neubauer, F. Goetz-Neunhoeffer, Hydration mechanism of partially amorphized b-tricalcium phosphate, Acta Biomater. 54 (2017) 429e440, https://doi.org/10.1016/j.actbio.2017.03.013.

[78] P.M.C. Torres, A. Marote, A.R. Cerqueira, A.J. Calado, J.C.C. Abrantes, S. Olhero, O.A.B. Da Cruz E Silva, S.I. Vieira, J.M.F. Ferreira, Injectable MnSr-doped brushite bone cements with improved biological performance, J. Mater. Chem. B. 5 (2017) 2775e2787, https://doi.org/10.1039/c6tb03119f.

[79] K. Spaeth, F. Goetz-Neunhoeffer, K. Hurle, The effect of Cu2+ doping in β-tricalcium phosphate on the hydration mechanism of a brushite cement, Materials Today Chemistry, Volume 27, 2023, 101288, ISSN 2468-5194, https://doi.org/10.1016/j.mtchem.2022.101288.

[80] J. Unosson, H. Engqvist, Development of a resorbable calcium phosphate cement with load bearing capacity, Bioceram. Dev. Appl. 4 (2014), 1000074, https://doi.org/10.4172/2090-5025.1000074.

[81] J. Engstrand, C. Persson, H. Engqvist, The effect of composition on mechanical properties of brushite cements, J. Mech. Behav. Biomed. Mater. 29 (2014) 81e90, https://doi.org/10.1016/j.jmbbm.2013.08.024.

[82] G. Cama, S. Nkhwa, B. Gharibi, A. Lagazzo, R. Cabella, C. Carbone, P. Dubruel, H. Haugen, L. Di Silvio, S. Deb, The role of new zinc incorporated monetite cements on osteogenic differentiation of human mesenchymal stem cells, Materials Science and Engineering: C, Volume 78, 2017, Pages 485-494, ISSN 0928-4931, https://doi.org/10.1016/j.msec.2017.04.086.

[83] A. Laskus-Zakrzewska, A. Zgadzaj, J. Kolmas, Synthesis and physicochemical characterization of Zn-doped brushite, Ceramics International 47 (2021) 7798–7804.

[84] I. Petrov, B. ˇ Soptrajanov, N. Fuson, J.R. Lawson, Infra-red investigation of dicalcium phosphates, Spectrochim. Acta Mol. Spectros 23 (1967) 2637–2646.

[85] T. Sopcak, L. Medvecky, M. Giretova, R. Stulajterova, J. Durisin, V. Girman, M. Faberova, Effect of phase composition of calcium silicate phosphate component on properties of brushite based composite cements, Mater. Char. 117 (2016) 17–29.

[86] F.E. Tabaght, K. Azzaoui, A. Elidrissi, O. Hamed, E. Mejdoubi, S. Jodeh, N. Akartasse, M. Lakrat, A. Lamhamdi, New nanostructure based on hydroxyapatite modified cellulose for bone substitute, synthesis, and characterization, Int. J. Polym. Mater. Polym. Biomater. 70 (2020) 437–448, https://doi.org/10.1080/00914037.2020.1725758.

[87] M. Lakrat, K. Azzaoui, S. Jodeh, N. Akartasse, E. Mejdoubi, A. Lamhamdi, M. Berrabah, O. Hamed, B. Razzouki, M. Algarra, The removal of methyl orange by nanohydroxyapatite from aqueous solution: Isotherm, kinetics and thermodynamics studies, Desalination Water Treat. 85 (2017), https://doi.org/ 10.5004/dwt.2017.21260.

[88] N. Ebadipour, S. Paul, B. Katryniok, F. Dumeignil, Calcium hydroxyapatite: a highly stable and selective solid catalyst for glycerol polymerization, Catalysts 11 (2021) 1247, https://doi.org/10.3390/CATAL11101247.

[89] R. Barua, C.S. Daly-Seiler, Y. Chenreghanianzabi, D. Markel, Y. Li, M. Zhou, W. Ren, Comparing the physicochemical properties of dicalcium phosphate dihydrate (DCPD) and polymeric DCPD (P-DCPD) cement particles, J. Biomed. Mater. Res. B Appl. Biomater. 109 (2021) 1644–1655.

[90] D.W. Gardner, J. Li, A. Morshedifard, S. Masoumi, M.J. Abdolhosseini Qomi, P. J. Monteiro, R. Maboudian, C. Carraro, Silicate bond characteristics in calcium–silicate–hydrates determined by high pressure Raman spectroscopy, J. Phys. Chem. 124 (2020) 18335–18345.

[91] I.S. Vintila, T. Badea, S. Draghici, H.A. Petrescu, A. Cucuruz, H. Iovu, A. Hadar, Mechanical characterization of DCPD and ENB healing systems in glass fibre composites, Mater. Plast. 57 (2020).

[92] T. Monia, β-TCP/DCPD-PHBV (40%/60%): biomaterial made from bioceramic and biopolymer for bone regeneration; investigation of intrinsic properties, J. Appl. Biomater. Funct. Mater. 20 (2022) 22808000221088950.

[93] Chen X, Fan H, Deng X, Wu L, Yi T, Gu L et al (2018) Scaffold structural microenvironmental cues to guide tissue regeneration in bone tissue applications. Nanomaterials (Basel) 8(11):960. https://doi.org/10.3390/ nano8110960.

[94] A. Ito, H. Kawamura, M. Otsuka, M. Ikeuchi, H. Ohgushi, K. Ishikawa, K. Onuma, N. Kanzaki, Y. Sogo, N. Ichinose, Zinc-releasing Calcium Phosphate for Stimulating Bone Formation, 22, 2002 21–25.

[95] J. Ovesen, J.S. Thomsen, G. Danscher, L. Mosekilde, The Positive Effects of Zinc on Skeletal Strength in Growing Rats, 29, 2001 565–570.

[96] Y. Qiao, Biomaterials stimulation of bone growth following zinc incorporation into biomaterials, Biomaterials 35 (2014) 6882–6897.

[97] H. Hu, W. Zhang, Y. Qiao, X. Jiang, X. Liu, C. Ding, Antibacterial activity and increased bone marrow stem cell functions of Zn-incorporated TiO2 coatingsontitanium,Acta Biomater. 8 (2012) 904–915.